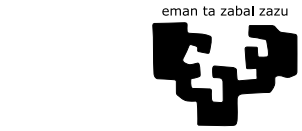

Design and Manufacturing of accelerator components for use on linacs

Doctoral thesis submitted for the degree of Doctor from the UPV/EHU by

Julio Lucas Torralba

Supervisor

Prof. Victor Etxebarria Ecenarro

Leioa, 2017

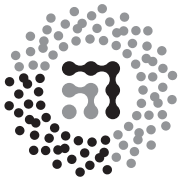

Departamento de Electricidad y Electrónica
Facultad de Ciencia y Tecnología

Elektrika eta Elektronika Saila
Zientzia eta Teknologia Fakultatea

(cc)2017 JULIO LUCAS TORRALBA (cc by 4.0)

Acknowledgments

This work would not have been possible without the collaboration of many people.

I would like first to think in my mother, Carmen, who gave me all the means to develop my career, and love to be able to concentrate in it.

To Arantxa, Enara and Tasio, who were so patient with me while I was working on it.

My colleagues at CERN during the years I spent there, were a continuous source of inspirational new ideas. There are too many persons there I am indebted, to mention each of them here. Some of them are my *frères* as well ...

The original idea to develop the PMQs for Linac4 came from M. Vretenar from CERN, the follow up of the contract by A. Lombardi was extremely helpful.

All my colleagues at ELYTT Energy, partners, collaborators and customers with whom I had so many fruitful discussions.

Contents

List of Figures

List of Tables

CHAPTER 1

Resumen

1.1 Estructura del presente trabajo

El presente trabajo está estructurado como una colección de diferentes contribuciones del autor al campo de la tecnología de los aceleradores de partículas así como a una aplicación derivada de este campo. Se cubren los dos dominios fundamentales de este ámbito, las cavidades de radiofrecuencia y los imanes; en el primero se describirá como el conocimiento de de las cavidades de radiofrecuencia ha sido utilizado para desarrollar un nuevo tipo de sensor de posición, que presenta una combinación de sensibilidad y ancho de banda que no puede ser igualada por ningún otro medio. En el campo de los imanes se describirán un par de aplicaciones, el desarrollo de un espectrómetro de gran apertura y a los cuadrupolos de imanes permanentes.

El uso de cuadrupolos de imanes permanentes (PMQ) para crear las estructuras de focalización dentro de un acelerador basado en tubos de deriva (DTL) presenta muchas ventajas. Pueden ser más puequeños que los los cuadrupolos electromagn'eticos y no requieren una fuente de alimentación externa, por ello la implementación del sistema total puede ser mucho más simple. Por otra parte, el menor tamaño del cuadrupolo permite reducir el diámetro de tubo de deriva y su tallo, reduciendo por tanto las pérdidas de radiofrecuencia. El principal inconveniente de los PMQ es la imposibilidad de ajustar su gradiente tras el montaje del tubo de deriva. ELYTT Energy ha diseñado y construido un conjunto de PMQs para ESS-B. Los imanes fueron construidos con una excelente concordancia entre los cálculos y las medidas. La tecnología desarrollada en este proyecto se empleó para construir los PMQ de los últimos tanques de linac de tubos de deriva de la cadena de inyección del complejo de aceleradores del CERN. Este diseño emplea una estructura muy económica usando 8 bloques de imanes permanentes del mismo tamaño.

También se publica en este trabajo una contribución a la teoría de la ecuación de Hill en el dominio complejo. La generalización que se presenta en esta obra permite emplear un método de variable compleja para resolver el problema de las oscilaciones betatrón de un haz.

1.2 Objetivos y vista general de la tesis

La tesis comienza con una breve descripción de la tecnología de los aceleradores de partículas cargadas y de sus dos técnicas fundamentales, las cavidades de radiofrecuencia (RF) y los imanes. En el primer capítulo se hace una descripción del efecto del campo electromagnético en los haces de partículas y de discute el principal problema al que se enfrenta el diseñador

de un acelerador.

El segundo capítulo trata de las cavidades de RF y como son utilizadas para acelerar el haz. Se presenta un desarrollo derivado del trabajo en este campo, en el que el cambio de sintonización de una cavidad debido al desplazamiento de sus paredes es utilizado para determinar el valor de este movimiento, así se obtiene un sensor muy eficaz.

Dado que el trabajo trata en gran parte del uso de cuadrupolos de imanes permanentes (PMQ) en aceleradores lineales (linacs) se relizará, en el tercer capítulo una breve introducción a la dinámica longitudinal en este tipo de máquinas. Solo se dará una pincelada de un campo muy amplio.

El siguiente capítulo tratará de la mecánica transversal del haz y especialmente de la parte lineal de esta mecánica, esto es de las perturbaciones en primer orden de la trayectoria ideal. Se presentará la teoría clásica de las matrices de transporte y de los parámetros de Twiss. El tratamiento de los parámetros de Twiss se realiza empleando formas cuadráticas para transportar el haz de un lugar a otro, un método, en mi opinión más simple que el tratamiento que suele emplearse en la mayoría de los libros de texto sobre la materia. Se realiza así mismo una contribución original a la teoría lineal, expandiendo algunos resultados que se conocían desde los años 50 del siglo pasado, sobre la representación compleja de del espacio de fase ocupado por un haz. El formalismo se resuelve totalmente y se identifica la naturaleza de la transformación compleja que sufre el espacio de fases. Esta identificación permite obtener algunos resultados que están ocultos en el formalismo convencional. Además, en este capítulo se explica como el autor desarrolló un espectrómetro de gran apertura mediante un dipolo de gran aceptancia.

La descripción matemática del campo magnético en la apertura de un imán es el objeto del siguiente capítulo. Se muestra el formalismo convencional y se desarrollan los procedimiento complejos para obtener los armónicos del campo magnético a partir de la distribución espacial de la magnetización. Así mismo se obtienen múltiples soluciones para el campo producido por algunas distribuciones simples. Se explica como se relaciona la simetría de los imanes con la simetría del campo y el resultado se resume en un par de matrices que relacionan los armónicos del campo con la simetría de los imanes. Finálmente se explica porqué la representación 2D es en este caso mucho más efectiva que en los imanes dominados por corrientes de trasporte.

El siguiente capítulo se dedica a los materiales empleados en los PMQ tanto para los imanes permanentes como para los retenedores. Se da una breve introducción a la ciencia del magnetismo en los materiales y como estas propiedades se relacionan con su uso en los PMQ. También se discute la importancia del vacío en la elección de los materiales.

Los últimos 3 capítulos se dedican al diseño y construcción de los PMQ para el linac4 del CERN (excepto los del primer tanque). El primero de estos capítulos muestra las especificaciones de los imanes y las opciones de diseño que hemos considerado. Se muestra el diseño final, que cumple las especificaciones y es especialmente simple de construir.

En el siguiente capítulo se muestra como se miden los bloques de imanes permanentes usando dos métodos diferentes. El primero mide el campo en una nube de puntos sobre el bloque de imán permanente. Las medidas en la nube son ajustadas mediante un método de mínimos cuadrados a los resultados de un programa de elementos finítos. El otro método emplea un conjunto de bobinas en las que se induce tensión mediante el desplazamiento de los bloques.

El último capítulo explica como ordenar los bloques de imanes permanentes para obtene cuadrupolos de alta calidad a partir de bloques no tan buenos. Se explica como medir los cuadrupolos mediante varios métodos y que medidas correctivas adoptar en caso de que el imán medido no esté en tolerancia.

CHAPTER 2

Abstract

2.1 Structure of the present work

The present work is structured as a collection of different contributions of the author to the field of accelerator technologies and an interesting spin-off of this field. The two main domains of the accelerator technologies are covered, RF cavities and magnets; in the former it will be described how the knowledge of RF cavities may be used to develop a new type of position sensor, which a combination of accuracy and band-width that probably cannot be matched by any other medium, in the latter a couple of applications related to a large aperture spectrograph and to the theory of permanent magnet quadrupoles will be described.

The use of permanent magnet quadrupoles (PMQ) to create the focusing lattice inside a drift tube linac (DTL) has many advantages. They can be smaller than electromagnetic quadrupoles and do not require an external power supply; moreover, the implementation of the complete system is simplified to a large extent. The smaller dimension of the quadrupole allows a reduction in the diameter of the drift tube and the stem, thus reducing RF losses. The main disadvantage of PMQs is the impossibility of tuning the integrated gradient of the quadrupole after building the drift tube. ELYTT Energy designed and built a set of PMQs for ESS-B. These magnets were then built and measured, with excellent match between the calculations and the measurements. The technology developed was then used to build all the focusing quadrupoles for the later tanks of the Drift Tube Linac of Linac4 [5] at the LHC injection chain. This design used a very economical design made of 8 identical blocks of permanent magnet material.

A contribution to the theory of the Hill equation in the complex domain is as well published for the first time in the present work. The generalization presented here, allows the complex method of solution of the Hill equation to be fully related to the theory of the betatron movement of particles in a beam.

2.2 Objectives and overview of the thesis

The thesis will start with a short description of the charged particle accelerator technology and its two main technologies, radiofrequency (RF) cavities and magnets. In this first chapter a brief description of the effect of the electromagnetic field in the beam particles will be presented and also the main challenges that the accelerator design faces will be discussed.

The second chapter deals with the RF cavities and how they are used to accelerate the beam. An original spin-off of this field is presented, in which the tuning of the cavity with

the displacement of its walls is used to determine the extent of this displacement, creating a highly effective sensor.

Because the use work treats to a large extent on the use of Permanent Magnet Quadrupoles (PMQ) in linear accelerators (linacs) a short introduction to the longitudinal dynamics of a beam in this type of accelerator is presented in the third chapter. Only a very limited version is presented in order to give a hint of the vast field of this subject.

The following chapter covers the transversal mechanics of the accelerator and specially the linear part of it, i.e. the first order perturbation with respect to the ideal trajectory. Here, the classical transport matrix and Twiss parameters theories are presented. The treatment of the Twiss parameters is based on matrix quadratic forms transforming phase space, which is in my opinion a simpler approach than the one found in most text books. An original contribution is made to the linear theory by expanding some results that were known since the 1950s in order to represent the phase space occupied by the beam by a single complex number, the formalism is completely solved and the nature of the transformation is identified. This identification allows to obtain some results that are very cumbersome to achieve in the classical formalism. In addition in this chapter, it is explained how the author developed a magnet to be used for spectrographic purposes, and that provides a huge acceptance of the beam.

The mathematical description of the magnetic field in a magnet aperture is shown in the following chapter. The conventional complex formalism is used. The analytical procedure to obtain the field harmonics development from the spatial distribution of magnetization is explained, and a significant amount of work is provided to obtain the field of simple permanent magnet geometries. It is explained how the symmetry in the magnets is related to the symmetry in the field, and this result is summarized in a pair of matrices that relates the field harmonics to the magnet symmetries. Finally, it is explained why the 2D representation of the permanent magnets provide a much better representation of the actually 3D structures than in the case of using transport currents.

One chapter is dedicated to the materials used in the PMQs for the permanent magnets and holders. A very short introduction to science of magnetic materials is provided and how its properties are related to the use in the PMQs. It is necessary, as well to discuss the effect of the material properties in vacuum.

The last 3 chapters are related to the design and manufacturing of the linac4 PMQ for CERN (except for tank 1). The first of these chapters provides the specification of the magnets and the available design options. A final design is shown, that satisfies the requirement and is simple to build.

In the following chapter, it is shown how the permanent magnets blocks are measured using two different methods, one measures the magnetic field at a cloud of points above the magnet using a Hall probe and the correlates, by a best fitting method, the measurements to the expected values using a Finite Element Method program. The other method uses a set of coils in which voltage is induced by displacing the magnet blocks.

The last chapters explains how the permanent magnet blocks may be sorted in order to provide high quality quadrupoles from lower quality permanent magnet blocks. It is explained how the quadrupoles may be measured, using several methods and which corrective measurements may be adopted in case the measurements show the magnets is not yet in tolerance.

CHAPTER 3

Introduction to Accelerator Technologies

3.1 Introduction to accelerator technology

Since its beginning in the late 19^{th} century, accelerator technology has evolved into a rich field, covering many applications requiring a wide range of beam energy, current, particle type and accuracy. Basically, a particle accelerator is a device that increases the energy of a beam of charged particles through the use of electromagnetic fields. The beams may be used in many fields of science and technology as nuclear research, high energy physics, medicine, material science, security, etc, ...

The size of the accelerators spans many orders of magnitude in all the significant parameters, with energies from a few keV for a cathodic ray tube to the 7 TeV per beam of the LHC. The current may vary as well from single particles to many kA as used in some fusion devices. The particles may vary from electrons to ions of the heaviest elements to complete molecules.

It is interesting that such a rich zoo of applications may be understood on the basis of a few key concepts, some of which will be described in the present work. The discipline of accelerator physics has two basic roots, the electromagnetic field theory, which will describe the forces acting on the beam, and the theoretical mechanics, which will describe how the beam will behave under such forces.

Typically, there are two different tasks in handling the beam, acceleration and confinement and transport. Acceleration can only be performed by the use of the electrical field, as the Lorentz force due to the magnetic field is always perpendicular to the velocity and therefore, no work may be performed by it on the particle. Confinement and transport may be performed either by the magnetic field or the electrical field, and both types of accelerators are widely used, with the electrical field being used towards the lower end of the energy.

3.2 Types of particle accelerators

The accelerators may be classified depending on several parameters. Here, we will use two criteria, the nature of the electrical field that will accelerate the particles and the geometry of the beam as it is carried along the accelerator. Lets start with the first one.

3.2.1 Electrostatic and RF accelerators

As we have seen, only the electrical field may accelerate the particles, on the other hand the electrical field may be DC or AC. In the first case, a constant voltage is created at a certain

point of the structure where the particles are born, the particles will be accelerated according to the direction of the electrical field to a target, typically at ground potential or even at a potential opposite to the source one. This approach is very simple conceptually, but it has the inconvenient of requiring large voltages that are difficult to handle due to the risk of unwanted electrical flash overs.

Most accelerators start with an electrostatic accelerator, the particle source, [1]. An example of an ion source may be seen in fig. 3.1. The most important feature is that the particles must be created already at the highest voltage of the accelerator, as their kinetic energy will be increased as the voltage decreases towards ground.

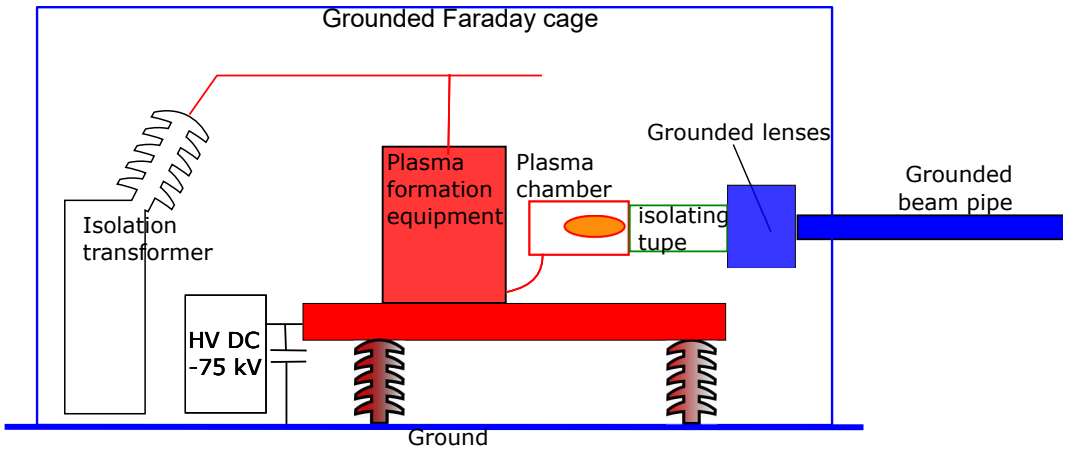

Figure 3.1 – Example of a negative ion electrostatic accelerator. All parts under voltage are in red, while all grounded parts are in blue

The high electrical voltage may be created in many different ways, with power electronics using typically voltage multipliers, the so called Cockcroft-Walton accelerators, or by mechanical charge transport, Van de Graf accelerators. In both cases, voltage confinement is the main challenge the designers of the accelerator must fight with.

Whatever the procedure used to obtain and confine the high voltage, electrostatic accelerators allow to obtain a continuous beam of well defined energy. They are used in many industrial applications, below 1 MeV with large currents and above several MeV for nuclear and material science applications in which the stability and very low energy or momentum spread of the beam is required.

RF accelerators use the alternating electrical field of an electromagnetic wave to provide energy to a particle in a sequence of steps. As in the electromagnetic wave the electrical field changes from positive to negative, the accelerating structure must be designed so as to screen the particle from the decelerating field while it is exposed to the accelerating field. This type of structure may be seen in fig. 3.2.

RF acceleration has the big advantage of being able to add unlimited energy to the particles while limiting the voltage inside the structure to a level that may be handled. The main inconvenient is that the accelerating structure is more complex and RF power is required in

[1] The most important exception being the electron RF sources, where the electrons are extracted from an appropriate cathode from the electrical field of a microwave cavity where it is inserted

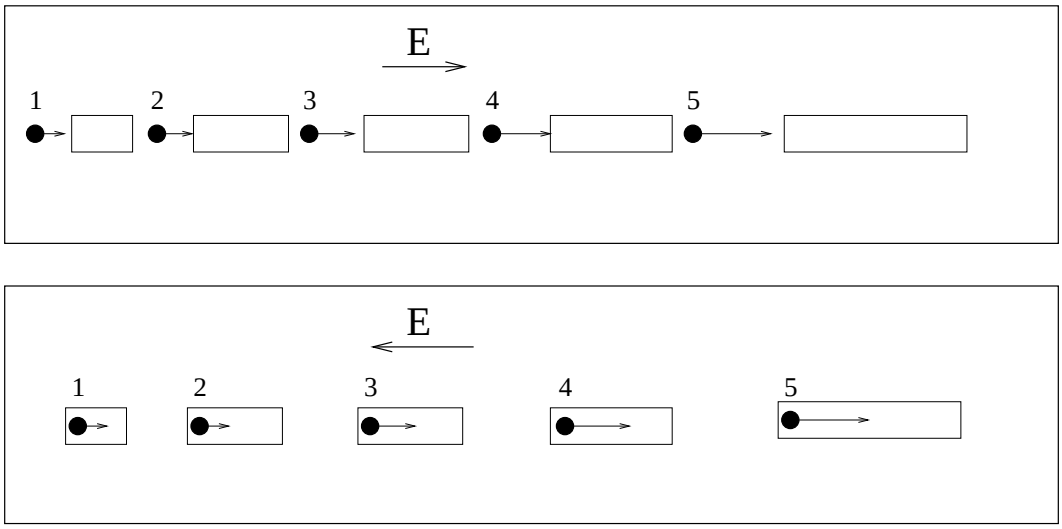

Figure 3.2 – Schematic representation of a standing wave RF accelerating structure. The small rectangles represent the part of the structure where no electrical field is present. On the left, the accelerating articles are in the region where the electrical field is present. During the electrical field phase reversal, right, the particles are screened from the decelerating field. The net effect is a rectification of the electrical field as seen by the particles.

the structure. Actually, RF accelerator technology took off after WWII, when the development of radar made RF hardware easily available.

In addition to the standing wave structures, for ultrarelativistic particles, usually electrons, it is possible to accelerate the beam by the use of a traveling wave similar to the one present in a waveguide. In this case, the relative phase between the electromagnetic wave and the particle may be kept in the accelerating region for a significant length.

3.2.2 Linear and circular accelerators

In the previous section, we have seen that for higher energies, RF accelerators must be used in order to avoid large voltages to ground. Nevertheless, in most cases, a single accelerating gap cannot provide enough voltage to increase the energy of the beam to the desired energy. Therefore, it is necessary for the particles to pass through several accelerating gaps. There are two solutions for this, in the first one, the beam follows a roughly straight trajectory and traverses several independent accelerating structures, whose phases are tuned to provide acceleration to the beam in each of them, this type of structure is called a linear accelerator or linac. In the second approach the beam is made to follow a curved trajectory which passes several times through the same accelerating structure, this structure is called a circular accelerator, of which there are many variants. A comparison between a linear accelerator and a circular one is schematically shown in fig. 3.3.

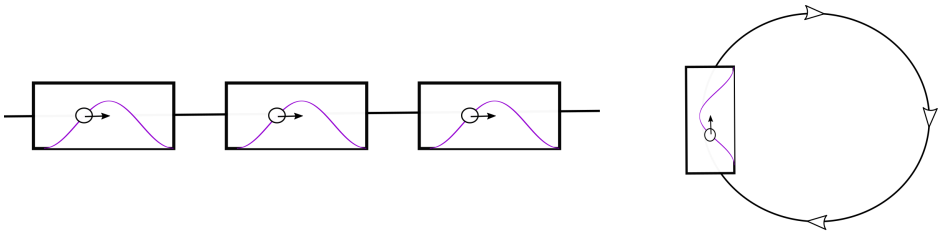

Figure 3.3 – Schematic comparison between a linac, left, and a circular accelerator, right. The RF cavities are represented as a cosinus wave with the particle mounted on the relative phase

3.2.3 Types of circular accelerators

As we will see in Chapter 6, the trajectory of a particle of momentum p and charge e in a magnetic field B has a curvature radius, ρ, defined by,

$$B\,\rho = \frac{p}{e} \tag{3.1}$$

, where the ratio between the momentum and the charge is known as the magnetic rigidity. The main consequence of eq. 3.1 is that as the particle gains energy and therefore momentum, either the radius of curvature, the applied field or both must change. If the field does not change the particle must describe a trajectory of increasing radius of curvature, spiraling from the inside of the accelerator towards the outside. The archetypal accelerator using this principle is the cyclotron, [2]. In the cyclotron, the beam is accelerated continuously from the center towards the periphery by a constant magnetic field and RF power. The operation of the conventional cyclotron is made possible by the fact that in non relativistic conditions, the frequency of revolution of a particle is independent of the energy, and therefore, the particles may be resonantly accelerated in a continuous way. At higher energies, relativistic effects cause that the revolution frequency decreases below what it is necessary to maintain the accelerating resonance.

To quantify this statement, we can calculate the orbiting frequency of a particle in a constant magnetic field, the so called cyclotron frequency, expressing the momentum as a function of velocity and the relativistic γ and taking into account that the length of the orbit is $2\pi\rho$, the cyclotron frequency will be,

$$\omega_c = \frac{eB}{\gamma m} \tag{3.2}$$

In this expression, we can see that at low energies, where $\gamma \approx 1$, the cyclotron frequency is constant and an accelerating resonance may be obtained easily. At higher energies, it is possible to keep the resonance by modulating the average magnetic field at a certain orbit radius so that the increase on the average field cancels the increase of γ, this approach is called isochronous cyclotron. Nevertheless, the increase of the average magnetic field cannot be obtained just by a higher azimuthally constant field, as the vertical stability of the particle movement requires actually a radially decreasing magnetic field. For isochronous cyclotrons,

[2] A different accelerator with this type of structure is the microtron [51]

it is essential to have azimuthal variation of the field to provide the vertical focusing through the principle of strong focusing allowing for a radially increasing average magnetic field.

In the second approach to circular accelerators, the orbit is kept constant and the magnetic field is increased to cope with the increasing magnetic rigidity. This type of accelerator is called a synchrotron. This principle allows to reach higher energies than any other, as the small volume on which the magnetic field must be created make possible to increase the diameter of the orbit to much larger values than in a cyclotron, in which the magnetic field must extent over the whole surface where the beam is. Actually, for a cyclotron the cost of generating the magnetic field scales as the third power of the energy, as the magnetic flux acting on the beam must return through the third dimension. On the contrary, for a synchrotron, the cost of creating the magnetic field only increases linearly with the energy.

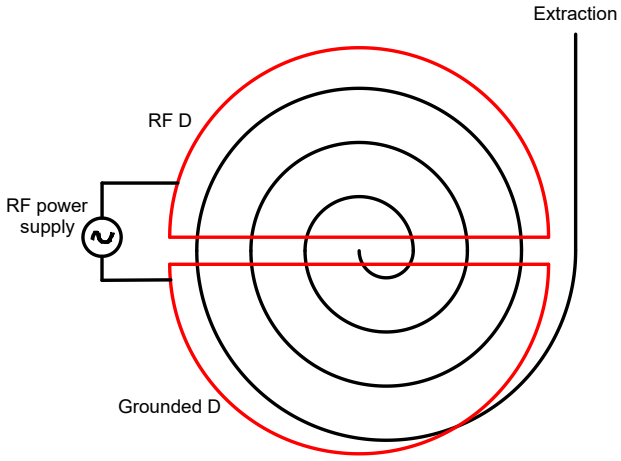

Figure 3.4 – Schematic representation of a ciclotron

A hybrid approach to the compensation of the increase of the magnetic rigidity is the synchrocyclotron, in which the effect of the relativistic decrease of the cyclotron frequency is compensated by a temporal modulation of the RF frequency.

An interesting property of the cyclotron, shared with the linac, is that the acceleration proceeds in a continuous way, this allows to accelerate a large average current of the beam. On the other hand, the synchrotron may handle a large instantaneous current but a low average current, as the acceleration must be performed over a extended period of time, required to increase the magnetic field. An analogy exists with the comparison between an elevator and mechanic stairs, as the former must load people on one floor and unload them on another the amount of people transferred is lower than in the latter. In the same way, mechanical stairs are not optimal for transferring people through many floors, as they are more expensive in this case. Therefore linacs and cyclotrons are used for applications where moderate energy but high beam current is required like the International Fusion Material Irradiation Facility, IFMIF [23], the European Spallation Source, ESS [22], the accelerator production of tritium, APT [15], the aceelerator driven system MYRRHA [16] or the Spallation Neutron Source [40].

On the other hand the high energy (per particle) frontier is the domain of the synchrotrons with the LHC being the highest performer at present day, [14], [28].

CHAPTER 4

RF resonant cavities: application for high accuracy sensors

In this chapter we want to describe a very interesting application that was developed by the author as a spin-off of the work in the accelerator field. The main idea is to use the strong dependency of a high-Q resonant cavity with respect to its geometry in order to use it as a displacement sensor. As anybody that must tune a RF cavity to the desired frequency may confirm the smallest geometrical imperfection will displace the resonant frequency beyond the acceptable limits. The question is then, why not to use this characteristic to our advantage? A quick review of the bibliography, both academic and industrial showed that this field was almost unexplored and it was quickly decided to build a prototype that performed successfully. The idea was successfully carried out from the technical point of view and a patent was achieved on the novel idea of using resonant RF cavities for very accurate displacement sensing [38].

In this chapter, I will describe first what a resonant cavity is and how they are used in the field of particle accelerators, our starting point. We will then proceed to explain how a resonant cavity may be used as a displacement detector and which properties will be optimal for this application. We will finally describe the prototype and the result of the experimental set up.

4.1 What is a resonant cavity?

In its most basic definition, a resonant cavity is a closed volume surrounded by highly conducting walls. In this volume, an electromagnetic standing wave is established by some external circuit which couples to the cavity through a small aperture. Inside the volume of the cavity there is a dielectric medium or vacuum. At each point inside the cavity, the Maxwell equations will be fulfilled and it is possible to have a self sustaining electromagnetic cycle in which the displacement currents create a magnetic field and the variation of the magnetic field induces electrical field. By using the same derivation than for a free space electromagnetic wave, it is possible to obtain that the fields inside the cavity will satisfy the wave equation, both for the electric and the magnetic field.

$$\nabla^2 \vec{B} = \frac{1}{c^2} \frac{\partial^2 \vec{B}}{\partial t^2} \tag{4.1}$$

$$\nabla^2 \vec{E} = \frac{1}{c^2} \frac{\partial^2 \vec{E}}{\partial t^2} \tag{4.2}$$

If we are only interested in the steady state of the cavity, we can replace the vectors by phasors and the time derivative by multiplication by $j\omega$. In this case, the wave equations are replaced by Helmholtz equations, i.e.

$$\nabla^2 \vec{B} + k^2 \vec{B} = 0 \tag{4.3}$$

$$\nabla^2 \vec{E} + k^2 \vec{E} = 0 \tag{4.4}$$

, where k is the free space wave number ω/c. These equations have to be compatible with the boundary conditions on the walls of the cavity.

The electric and magnetic fields in the volume of the cavity are sustained by surface charge densities, σ_q and surface current densities j_s. The surface charge density and current density are related to the fields near the surface of the cavity by the boundary equations,

$$\vec{E} = \frac{\sigma_q}{\epsilon} \vec{n} \tag{4.5}$$

$$\vec{B} = \mu_0 \vec{j_s} \times \vec{n} \tag{4.6}$$

, where $\vec{n}$ is the surface normal pointing inwards to the cavity at each surface point.

It may be proved [53], that the set of Helmholtz equations 4.3, 4.4, coupled with the boundary conditions of eqs. 4.5 and 4.6 form and eigenvalue and eigenvector problem in which the solutions only exist for a set of discrete values of the wave number k.

It is possible to analyze the operation of the cavity in two complementary ways, in one of them, the electromagnetic fields play the main role and the surface currents and charges are derived from them; in the second way, the surface currents and charges are the principal elements and the electromagnetic fields are derived from them. This second way bears some reminiscence to the low frequency approach of lumped components (capacitors and inductors) and it is very attractive for separated function cavities, in which the electric and magnetic fields are mostly separated inside the volume of the cavity.

An absolutely lovely description of a RF cavity as a series of superposition of electric and magnetic fields being alternatively generated one from the other and creating the correct solution to the Helmholtz equations for a pillbox geometry may be found in the Feynman lectures [29].

A typical case of resonant cavity is a transmission line in which both extremities are closed by a conducting wall. In this case, the cavity may be seen as two traveling waves interfering at the extremities to comply with the material boundary conditions. Only at a set of discrete frequencies will the forward and backward waves provide the appropriate cancellation of the desired components of the electrical and magnetic field.

All cavities will have some type of losses, either due to non perfect walls or to lossy dielectric materials in the volume of the cavity. In this circumstance, a self supporting oscillation at a certain resonant frequency will have a decreasing amplitude, as the electromagnetic energy is dissipated. The losses are usually characterized by the resonator quality factor Q , which is proportional to the ratio between the electromagnetic energy of the cavity and the loss of energy over one period,

$$Q = 2\pi \frac{U}{\Delta U} = \frac{\omega U}{< P >} \tag{4.7}$$

, where $< P >$ is the average loss of energy over a cycle. The decay of energy in the resonator will be determined by the differential equation,

$$\frac{dU}{dt} + \frac{\omega}{Q} U = 0 \tag{4.8}$$

,and therefore the decay will be an exponential of time constant Q/ω.

4.2 Application of resonant cavities for sensors

Anyone who has been working with high Q radiofrequency cavities knows how difficult is to stabilize the resonance frequency to the design one. In a particle accelerator, every cavity must resonate at exactly the same frequency and with the appropriate phase in order to accelerate the beam synchronously. This is achieved by means of a vector control of the power coupling and with a mechanical tuner to modify the geometry of the cavity in order to adjust the resonance to the desired value. It is very typical that a small deformation of the cavity, due for instance to a temperature change, fully detunes the cavity and requires a displacement of the tuner in the millimeter range.

The idea of using RF to determine the displacement, as shown in [26] and [8], of a system came originally from the collaboration between the Basque Country University (BCU) and ELYTT Energy to develop a very simple high-Q resonant structure to be used as a test bench for the 324 MHz low level that the BCU was developing for the Rutherford Appleton Laboratory. This structure had to be small in order to be easily handled on a table top set-up. The easiest way to lower the frequency of a pillbox cavity is to electrically load it, obtaining a re-entrant structure. This type of structure is very sensitive to a variation of the gap, i.e. the region where the electrical field is confined. A drawing of the cavity that was finally built is shown in fig. 4.1. In this cavity a radial tuner is used to adjust the resonance frequency to the desired value. It was very appealing how sensitive the resonance frequency was to the smallest deformation of the lid. As the group of the BCU that was developing the low level RF for the Rutherford Appleton Laboratory was involved at the same time in micro-positioning systems, it came naturally a question on the possibility of using the tuning of RF cavities to measure micro displacements in the range of tens of nanometers.

Some advantages of the this type of sensor are:

1. It may have a very high resolution when a high Q cavity is used as the resonator.

2. Very large stroke compared with other sensors of equivalent resolution.

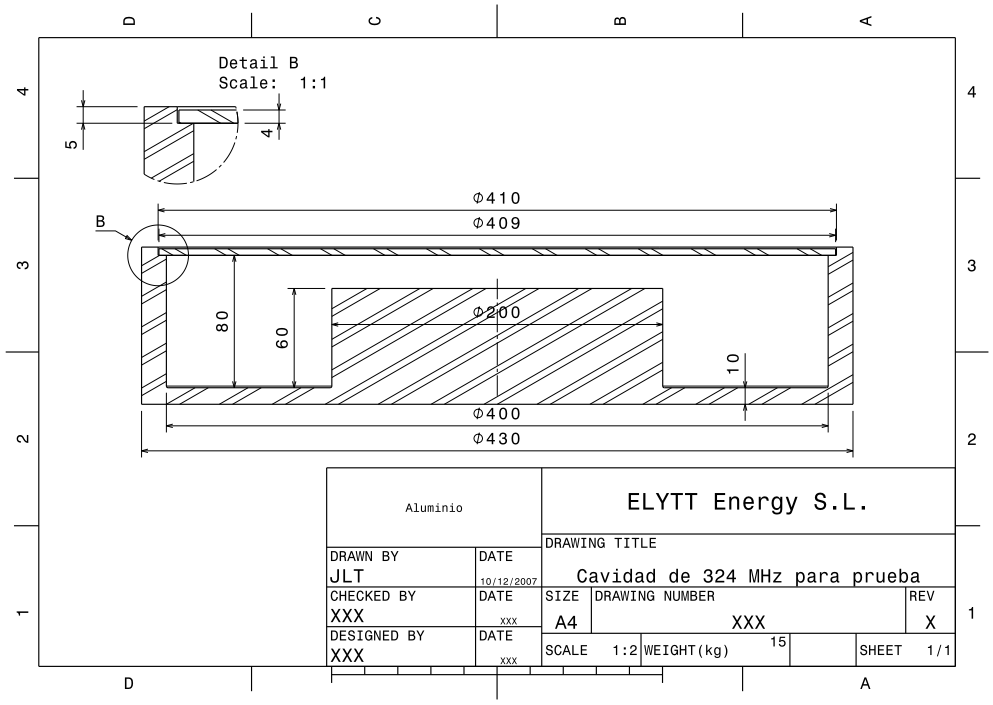

Figure 4.1 – Dummy Cavity used for the developing the control of the RAL low level RF system

3. Low sensibility to thermal variations if used in differential mode (see below).

4. Low sensibility to electromagnetic noise as the cavity is a perfect screen to EMI.

5. It may be low cost as the RF electronics involved may be mass produced and the machining tolerances are moderate. A possible interface electronics is explained in [7] and [6]

6. The signal between the electronics and the sensor may be transmitted over very large distance with a coaxial line. As the signal is frequency coded, it is interference immune.

7. The sensor is extremely rough. There are no complicated mechanical movements.

8. Because of the large operating frequency of the sensor, it is possible to detect signals of very large band-width. It would be possible to detect signal with variations in the MHz range by using a cavity tuned to resonate in the GHz range

This section describes the developments performed along the path described in the previous paragraph. First the theory of the small gap re-entrant cavity is explained, and we give the reasons to choose this geometry among others for the linear displacement transducer. Then we describe the differential sensor, in which the displacement modifies at the same time two cavities but in different direction, increasing the frequency of one cavity and decreasing the other one. We then describe the mechanical structure of the prototype and the results of the measurements. Finally, we give some ideas of the direction of future developments.

4.2.1 Detailed design

General theory of the separated field cavity

In order to obtain a large variation of the cavity parameters, it is necessary that the electric part of the cavity is modified in a substantial way. We will ask to the resonant cavity the following properties:

1. A large sensitivity to the variation of the resonant frequency to the displacement
2. A high Q so that the resonance frequency is well defined
3. The resonant frequency should be in the region of hundred of MHz to a few GHz for easy measurement
4. Low sensitivity to temperature variations
5. Easy integration of the displacement coupler to the cavity geometry

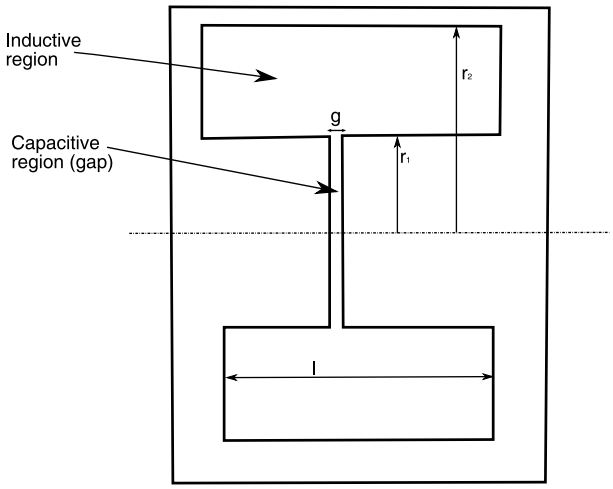

Figure 4.2 – Model of a separated field cavity

In the separated field cavity the electrical field is concentrated around the small gap and is axial. The magnetic field is azimuthal and almost the whole flux is contained in the region $r_1 < r < r_2$. As the region in the gap sees a constant flux variation (not varying with r_1), and the gap is uniform, the electrical field is constant in the gap region. On the other hand, the variation of the magnetic field, will be defined by the displacement current as:

$$\frac{\partial B_\phi}{\partial r} + \frac{B_\phi}{r} = j\omega\mu_0\epsilon_0 E_z \tag{4.9}$$

This equation may be solved to find that the magnetic field increases linearly in the gap region and decreases hyperbolically in the outer region. The qualitative shape of the field is shown in fig. 4.3.

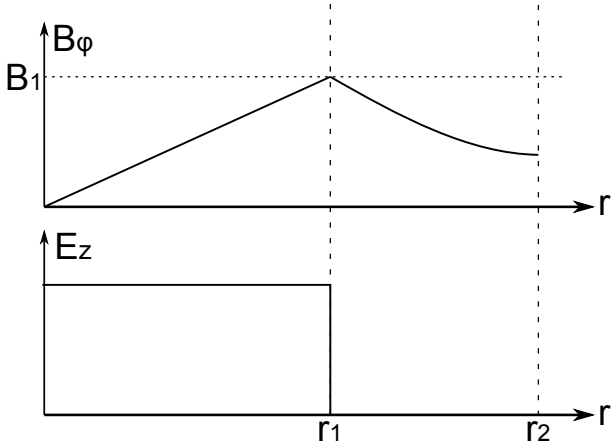

Figure 4.3 – Qualitative shape of the electrical and the magnetic field in the separated field cavity

If we use the magnetic field at r_1 to normalize the field and call it B_1, we will have the following expression for the magnetic field:

$$B = \begin{cases} {}^{B_1 r}/_{r_1} & \text{if } r < r_1, \\ {}^{B_1 r_1}/_{r} & \text{if } r > r_1 \end{cases} \tag{4.10}$$

The total flux in the cavity will be:

$$\Phi = \int_{r_1}^{r_2} B l dr = B_1 l r_1 \ln\left({}^{r_2}/_{r_1}\right) \tag{4.11}$$

The stored energy will be:

$$U = \int_{r_1}^{r_2} \frac{B^2}{2\mu_0} l 2\pi r dr = \frac{B_1^2 r_1^2 l \pi}{\mu_0} \ln\left({}^{r_2}/_{r_1}\right) \tag{4.12}$$

Because the electric field in the gap is constant, we can say that the total displacement current in the gap is:

$$I_d = j\omega\epsilon_0 E \pi r_1^2 \tag{4.13}$$

We can use Ampere's law to determine the electric field from B_1:

$$\frac{B_1}{\mu_0} 2\pi r_1 = \epsilon_0 j\omega E \pi r_1^2 \tag{4.14}$$

Giving,

$$E = \frac{V}{g} = \frac{-jB_1}{\mu_0\epsilon_0\omega r_1} = \frac{-jB_1 c^2}{\omega r_1} \tag{4.15}$$

Eq. 4.15 provides the voltage in the gap required to produce the right amount of displacement current to sustain the total magnetic flux in the outer region. The variation of this flux will create the same voltage, so that:

$$V = -\frac{d\Phi}{dt} = -j\omega\Phi = -j\omega r_1 l \ln\left({}^{r_2}/_{r_1}\right) \tag{4.16}$$

Equating both expressions of the gap voltage, we can obtain the resonance frequency:

$$f_0 = \frac{c}{r_1}\sqrt{\frac{2g}{l\ln\left({}^{r_2}/_{r_1}\right)}} \tag{4.17}$$

To obtain the Q factor of the cavity, we need the losses as a function of B_1. In order to calculate the losses we perform the following surface integral in all the surfaces of the cavity:

$$P = \frac{R_s}{2\mu_0^2}\int_A |B| dS = \frac{\pi R_s B_1^2 r_1}{\mu_0^2}\left(l + \frac{l r_1}{r_2} + \frac{r_1}{2} + 2r_1 \ln\left({}^{r_2}/_{r_1}\right)\right) \tag{4.18}$$

R_s is the surface resistance of the material at a frequency of ω, and its value is:

$$R_s = \sqrt{\frac{\omega\mu_0\rho}{2}} \tag{4.19}$$

where ρ is the resistivity of the material.
The value of the quality factor will be:

$$Q = \omega\frac{U}{P} = \frac{\omega\mu_0 \ln\left({}^{r_2}/_{r_1}\right) l}{R_s\left(\frac{l}{r_1} + \frac{l}{r_2} + \frac{1}{2} + 2\ln\left({}^{r_2}/_{r_1}\right)\right)} \tag{4.20}$$

With the calculated expressions in hand, it is possible to make a design to optimize the sensitivity of the sensor. In fig. 4.4, we have varied the radius of the gap region r_1 and we have calculated the resonance frequency and the quality factor. As we may see, the quality factor steadily decreases with increasing r_1; while the resonance frequency has a minimum when $r_2 = 2r_1$.

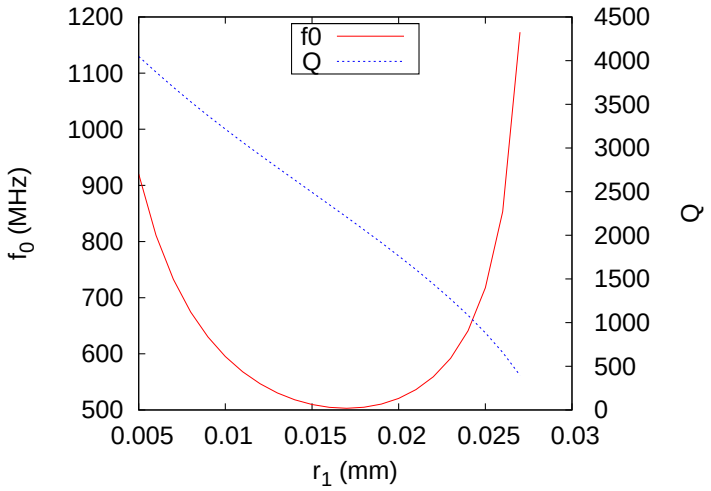

Figure 4.4 – Parametric properties of the cavity as r_1 varies. The other values are $r_2 = 25$ mm, l=25 mm, and g=0.2 mm.

For the present design, we have adopted a value of 15 mm for r_1, a smaller value would

have provided a larger Q, which may be interesting to improve the sensitivity of the device. It would be possible, as well, to improve the quality factor by having a different shape of the inductive part of the cavity. This is due to the fact that the losses are due to the effect of the magnetic field on the conductive wall, and therefore is related to the surface of the inductive part. On the other hand, maintaining the same resonant frequency, depends only on the volume of the inductive part. From this two facts, the optimal shape of the inductive part is a torus of circular section. This is the typical shape, for instance, of the re-entrant cavities in particle accelerators.

Design with Superfish

To validate the analytic design, the cavity has been simulated with a FEM program. The Superfish program fro LANL has been chosen for this purpose [54]. The input program, for Superfish is written using a Perl macro that writes the Superfish file. In such a way, parametric capabilities are added to the Superfish input language and it is possible to perform an optimization of the cavity geometry. The output of the Superfish simulation is shown in fig. 4.5.

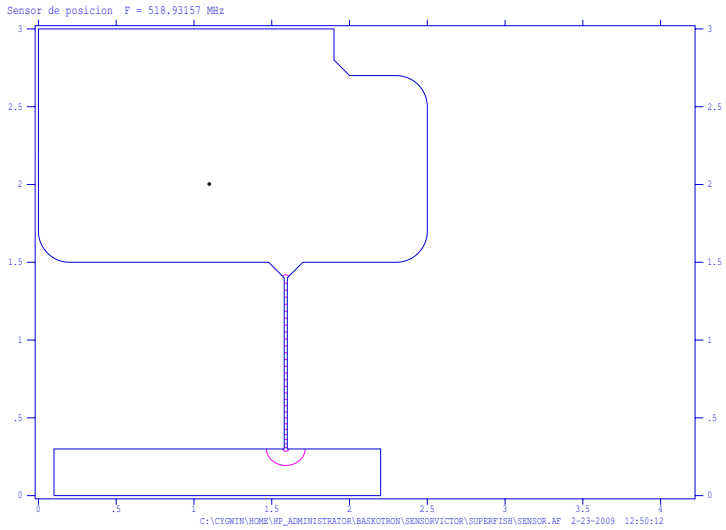

Figure 4.5 – Superfish plot of the cavity

The FEM model is in excellent agreement with the analytical results of the previous section. The model may be run with different values of the capacitive gap in order to check the sensitivity of the resonant frequency to the axial position of the shaft. For a central frequency of 518.93 MHz, the resonance shifts up to 530.82 MHz for a 10 μm increase of the gap (nominal 200 μm) and decreases to 506.69 MHz for a 10 μm reduction of the gap. This values reproduce very well the expected value of 1.3 MHz/μm.

Operation in differential mode

It is possible to build the sensor in differential mode. In such a way, the displacement to be measured causes the frequency of two cavities to be changed in opposite direction, in one of

them the frequency increases, while in the other the frequency decreases. The displacement is then induced from the frequency difference between both cavities. Two advantages derive from this approach, the first is that the sensor is less sensitive to temperature variations, as the thermal expansion will change the frequency of both cavities in the same direction. The second advantage is that the sensitivity increases by a factor of 2.

In fig. 4.6, we may see an example of a differential mode sensor.

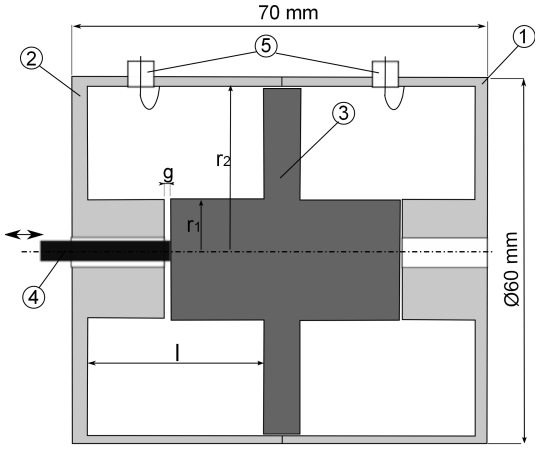

Figure 4.6 – Schematic view of the differential mode operation

Parameter determination

In order to model the cavity, in this section we will determine the equivalent circuit parameters of each individual cavity. The circuital model will be very useful to calculate the required coupling of the circuit to the feeding line. From the transmission line point of view, the cavity must be coupled so that it looks like a matched load to the characteristic impedance of the coaxial line. This matching is made easier if the cavity is represented by a circuital equivalent.

We will require the four following magnitudes of the cavity near the resonant frequency to be reproduced by the equivalent circuit: The values provided by Superfish are:

1. The resonant frequency
2. The on-axis voltage (integral of the electric field)
3. The stored magnetic and electric energy
4. The losses

These magnitudes are provided by the electromagnetic field solver program. The following equations allow to obtain the equivalent circuit parameters:

$$U = \frac{1}{2}CV^2 \tag{4.21}$$

$$f_0 = \frac{1}{2\pi\sqrt{LC}} \tag{4.22}$$

$$R = \frac{Q_0}{2\pi f_0 C} \tag{4.23}$$

Which may be used to obtain the circuital parameters

$$C = \frac{2U}{V^2} = 28.03pF \tag{4.24}$$

$$L = \frac{1}{C\left(2\pi f_0\right)^2} = 3.35nH \tag{4.25}$$

$$R = \frac{Q_0}{2\pi f_0 C} = 37k\Omega \tag{4.26}$$

We can now use these parameters to calculate the antenna area in order to match the cavity to the 50 Ω feeding transmission line. The transformer ratio of the coupling between the antenna and the cavity will be the ratio of the total cavity flux to the flux link by the antenna area A_{loop}. In a cavity which has virtually no electric field in the inductive region, the magnetic induction will satisfy:

$$B(r) = B_2\frac{r_2}{r} \tag{4.27}$$

Where B_2 is the field at the outer radius r_2. Let r_1 be the radius of the cavity at the end of the electric part and l the length of the magnetic part. The total flux will be:

$$\Phi = \iint_s B_2\frac{r_2}{r}\,dzdr = B_2 r_2 l \log\frac{r_2}{r_1} \tag{4.28}$$

If the antenna is small and it is located near the outer radius, where the field is B_2, the link flux will be $B_2 A_{loop}$. Therefore the transformer ratio between the antenna and the cavity will be:

$$n = \frac{r_2 l}{A_{loop}} \log\frac{r_2}{r_1} \tag{4.29}$$

For our cavity, we would like:

$$Z_0 = R' = \frac{R}{n^2} \tag{4.30}$$

Where the prime on the resistance, means that it has been transferred to the feeding line. From this equation, we can calculate that a transformer ratio of 27 is desired, and from eq. 4.29, an antenna loop area of 19.1 mm^2 is required.

4.2.2 Surface roughness

The rule of thumb is that the surface roughness (specified as R_a) must be a quarter of the skin depth at the given frequency and material. The skin depth is given as:

$$\delta_s = \sqrt{\frac{\rho}{\omega\mu}} \tag{4.31}$$

In our case (500 MHz and copper) this implies a value of 0.73 μ m, which we will round to the more standard $R_a 0.8$ in the inside of the cavity, while for the outside the specified value is $R_a 3.2$.

4.2.3 Relationship between the quality factor of the cavity and the sensitivity of the sensor

It is possible to take a logarithmic derivative of the resonance frequency with respect to the gap to obtain:

$$\frac{\Delta f}{f_0} = \begin{cases} \frac{1}{2}\frac{\Delta g}{g}, \text{for the standard re-entrant cavity,} \\ \frac{\Delta g}{g}, \text{for the differential re-entrant cavity,} \end{cases} \tag{4.32}$$

In order to be detectable, this frequency variation must be larger than f_0/Q, and therefore, we must state that the resolution of the sensor will be in the order of:

$$\Delta g \geq \begin{cases} \frac{2g}{Q}, \text{for the standard re-entrant cavity,} \\ \frac{g}{Q}, \text{for the differential re-entrant cavity,} \end{cases} \tag{4.33}$$

This result is rather pessimistic, and should only indicate a minimum resolution of the sensor, as with appropriate filtering, it should be possible to determine the resonance frequency well inside the bandwidth of the resonator. In any case, it is a clear indicator that a high Q is desirable in order to improve the resolution of the sensor.

Another interesting point is the possibility of using superconducting cavities with quality factors in the order of 10^9, [43]. In this type of sensor, the accuracy will be limited by the measurement equipment and not by the resonator itself. A collateral advantage of the use of superconducting cavities would be the stable operation of both, the cavities and the samples at cryogenic temperature.

4.2.4 Technical Implementation and experimental results

Technical Implementation

This section describes the technical implementation of the sensor calculated in the previous sections. Fig. 4.7 shows a technical drawing of the cross section of the magnet, while fig. 4.8 shows an isometric view of the sensor.

The main body and the movable central part are made of high conductivity copper. For the connection rods, we built an initial prototype using a machinable ceramics, but it showed to be brittle and difficult to join to the movable part. We then built the connecting rods in a technical plastic, which showed far better mechanical behavior. Nevertheless, the plastic has

worse thermal behavior (a much larger thermal expansion coefficient) and is less stiff, what probably exacerbates the stick-slip effect.

The central part and the movable part has an ISO 286 H7/h6 fitting, which provides an evanescent wave in the small coaxial channel between both parts effectively decoupling the two differential cavities.

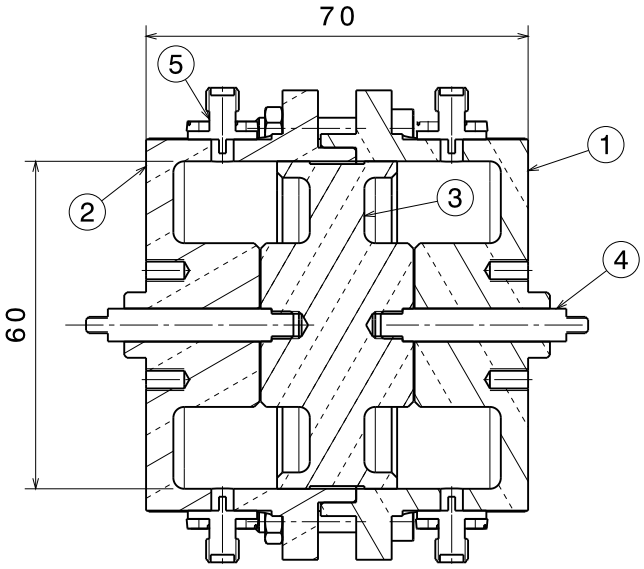

Figure 4.7 – Section of the sensor. 1 and 2 form the main body of the sensor, 3 is the movable central part, 4 is the plastic connection rod which is used to transmit the displacement, 5 is the SMA coaxial coupler.

The coupling of RF to the cavity is made by two loops per cavity built at the end of an SMA connector. These connectors may be seen in fig. 4.8.

Experimental Set Up

The prototype has been built and measured in the experimental set-up of fig. 4.9. The sensor is attached to two rings that are fixed to an optical bench. The displacement of the sensor is controlled with a micrometer. In future sensor, it is planned that the actuator will be a piezoelectric, whose displacement may be controlled in the range of the tens of nanometers. Unfortunately, the stick-slip effect and the high rigidity of the prototype have made impossible to perform these measurements with the present design.

Averaging over large displacements (as they are the caused by the micrometer), the sensor behaves as expected, see fig. 4.10.

4.2.5 Membrane design

As we have mentioned before, the stick-slip movement made impossible the measurement of displacements in the order of the tens of nanometers, which is the theoretical limit of the sensor. In order to solve this problem, we are developing a second prototype based in a membrane which is deformed by the force transmitted through the movable part. Although

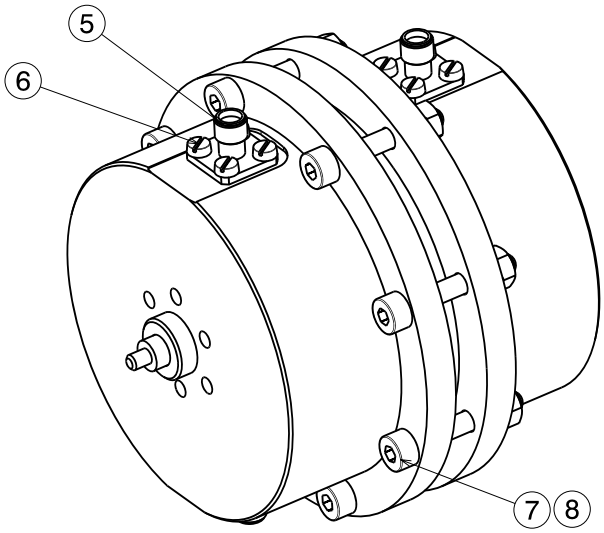

Figure 4.8 – Isometric view of the sensor. 5 is the SMA coupler, 6 the bolts used to fix the coupler to the main body and 7,8 the nuts and bolts used to put together the two parts of the main body.

the rigidity of the sensor will be larger, the displacement will be smother. A CAD model of the membrane actuator is shown in fig. 4.11.

This sensor should be capable of detecting the displacement of the connecting rod without the stick-slip effect observed in the previous prototype. As a drawback a larger force will be required to deform the membrane in order to create a certain frequency shift.

A very interesting spin-off of this design would be a differential pressure sensor. In this case, the displacement of the transducer would be caused by a non-conducting, low dielectric losses fluid. It should be possible to obtain extremely accurate measurements of the pressure in very rough environments.

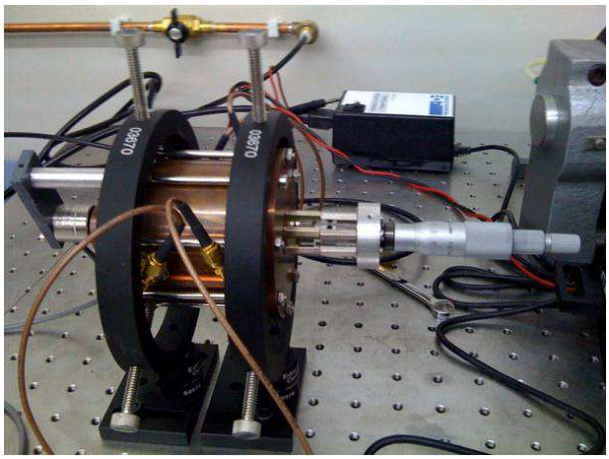

Figure 4.9 – Experimental set up

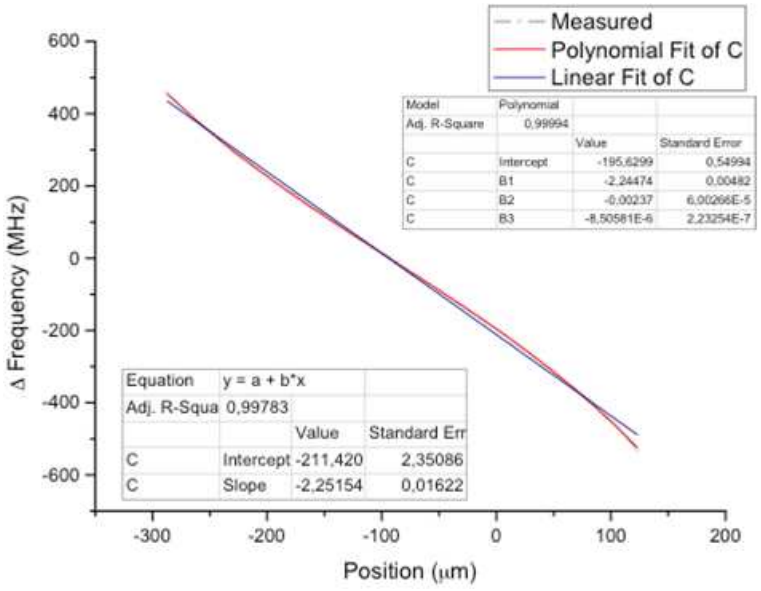

Figure 4.10 – Results of the measurements

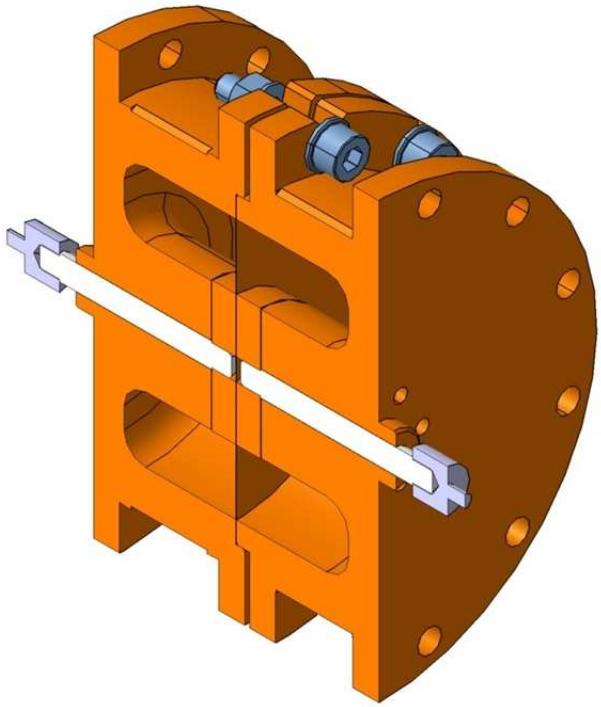

Figure 4.11 – Membrane based design

CHAPTER 5

Acceleration in drift tube linacs and longitudinal beam dynamics

The objective of this chapter is to describe the environment in which the PMQs will operate and to describe the alternatives existing for the transverse focusing in an accelerating structure. We will start by looking at how the electrical field is generated in a RF cavity, we will then describe how the particles are accelerated by an electrical field, and how this field is practically applied in an accelerating gap. Afterwards, we will give a very rude description of a drift tube linac and we will end the chapter with a more detailed description of the longitudinal dynamics in a series of accelerating gaps.

5.1 Application of resonant cavities for particle accelerators

The particles will pass through most cavities in a longitudinal channel defining the beam trajectory. The effect of the cavity in the beam will be determined by the characteristics of the electrical, and to a lesser extent the magnetic, fields along this longitudinal channel. These properties are the on-axis ones of the cavity. When the cavity is used for accelerating particles, the most important parameter of the cavity is the on-axis voltage, which may be defined as the maximum integrated electrical field on the axis of the beam passage. Other cavity parameters may then be related to the on-axis voltage.

In order to relate the losses in the cavity to the on axis voltage, the losses are modeled as due to a resistance placed in parallel to the voltage of the gap, i.e., a shunt resistance. In a more quantitative way, the *shunt impedance* r_S gives an idea of the amount of power that must be dissipated in order to establish a certain on-axis voltage V_0.

$$r_s = \frac{V_0^2}{P} = Q\frac{V_0^2}{\omega U} \tag{5.1}$$

Very often the value used for r_s is half that of eq. 5.1. In this case, the shunt impedance is the same that the actual shunt impedance in the cavity equivalent circuit. [1]. This expression does not take into account the effectiveness of the created voltage, as the real acceleration should include not only the voltage but the transit time factor, see eq. 5.12, which will be defined in the next chapter. This is provided by the *effective shunt impedance*, r.

[1] Electrical engineers should be aware that in the microwave world, most often the peak value of the oscillating magnitudes is used instead of the rms value. Therefore the discrepancy of a factor 2, to obtain the power.

$$r = \frac{(V_0 T(\beta))^2}{P} = r_s T^2(\beta) \tag{5.2}$$

It is obvious that the effective shunt impedance of the cavity will depend on the particle speed through the time transit factor. The *r over Q* parameter is the ratio of the effective shunt impedance and the quality factor, it is only a function of the geometry, and it is independent of the material used for building the cavity.

$$\frac{r}{Q} = \frac{(V_0 T)^2}{\omega U} \tag{5.3}$$

With the above definitions is possible to obtain a cavity equivalent circuit near each resonant mode. The equivalent circuit is shown in fig. 5.1.

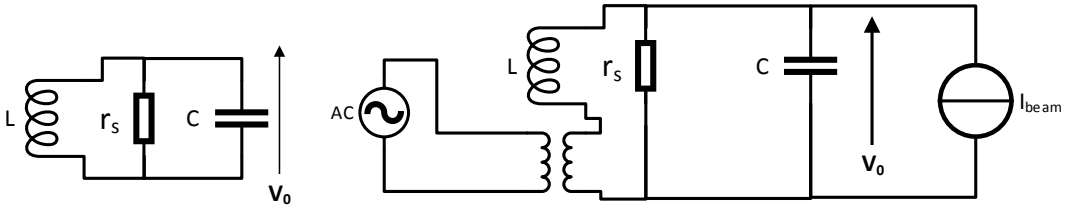

Figure 5.1 – Left, parallel equivalent circuit of an unloaded resonant cavity near a certain mode. Right, the same cavity but loaded with the beam current and including power injection from a source through a magnetic coupling.

The equivalent parameters may be obtained from a FEM simulation by equating the resonant frequency to $1/\sqrt{LC}$, the total stored energy to $1/2CV_0^2$, when the on-axis field is normalized to provide V_0 and using the shunt impedance of 5.1.

Any practical cavity will require some power injection through an aperture, and in the case of accelerator cavities, the component of the beam current at the resonant frequency will apply a load to the cavity. The equivalent circuit is shown as well in fig. 5.1

5.2 Acceleration in a RF gap

As it is well know, the acceleration of a charged particle must be performed by the electrical field. The magnetic field, as it creates a force perpendicular to the velocity, cannot change the particle energy. Performing the scalar product of the Lorentz law by the velocity, we obtain,

$$\vec{v} \cdot \frac{d\vec{p}}{dt} = -q\vec{v} \cdot \vec{\mathcal{E}} = q\vec{v} \cdot \left(\frac{\partial \vec{A}}{\partial t} + \nabla V \right) \tag{5.4}$$

It is interesting to note, that the electrical field may be created either from static charges or a changing magnetic field. This second case of acceleration is used in the betatron or in the induction linac, and it is expressed in eq. 5.4 by the time derivative of the vector potential.

We should now move to the more general case of the acceleration of one particle as it moves along a gap in a radiofrequency structure. The variation of voltage per unit length of a certain particle will be the electrical field seen by that particle at a certain position and instant.

$$\frac{dV}{dz} = \mathcal{E}(z, r, t) \tag{5.5}$$

We will assume that the particle is traveling very near the axis and that the on-axis field may be decomposed in a time variation of angular frequency ω and an spatial component corresponding to the maximum temporal value of the field. In this case, we can write

$$\frac{dV}{dz} = e(z)\cos(\omega t + \phi_s) \tag{5.6}$$

The limits of the integral must extend to a region where the electrical field of the gap is negligible. This formalism may be extended to a multi-gap structure, in which case the limits would be outside of the RF cavity.

We have introduced a synchronous phase to model particles that are not at the origin when the peak field is maximum. ϕ_s may be seen as the phase of a given particle at the origin. We will suppose, in addition, that the variation of energy in the gap is relatively small, so that the particle will be at a certain average velocity in the gap that we will call v. Under this assumption, the particle will be at position z at time z/v and the expression for the voltage variation in the gap may be integrated in z.

$$\Delta V = \int e(z)\cos\left(\omega\frac{z}{v} + \phi_s\right)dz = \int e(z)\cos\left(\omega\frac{z}{v}\right)\cos\phi_s dz - \int e(z)\sin\left(\omega\frac{z}{v}\right)\sin\phi_s dz \tag{5.7}$$

We will know express the voltage gain equation in complex form,

$$\Delta V = \Re\left(e^{j\phi_s}\int e(z)\exp\left(j\frac{\omega}{v}z\right)dz\right) \tag{5.8}$$

We easily recognize the Fourier transform of the electrical field[2], that we will denote as $\mathfrak{e}$.

$$\Delta V = \Re\left(e^{j\phi_s}\mathfrak{e}\left(\frac{\omega}{v}\right)\right) \tag{5.9}$$

Usually the magnitude ω/v is expressed in a slightly different way,

$$\frac{\omega}{v} = \frac{2\pi f}{v} = \frac{2\pi}{\beta\lambda} \tag{5.10}$$

Where $\beta\lambda$ is the space that a particle traverse during an RF time. In addition, we will take the modulus of the expression given by eq. 5.9 to obtain,

$$\Delta V_{max} = \left|\mathfrak{e}\left(\frac{2\pi}{\beta\lambda}\right)\right| \tag{5.11}$$

As an example of the use of the Fourier transform and eq.5.11 we will use the case of a double spoke cavity that was calculated by the author for a preliminary design of ESS-Bilbao [1], [41]. The main dimensions of the cavity may be seen in 5.2.

[2]Depending on the convention adopted, a normalizing factor $1/\sqrt{2\pi}$ is used in the definition of the Fourier transform. This factor is useful in order to have more symmetrical inverse Fourier transform. We prefer not to use it here for clarity

The RF problem of the resonant mode in the cavity was solved and the on-axis electrical field could be extracted. This electrical field was scaled to obtain the maximum allowed electrical field in the cavity surface. The result may be seen on the left of fig. 5.3. Once this electrical field is obtained, it is possible to calculate the maximum accelerating voltage as a function of the particle velocity by using eq. 5.11. The result is shown on the right of fig. 5.3.

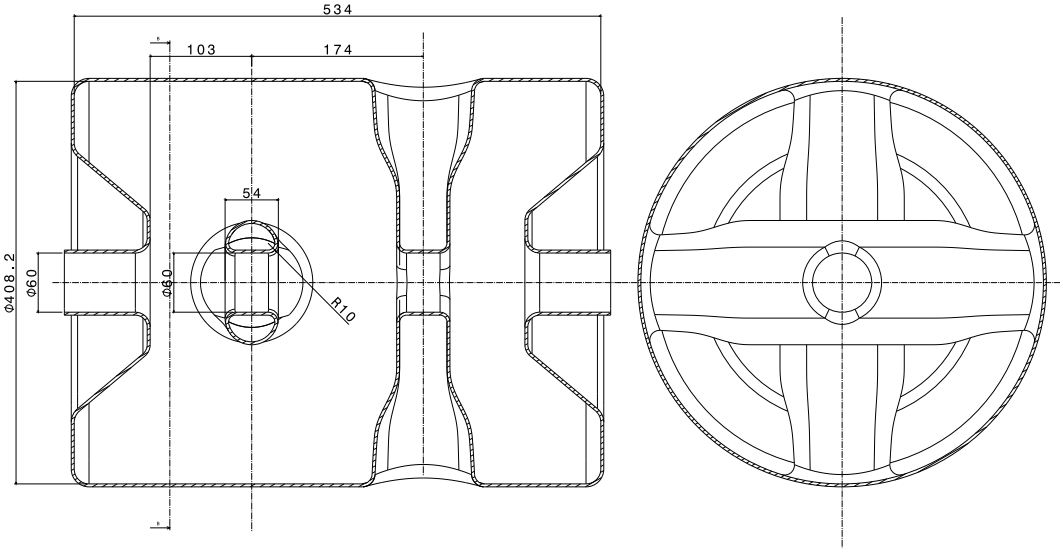

Figure 5.2 – Main dimensions [mm] of the designed double spoke

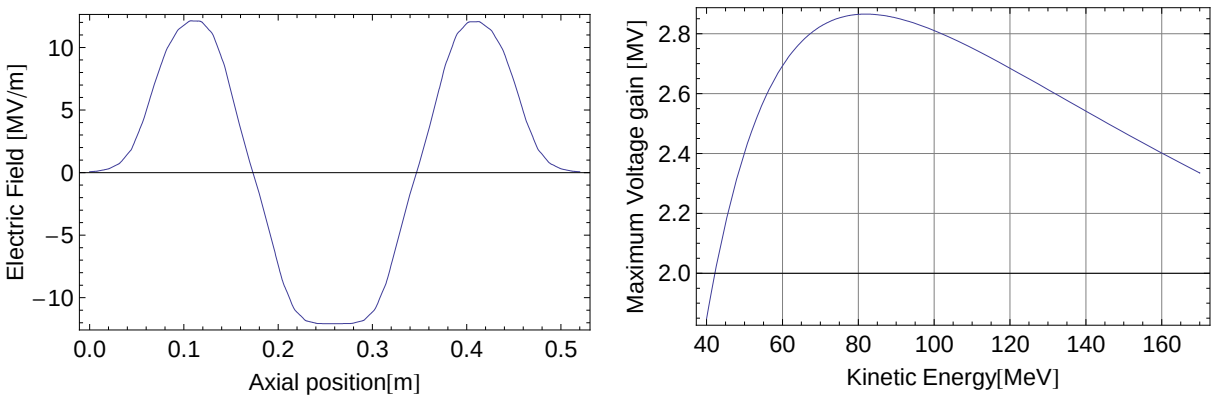

Figure 5.3 – DSR Cavity. Left, on-axis peak voltage of the cavity. Right, available accelerating gradient in the range of interest.

Although equation 5.11 is very general and may be used for obtaining the accelerating voltage for a large range of problems, normally a simpler approach is taken for a single gap acceleration. Typically, the gap is supposed symmetrical around the point $z = 0$, so that the sinus term may be drop from eq. 5.7. We define then a transit time factor T, which will depend on the particle velocity as,

$$T(\beta) = \frac{\int e(z) \cos\left(\frac{2\pi}{\beta\lambda} z\right) \, dz}{\int e(z) \, dz} \tag{5.12}$$

With this definition, the acceleration in the gap will be,

$$\Delta E = eV_0 T(\beta)\cos\phi_s \tag{5.13}$$

, which is called the Panoffsky equation. In spite of its simplicity, the Panoffsky equation summarizes the effect of the accelerating gap on any given particle by quantifying the different effects affecting the acceleration, the strength of the coupling of the particles of the beam to the electrical field, e, the absolute strength of the accelerating gap, V_0, the adequacy of the matching of the particle speed to the gap size, T and finally the relative phase between the pass of the particle through the gap center and the electrical phase.

5.3 Structure of a linac

Normally a single gap or even a single cavity is not enough to boost the energy of the beam to the desired energy. For this, a structure of several cavities placed along a linac or a circular accelerator, as was described in the introduction is required. A linac is an accelerator in which the particles are not recirculated through the same cavities several times. Each gap in a linac will receive a beam of a certain energy and will provide a well defined increase of energy. With this boost of energy, the particle will reach the center of the next accelerating gap at the required time.

In any multi-gap accelerating structure, it is necessary that each bucket is at the center of a gap during the phase when the electric field is positive. As we will see later, the reference particle passes through the center of each gap at a constant phase, receiving just enough acceleration to pass through the center of the next gap at the same electric field phase. Depending of the type of RF structure, the relative phase between adjacent gaps is not necessarily zero (or 2π), therefore some of the gaps will be empty of particles. The RF structure may be classified according to the phase advance per gap. This situation is shown in fig. 5.4.

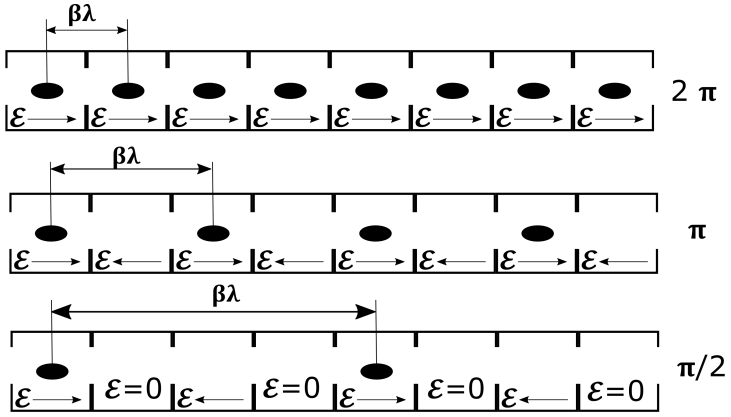

Figure 5.4 – Different cases of phase advance per gap

Although not all the gaps are occupied at any certain time, the buckets will be accelerated in all the gaps, as the structure must be build so that the time to reach any empty gap is

equal to the time required for the field to change to the accelerating synchronous phase. A principle that we will define later as the zeroth order of the longitudinal dynamic.

It is important to note that the widely used expression $\beta\lambda$, just represents the distance traversed by the beam in a single RF period, in this sense, λ must be understood as the free space wave length of an electromagnetic wave of frequency $\omega = c/\lambda$.

The distance between gaps must be increased along the linac to cope with the increasing value of the particle speed, β. For ions and low energy electrons, this means that the profile of the particles speed is linked to the linac gap position and dimension along its structure. Nevertheless, for ultra-relativistic particles, as it is normally the case for electrons, the gap may be kept constant, as the increase of energy is not associated to a significant acceleration, as the speed is saturated to value of the light one.

The linac design requires then to calculate the acceleration at each gap and to distribute the different gaps at the appropriate position. In practice this requires a software, like Parmila or GenDTL [21], that may import the data of a RF analysis program, normally SUPERFISH [54], and transport the beam along the accelerating structure. These codes, normally also allow to compute the transversal behavior of the beam along the linac, a subject to be treated on the next chapter.

PMQs are typically used in drift tube linacs (DTL) structures. The basic structure of a DTL may be seen in fig. 5.5. The structure is resonating in a 2π mode, i.e. the field repeats a complete cycle when the bunch is in the next accelerating gap. During the field reversal, the particles are screened from the decelerating field by a drift tube, in which the absolute value of the electrical field is very low. In such a way, the neat effect is accelerating.

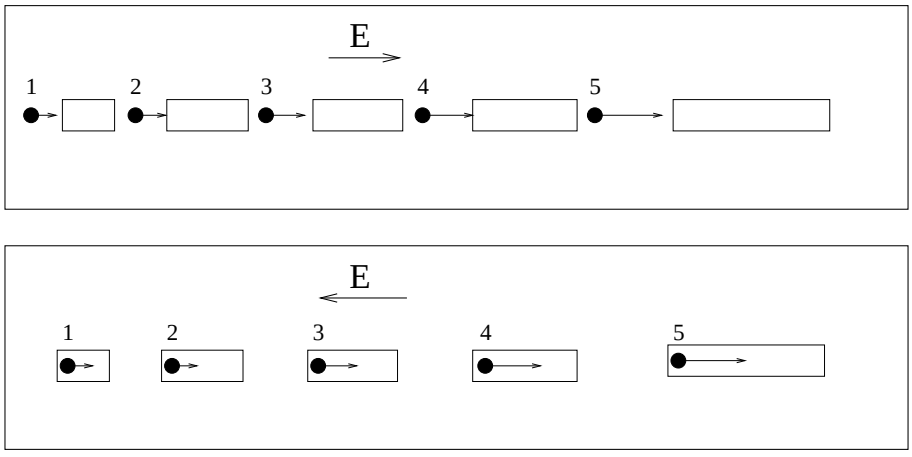

Figure 5.5 – Basic structure of a DTL. Up, position of the particle bunches during the accelerating phase of the electrical field. Down, position of the particle bunches during the decelerating phase of the electrical field

As it is indicated in fig. 5.5, the length and spacing of the drift tubes must be increased along with the velocity of the particles, so that the particles are at the same phase of the electrical field when they are at the center of the gap.

5.4 Longitudinal dynamics

5.4.1 A trick to get the relativistic derivatives

It is quite often necessary to obtain the relationship between the variation of the different relativistic parameter. How does the velocity change with energy?, or the momentum with velocity? In this section, a method is presented that allow to quickly calculate these derivatives.

First of all, we should consider that the velocity, the total energy and the momentum are represented by the adimensional relativistic parameters, β, γ and $\beta\gamma$, respectively, because we can write,

$$v = \beta c \tag{5.14}$$
$$E = \gamma m c^2 \tag{5.15}$$
$$p = \beta\gamma m c \tag{5.16}$$

Then, all the relativistic parameters may be related to the *rapidity*, u by the following equations,

$$\beta = \tanh u \tag{5.17}$$
$$\gamma = \cosh u \tag{5.18}$$
$$\beta\gamma = \sinh u \tag{5.19}$$

And it is much quicker to obtain the desired relationships by passing through the rapidity. For example, for the analysis of the longitudinal dynamics, we need to know how the speed of a particle changes with its energy, we can proceed in the following way,

$$\frac{d\beta}{d\gamma} = \frac{d\beta/du}{d\gamma/du} = \frac{1/cosh^2 u}{\sinh u} = \frac{1}{\beta\gamma^3} \tag{5.20}$$

Obtaining this expression without using the rapidity would require significantly more algebra. In addition, the rapidity is very interesting in itself, as it represents the hyperbolic angle that appears in the Lorentz transform and it is an additive parameter when combining relativistic boosts. A lovely description of this subject may be seen in [20]. Of course, solving relativistic problems using hyperbolic triangles instead of Lorentz transforms is technically inferior, but it has the appeal of the graphical methods, in which the relationship between several magnitudes is easier to appreciate. A similar problem occurs when solving spherical triangles using the Bessel formulae instead of vectors on the unit sphere. The first approach has the advantage of giving a visual interpretation of the problem, at the expense of having an incertitude on the quadrant of the inverse trigonometric functions.

5.4.2 Equations of the longitudinal dynamics

The longitudinal dynamics of a linac analyzes the difference in energy and phase of transit through an accelerating particle of an arbitrary particle with respect to the synchronous particle. The synchronous particle is defined as the one that passes through the accelerating gaps at the synchronous phase, ϕ_s, and has just the right energy, E_s, to reach the following gap again at the synchronous phase. The fact that the linac is built in such a way that a certain (synchronous) particle arrives always at every gap on the same phase is the zeroth order dynamics of the longitudinal movement[3]. For all other particles we define the phase error, $\delta\phi$, and the energy error, δE, so that their phase of arrival and energy at a certain gap is given by [4],

$$\phi = \phi_s + \delta\phi \tag{5.21}$$

$$E = E_s + \delta E \tag{5.22}$$

The longitudinal dynamics equations provide us with two relationships, how does the energy error of a particle change for a certain phase error and how does the phase error change for a certain energy error. For answering the first question we introduce eq. 5.22 in the Panoffsky equation,

$$\Delta E = qTV_0 \cos(\phi_s + \delta\phi) = qTV_0 \cos\phi_s \cos\delta\phi - qTV_0 \sin\phi_s \sin\delta\phi \tag{5.23}$$

The obtain the change of δE, we have to subtract the energy gain of the synchronous particle,

$$\Delta\delta E = \Delta E - \Delta E_s = \Delta E_0 \left[\cos\phi_s (\cos\delta\phi - 1) - \sin\phi_s \sin\delta\phi\right] \tag{5.24}$$

, which answers the first of the questions. We have called ΔE_0 to the maximum available energy gain per gap.

For answering the second question we will consider that the distance between gaps is l_g and the radiofrequency has an angular velocity of ω_{RF}, in this case, the difference in time to arrive to the gap between the synchronous and the arbitrary particle will be,

$$\delta t = \frac{l_g}{c}\left(\frac{1}{\beta} - \frac{1}{\beta_s}\right) = \frac{l_g}{c}\frac{\beta_s - \beta}{\beta_s\beta} = -\frac{l_g}{c}\frac{\delta\beta}{\beta_s\beta} = -\frac{l_g}{c}\frac{d\beta/d\gamma \cdot \delta\gamma}{\beta_s\beta} = -\frac{l_g}{c}\frac{\delta\gamma}{\beta_s\beta^2\gamma^3} \tag{5.25}$$

, in which we have used eq. 5.20. The variation in phase will be then,

$$\Delta\delta\phi = -\frac{l_g\omega_{RF}}{c}\frac{\delta\gamma}{\beta_s\beta^2\gamma^3} = -\frac{l_g\omega_{RF}}{c}\frac{\delta E}{mc^2\beta_s\beta^2\gamma^3} \tag{5.26}$$

[3] In the same way that the fact that a certain particle passes through the center of the quadrupoles and it is bent by the nominal angle by the dipoles is the zeroth order dynamics of the transverse movement

[4] We use the letter δ to represent the error with respect to the synchronous particle in order to reserve d as the derivative of this error and Δ to the variation of the error

For a 2π type cavity, l_g is $\beta_s\lambda$ and eq. 5.26 may be expressed as,

$$\Delta\delta\phi = -2\pi\frac{\delta E}{mc^2\beta^2\gamma^3} \approx -\pi\frac{\delta E}{E} \tag{5.27}$$

, where the approximation is to the non-relativistic case, in which $\gamma \to 1$ and $E \to 1/2mc^2\beta^2$. We will use in the following the non relativistic equation, although it is very simple to revert to the fully correct one by replacing the kinetic energy by the right term of eq. 5.27. Nevertheless, we retain the approximate expression because it provides a very neat and easy to remember quantification of the phase shift with energy error, i.e. a one per one error in energy gives a phase increment of $-\pi$.

Eqs. 5.24 and 5.27 form a set of coupled equations that provide the behavior of all particles having an error on energy or phase with respect to the synchronous particle. In fig. 5.6, we can see a tracking performed on a certain structure for several values of energy error. As we may see, above a certain energy error, the particle is lost.

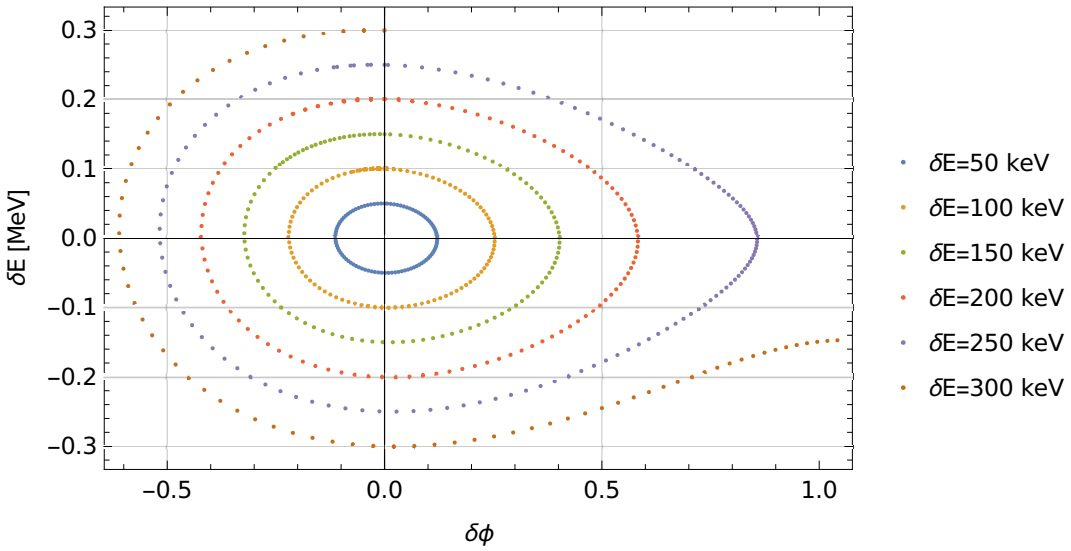

Figure 5.6 – Tracking of a set of particles with different energy errors. The nominal energy is 20 MeV, the acceleration per gap 50 keV and the synchronous phase -30°.

To analyze what is happening, we will replace the difference equations 5.24 and 5.27 by a pair of coupled differential equations, supposing that the gap number n is a continuous variable.

$$\frac{d\delta E}{dn} = \Delta E_0\left[\cos\phi_s\left(\cos\delta\phi - 1\right) - \sin\phi_s\sin\delta\phi\right] \tag{5.28}$$

$$\frac{d\delta\phi}{dn} = -\pi\frac{\delta E}{E} \tag{5.29}$$

This coupled system may be obtained from the Hamiltonian of eq. 5.30 assuming that $\delta\phi$ and δE are the generalized coordinate and momentum respectively.

$$H = -\Delta E_0 \left[\cos\phi_s \left(\sin\delta\phi - \delta\phi\right) + \sin\phi_s \cos\delta\phi\right] - \frac{\pi}{2E}\delta E^2 \tag{5.30}$$

Because the Hamiltonian is not explicitly dependent on n, it will be a constant of movement, and therefore we can plot in the phase space curves of constant H that will be the trajectories of the particles. This is made in fig. 5.7.

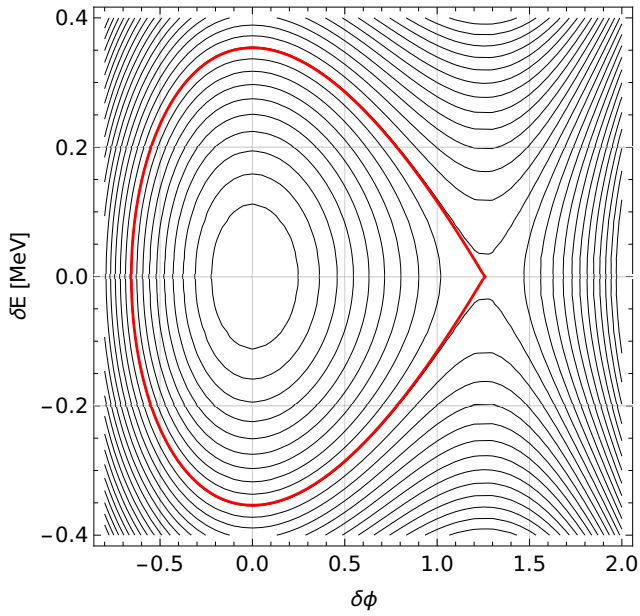

Figure 5.7 – Longitudinal phase space for E=20 MeV, ΔE_0=50 kEV and $\phi_s = -30°$. The separatrix is explicitly indicated.

There are two types of trajectories, some of them are trapped and rotate around the synchronous point, the other trajectories are not trapped and have an unbounded change of $\delta\phi$. Both trajectory families are separated by a singular trajectory which is called the separatrix. All the points inside the separatrix will have a stable oscillation around the synchronous trajectory, while all the other points will be lost during the acceleration. The area inside the separatrix is called the bucket and defines the acceptance of the accelerating structure in the longitudinal dynamics. To obtain the equation of the separatrix, we use the fact that it is the phase space trajectory that passes trough the unstable stationary point of the Hamiltonian, which is located on the apex of the separatrix. In this points, the differential equations are zero, so that the point is stationary,

$$\frac{d\delta E}{dn} = \Delta E_0 \left[\cos\phi_s \left(\cos\delta\phi - 1\right) - \sin\phi_s \sin\delta\phi\right] = 0 \tag{5.31}$$

$$\frac{d\delta\phi}{dn} = -\pi\frac{\delta E}{E} = 0 \tag{5.32}$$

This is fulfilled when δE is zero and $\delta\phi$ is $-2\phi_s$. We will call this value as $\delta\phi_\alpha$. The fact that this solution corresponds to an unstable stationary point may be proved by the fact that the Jacobian matrix of the differential equation set has two eigenvalues of opposite sign at

$(\delta\phi_\alpha, 0)$, and it is therefore a saddle point [30]. The value of the Hamiltonian function t the separatrix is,

$$H_\alpha = -\Delta E_0 \left(2\phi_s \cos\phi_s - \sin\phi_s\right) \tag{5.33}$$

, and the implicit equation defining it will be,

$$H_\alpha = -\Delta E_0 \left[\cos\phi_s \left(\sin\delta\phi - \delta\phi\right) + \sin\phi_s \cos\delta\phi\right] - \frac{\pi}{2E}\delta E^2 \tag{5.34}$$

The area of the bucket will be reduced with the synchronous phase approaching zero, so that $\cos\phi_s \to 1$. In other words, if we try to get the maximum energy gain per gap, the longitudinal acceptance will be zero , and only the synchronous particle will be accelerated. In fig. 5.8, we can observe the reduction of the phase space area as the synchronous phase approaches zero, where the maximum energy boost of the synchronous particle may be reached.

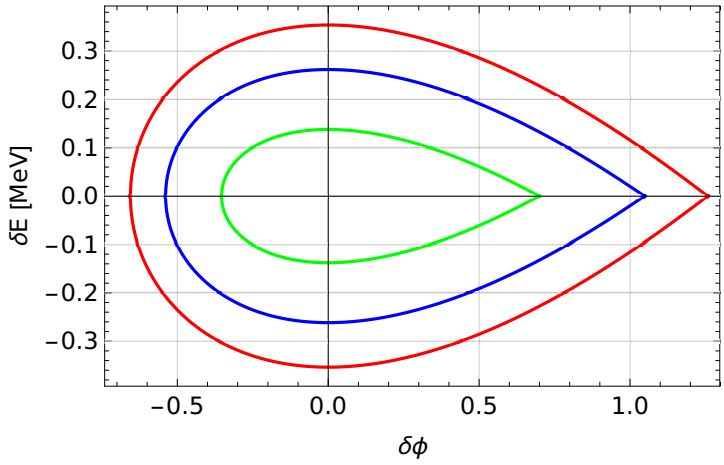

Figure 5.8 – Several separatrices for E_0=20 MeV, ΔE=50 keV. The values of ϕ_s are -36°, -30° and -20°

The same situation may be seen in the accelerating voltage plot of fig. 5.9. We may observe there the symmetry of the synchronous phase and the apex of the separatrix. Obviously, a particle that sits at the apex and has zero energy error receives just the energy to stay in the same position after one gap, but in an unstable way.

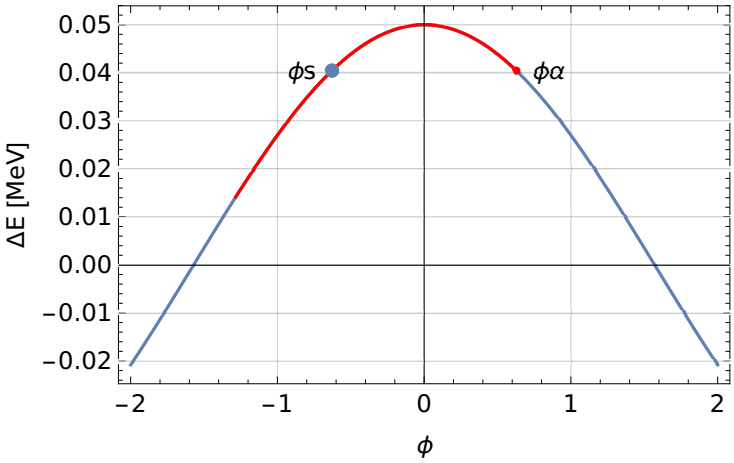

Figure 5.9 – Accelerating voltage over phase. The stable region for δE =0 is indicated in red.

CHAPTER 6

Transverse dynamics

In any accelerator system, the beam will have a certain amount of transverse momentum that if not controlled will cause the beam to increase in size until the mechanical aperture of the system is exceeded and the beam is lost to the walls of the vacuum chamber. In order to avoid the loss of the beam, it is necessary to study and control this lateral expansion of the particles. This is the subject of the transverse dynamics.

In this chapter, we will study the main equations ruling the transversal movement of the particles. We will start by providing the equations that control the displacement of the particles with respect to the ideal trajectory that the beam designer has planned for its accelerator. We will analyze, as well the effect of this movement on complete regions of phase space, and not only for any single particle.

A significant contribution of the present work is on the complex formalism of linear beam dynamics. The fact that the two degrees of freedom defining a phase space ellipse in beam dynamics may be grouped in just one complex number has been known since a long time. Nevertheless, to the author's knowledge, only the transformation of the phase ellipse through a drift space or a thin lens has been obtained. In this work, a general formulation is presented, the relationship with the commonly used Twiss parameters is given and some interesting uses of this new formulation are proposed.

The chapter will end with one application of the transversal beam dynamics, the analysis of ion species using a magnetic spectrograph. I will describe the design of a spectrograph of extremely large acceptance, that was designed by the author using a fully non-linear method.

6.1 The magnetic and electrical rigidity

6.1.1 The magnetic rigidity

From the magnetic term of Lorentz's law, the variation of the momentum with time may be expressed as,

$$\frac{d\vec{p}}{dt} = q\vec{v} \times \vec{B} \tag{6.1}$$

We can replace the derivative with respect to time by the derivative with respect to the trajectory length, s.

$$\frac{d\vec{p}}{ds}\frac{ds}{dt} = \frac{d\vec{p}}{ds}v = q\vec{v} \times \vec{B} \tag{6.2}$$

As the velocity vector may be expressed as the product of its modulus v and the unitary tangent vector $\vec{\tau}$, we can write,

$$\frac{d\vec{p}}{ds} = q\vec{\tau} \times \vec{B} \tag{6.3}$$

The first term may be simplified by expressing, again, the momentum as its modulus times the unitary tangent vector and applying Frenet's first equation of curves and the fact that the modulus of the momentum does not change because the magnetic field cannot modify the energy of the particle,

$$\frac{d\vec{p}}{ds} = \frac{d(\vec{p\tau})}{ds} = p\frac{d\vec{\tau}}{ds} + \tau\frac{dp}{ds} = p\frac{\vec{n}}{\rho} \tag{6.4}$$

Where $\vec{n}$ is the unitary normal vector and ρ is the radius of curvature. The magnetic induction may be separated in its tangential component B_t, colinear with $\vec{\tau}$, and its normal component, B_n, colinear with $\vec{n}$.

We obtain finally,

$$B_n\rho = \frac{p}{q} = \eta_m \tag{6.5}$$

Eq. 6.5 allows to define a new magnitude, the *magnetic rigidity* η_m; which is the quotient of the momentum and the charge and represents how the inertia of the particle will oppose to being bent, $1/\rho$, by a given magnetic field, B_n, perpendicular to the trajectory.

6.1.2 The electrical rigidity

A similar calculation may be performed for the effect of the electrical field on the particle trajectory.

$$\frac{d\vec{p}}{dt} = q\vec{E} \tag{6.6}$$

The derivation is slightly longer because the electrical field may change the modulus of the momentum of the particle. We will have now,

$$\left(\frac{dp}{ds}\vec{\tau} + p\frac{d\vec{\tau}}{ds}\right)v = q\vec{E} \tag{6.7}$$

We can now separate eq. 6.7 into its normal and tangential components, $\vec{E} = E_t\vec{\tau} + E_n\vec{n}$.

$$v\frac{dp}{ds} = qE_t \tag{6.8}$$

$$\frac{pv}{\rho} = qE_n \tag{6.9}$$

Eq. 6.8 is only the projection of the electrical field in the direction of the trajectory, the only component doing work on the particle; while eq. 6.9 describes how the shape of the trajectory changes. We can define an *electrical rigidity*, η_e in analogy with the magnetic rigidity.

$$\eta_e = E_n \rho = \frac{pv}{q} \tag{6.10}$$

It is interesting to note that in the non-relativistic regime, pv is twice the kinetic energy of the particle, which in turn is proportional to the total accelerating voltage, V, seen by the particle from the source times the charge. As the charge cancels in the numerator and the denominator the electrical rigidity is $2V$, independently of the charge or the mass of the particle. This is a very interesting property of electrostatic lenses, that are often used at low energies. In this case, if the voltage of the lenses is proportional to the voltage used to accelerate the particles, the beam dynamics will not depend on the beam energy. This solution is very cost effective, as the lenses voltage may be obtained by resistive dividers from the main high voltage power supply.

In the relativistic case, the expression is a bit more complicated,

$$\eta_e = \frac{pv}{q} = \frac{mc^2\gamma\beta^2}{q} = \frac{mc^2}{q}\left(\gamma - \frac{1}{\gamma}\right) = V\frac{2mc^2 + T}{mc^2 + T} \tag{6.11}$$

From where is evident that at low energies $\eta_e \approx 2V$ while at ultrarelativistic energies, $\eta_e \approx V$.

6.2 The paraxial particle equations

It is customary in beam analysis to define a reference particle that has the following properties,

1. It has exactly the nominal magnetic rigidity, so that it is bent by the dipoles exactly the nominal angle
2. It passes exactly through the center of the quadrupoles, so that they have no effect on the reference particle

Although it is not a common use, we will call the analysis of the trajectory of the reference particle, the zeroth order dynamic. The analysis of the movement of all other particles will be made on a moving system which has its z axis in the direction of the reference particle velocity, and the x and y axes in a plane perpendicular to the velocity. Normally, x is contained in the horizontal plane and y is vertical, although this is not always the case, specially for transfer lines, in which a vertical displacement of the reference trajectory is often required.

The reference system we will be using may be seen in fig. 6.1. The reference system is moving with the synchronous particle, the z axis is parallel to the trajectory, the x axis is the plane in which the particle is being bent (the dispersive plane as we will see later), and the y axis is perpendicular to the other two.

We will use, as well, the paraxial approximation, which is used when the longitudinal component of the momentum is much larger than the transverse ones. In that case, the curvature is equivalent to the second derivative of the transverse displacement with respect to the longitudinal coordinate,

$$\frac{d^2x}{dz^2} \approx -\frac{1}{\rho} \tag{6.12}$$

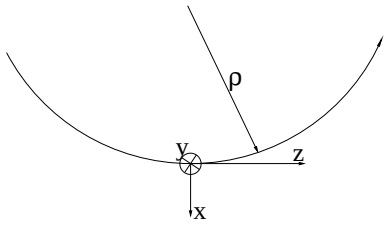

Figure 6.1 – Definition of the axes used in the derivation of the equations of movement

In addition, only the longitudinal velocity couples with the magnetic field to produce Lorentz force,

$$F_x = -\beta c B_y \tag{6.13}$$

$$F_y = \beta c B_x \tag{6.14}$$

The magnetic field may be expanded to first order around the synchronous particle, because there is no bending of the synchronous particle in the y axis, $B_{y0} = 0$.

$$B_x = B_{x0} + \frac{\partial B_x}{\partial x} x + \frac{\partial B_x}{\partial y} y \tag{6.15}$$

$$B_y = \frac{\partial B_y}{\partial x} x + \frac{\partial B_y}{\partial y} y \tag{6.16}$$

Because we want to express the equations of movement with respect to a rotating system, the one defined by the synchronous particle, we have to include two types of inertial forces, the centrifugal force and the Coriolis force. The angular velocity of the synchronous system is,

$$\vec{\Omega} = -\omega \vec{j} = -\frac{\beta c}{\rho} \vec{j} \tag{6.17}$$

For computing the effect of the Coriolis force, we need to know the value of the relative velocity of the particle with respect to the non-inertial frame. The relative velocity is due to the off-axis components of the speed and to the fact that a particle at synchronous speed but not located at the proper radius ρ, will have a difference between the drag velocity at this point and the actual velocity. The relative velocity will be,

$$\vec{v_r} = \frac{dx}{dt} \vec{i} + \frac{dy}{dt} \vec{j} - \omega x \vec{k} \tag{6.18}$$

The last term in eq. 6.18 is the one due to the mismatch between the frame velocity at the particle radius, $\omega\,(\rho + x)$, and the actual velocity of the particle, which is the synchronous one, $\omega\rho$.

The Coriolis force may then be computed as,

$$\vec{F}_{cor} = 2\gamma m \vec{v_r} \times \vec{\Omega} = -2\gamma m \left(\frac{dx}{dt}\vec{\imath} + \frac{dy}{dt}\vec{\jmath} - \omega x \vec{k} \right) \times \omega \vec{j} = -2\gamma m \left(\omega \frac{dx}{dt}\vec{k} + x\omega^2 \vec{i} \right) \tag{6.19}$$

The Coriolis force due to the relative velocity, dx/dt , may be neglected, because it is oriented in the longitudinal direction. The Coriolis force due to the relative velocity, dy/dt , is zero, because the relative velocity and the frame angular velocity are parallel. The effect of the offset in the x axis is very important, ant it is the cause of the focusing effect of a dipole on the dispersive plane.

On the other hand, the centrifugal force has an important contribution, it is pointing outwards and it it given by,

$$\vec{F}_{cent} = \gamma m \omega^2 (\rho + x) \vec{\imath} \tag{6.20}$$

The interesting point is that the excess of centrifugal force due to the off-axis displacement has half the value of the due to the Coriolis force and is pointing inwards, i.e. it is a focusing force.

So that the total effect of the transverse inertial force will be,

$$\vec{F}_{inert} = \gamma m \omega^2 (\rho - x) \vec{\imath} \tag{6.21}$$

The first term is the one canceled exactly by the Lorentz forces at the reference trajectory, will the second term is the focusing force due to the bending of the beam in the dispersive plane.

Once we have determined the forces, we will now derive the equation of motion, the time derivatives, may be replaced by derivatives along the trajectory as,

$$\frac{dx}{dt} = \frac{dx}{dz}\frac{dz}{dt} = \beta c \frac{dx}{dz} \tag{6.22}$$

$$\frac{d^2x}{dt^2} = \frac{d^2x}{dz^2}\left(\frac{dz}{dt}\right)^2 = (\beta c)^2 \frac{d^2x}{dz^2} \tag{6.23}$$

The equations of movement will be,

$$\frac{d^2\vec{r}}{dt^2} = \vec{F}_{Lorentz} + \vec{F}_{inert} \tag{6.24}$$

The Lorentz forces may be obtained from the field expansion given in eq. 6.15. If we take into account the cancellation of the main term of the centrifugal force with the Lorentz force in the reference trajectory, we arrive to the following equations,

$$\gamma m (\beta c)^2 \frac{d^2x}{dz^2} = -\left(\frac{\partial B_y}{\partial x} x + \frac{\partial B_y}{\partial y} y \right) e\beta c - \gamma m \left(\frac{\beta c}{\rho} \right)^2 x \tag{6.25}$$

$$\gamma m (\beta c)^2 \frac{d^2y}{dz^2} = \left(\frac{\partial B_x}{\partial x} x + \frac{\partial B_x}{\partial y} y \right) e\beta c \tag{6.26}$$

We can now express the equations of movement in terms of the magnetic rigidity, which is the ratio between the particle momentum and the electrical charge. The result is,

$$\frac{d^2x}{dz^2} + \left(\frac{\partial B_y/\partial x}{\eta_m} + \frac{1}{\rho^2}\right)x + \frac{\partial B_y/\partial y}{\eta_m}y = 0 \tag{6.27}$$

$$\frac{d^2y}{dz^2} - \frac{\partial B_x/\partial y}{\eta_m}y - \frac{\partial B_x/\partial x}{\eta_m}x = 0 \tag{6.28}$$

We will introduce the effect of a small difference in magnetic rigidity with respect to the reference one, taking logarithmic derivatives with respect to the basic equation of the radius of curvature of the reference particle, $B\rho = \eta_m$, we obtain

$$\frac{\Delta\rho}{\rho} = \frac{\Delta\eta_m}{\eta_m} \tag{6.29}$$

, so that the change of curvature radius will be to first approximation,

$$\Delta\rho = \rho\frac{\Delta\eta_m}{\eta_m} = \rho\delta \tag{6.30}$$

, where δ is the relative error of magnetic rigidity. Because we are in para-axial approximation, we can approximate the change in the second derivative of the transverse displacement in the dispersive plane to the change in the radius of curvature. Taking a variation with respect to eq. 6.12,

$$\Delta\left(\frac{d^2x}{dz^2}\right) = \frac{\Delta\rho}{\rho^2} = \frac{\delta}{\rho} \tag{6.31}$$

We can introduce now, the additional term given in eq. 6.31 into eq. 6.27 to obtain the complete set of equations in first approximation,

$$\frac{d^2x}{dz^2} + \left(\frac{\partial B_y/\partial x}{\eta_m} + \frac{1}{\rho^2}\right)x + \frac{\partial B_y/\partial y}{\eta_m}y = \frac{\delta}{\rho} \tag{6.32}$$

$$\frac{d^2y}{dz^2} - \frac{\partial B_x/\partial y}{\eta_m}y - \frac{\partial B_x/\partial x}{\eta_m}x = 0 \tag{6.33}$$

Most accelerators are design to minimize the terms coupling the displacement in the x and y planes. This is not the case when solenoids or skew quadrupoles are used, but it is normally a good approximation in most transfer lines and circular accelerators using quadrupoles and combined function dipoles. In this case, the equations of movement reduce to the simpler,

$$\frac{d^2x}{dz^2} + \left(\frac{\partial B_y/\partial x}{\eta_m} + \frac{1}{\rho^2}\right)x = \frac{\delta}{\rho} \tag{6.34}$$

$$\frac{d^2y}{dz^2} - \frac{\partial B_x/\partial y}{\eta_m}y = 0 \tag{6.35}$$

These equations are similar to the harmonic oscillator, but with a recovering term that

depends on the position of the transfer line. It is interesting to note that in absence of bending, the recovery terms in x and y axis have the same value but opposite sign. In addition, it is important to realize that the lack of a first derivative term in the ordinary differential equation leads to the conservation of the Wronskian of the equation solution pairs.

The equation of the movement on the dispersive plane is a non homogeneous type and therefore will be composed of a general solution of the homogeneous equation plus an individual solution of the homogeneous equation. For the individual solutions of the homogeneous equation, we will take the one with has initial conditions, $x(z_1) = 1$ and $x'(z_1) = 0$, which is the cosine like solution $C(z)$ and the one which has initial conditions $x(z_1) = 0$ and $x'(z_1) = 1$, which is the sine like solution, $S(z)$. For the particular solution of the complete equation we will take the one which has $x(z_1) = 0$ and $x'(z_1) = 0$, and we will take advantage of the fact that the solution of the eq. 6.34 must be linear in δ. On the other hand, for the non-dispersive plane y, the solution will only be composed of the linear combination of another pair of cosine like and sine like solutions. We can then write,

$$x(z) = x_1 C_x(z) + x_1' S_x(z) + \delta D(z) \tag{6.36}$$
$$y(z) = y_1 C_y(z) + y_1' S_y(z) \tag{6.37}$$

It is Typically possible to solve eq. 6.34 and eq. 6.35 for individual beam line components like dipoles, quadrupoles and drift spaces. If we call, z_2 the exit point of the beamline component and z_1 the entrance point, the solutions eq. 6.38 and eq. 6.39 may be expressed in matrix form as,

$$\begin{pmatrix} x_2 \\ x_2' \\ \delta_2 \end{pmatrix} = \begin{pmatrix} C_x & S_x & D \\ C_x' & S_x' & D' \\ 0 & 0 & 1 \end{pmatrix} \begin{pmatrix} x_1 \\ x_1' \\ \delta_1 \end{pmatrix} = \mathbf{M}_{x_{12}} \cdot \begin{pmatrix} x_1 \\ x_1' \\ \delta_1 \end{pmatrix} \tag{6.38}$$
$$\begin{pmatrix} y_2 \\ y_2' \end{pmatrix} = \begin{pmatrix} C_y & S_y \\ C_y' & S_y' \end{pmatrix} \begin{pmatrix} y_1 \\ y_1' \end{pmatrix} = \mathbf{M}_{y_{12}} \cdot \begin{pmatrix} y_1 \\ y_1' \end{pmatrix} \tag{6.39}$$

In most cases, we can treat individually the movement in the dispersive and non-dispersive planes and we will often drop the x or y sub-index, indicating by the context which plane we are dealing with. It would be possible as well to combine the movement in both planes in a 5x5 matrix. The movement along a more complex beamline will be made by combining the transport along the individual components using matrix multiplication,

$$\begin{pmatrix} x_3 \\ x_3' \\ \delta_2 \end{pmatrix} = \mathbf{M}_{x_{13}} \cdot \begin{pmatrix} x_1 \\ x_1' \\ \delta_1 \end{pmatrix} = \mathbf{M}_{x_{23}} \cdot \mathbf{M}_{x_{12}} \cdot \begin{pmatrix} x_1 \\ x_1' \\ \delta_1 \end{pmatrix} \tag{6.40}$$

Giving the law of composition,

$$\mathbf{M}_{13} = \mathbf{M}_{23} \cdot \mathbf{M}_{12} \tag{6.41}$$

It is possible now to obtain the matrices $\mathbf{M}$ for many beamline components of practical

interest and solve the first order dynamic of a beamline. This is made in many standard books and we will not repeat it here.

The solution of the complete equation 6.34, may be expressed on the basis of a Green function derived from the individual solutions of the homogeneous equation. In order to obtain the appropriate Green function, we express the complete equation as,

$$x" + K(z)x = p(z) = \int_0^z p\left(\hat{z}\right) \delta\left(z - \hat{z}\right) d\hat{z} \tag{6.42}$$

, that we interpret as a linear combination of inhomogeneus terms $\delta\left(z - \hat{z}\right)$, in which each term has a weight $p\left(\hat{z}\right)$. The total solution will then be a linear combination of the individual solutions,

$$x" + K(z)x = \delta\left(z - \hat{z}\right) \tag{6.43}$$

If we integrate eq. 6.43 over z, and apply initial conditions $x(0) = 0$ and $x'(0) = 0$, we obtain that for all $z < \hat{z}$, x remains zero, will for $\hat{z}$ we have a unitary jump of the derivative,

$$x'\left(\hat{z}^+\right) - x'\left(\hat{z}^-\right) = 1 \tag{6.44}$$

We can interpret this result as saying that the function will be identically zero until $\hat{z}$ and then it will continue to evolve according to the homogeneous equation but with initial conditions $x\left(\hat{z}\right) = 0$ and $x\left(\hat{z}\right)' = 1$. This type of solution may be seen in fig. 6.2.

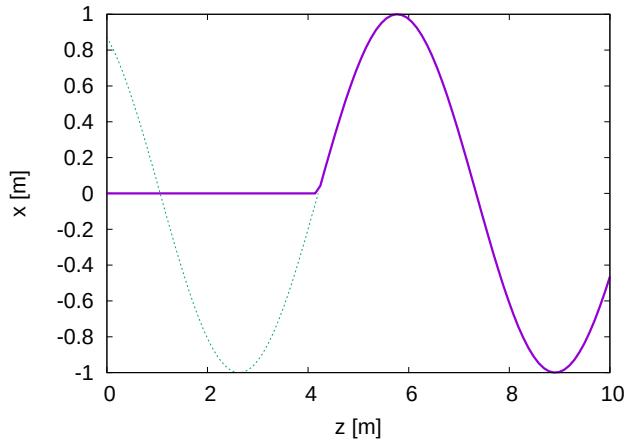

Figure 6.2 – Example of a unitary step on the derivative at around 4.1. The back-propagated initial condition may be seen in the dashed line

To obtain the solution to the impulse function, we only have to back-propagate the initial conditions at $\hat{z}$ to the origin and express the solution from this initial conditions. The back-propagated initial conditions will be,

$$\begin{pmatrix} x(0) \\ x'(0) \end{pmatrix} = M^{-1} \begin{pmatrix} 0 \\ 1 \end{pmatrix} = \begin{pmatrix} S'\left(\hat{z}\right) & -S\left(\hat{z}\right) \\ -C'\left(\hat{z}\right) & C\left(\hat{z}\right) \end{pmatrix} \begin{pmatrix} 0 \\ 1 \end{pmatrix} = \begin{pmatrix} -S\left(\hat{z}\right) \\ C\left(\hat{z}\right) \end{pmatrix} \tag{6.45}$$

, and therefore the solution will be,

$$x(z) = \begin{cases} 0 & \text{if} z \leq \hat{z} \\ -S\left(\hat{z}\right) C(z) + C\left(\hat{z}\right) S(z) & \text{if} z > \hat{z} \end{cases} \tag{6.46}$$

From here we can obtain the solution of the non homogeneous function, in terms of the Green function,

$$x = x(0)C(z) + x'(0)S(z) + \int_0^z p\left(\hat{z}\right) \left(C\left(\hat{z}\right) S(z) - S\left(\hat{z}\right) C(z)\right) \, d\hat{z} \tag{6.47}$$

On of the applications of eq. 6.47 is to obtain the dispersion function from the non homogeneous term of linear beam equation in the dispersive plane. In this case, $p(z)$ corresponds to the product of the momentum dispersion by the curvature of the nominal particle and a given point. The dispersion function is then,

$$D(z) = \int_0^z \frac{1}{\rho\left(\hat{z}\right)} \left(C\left(\hat{z}\right) S(z) - S\left(\hat{z}\right) C(z)\right) \, d\hat{z} \tag{6.48}$$

From eq. 6.48, we may see that the dispersion appears in the dipoles, which have a non infinite radius of curvature.

6.3 Twiss parameters and emittance

In many cases is not just enough to characterize the displacement of a single particle, but it is desired to describe the evolution of whole regions of the phase space. We will use the standard phase space of beam dynamics, composed of the x or y coordinate in the horizontal axis and the angles with respect to this axes, $x' = dx/dz$ or $y' = dy/dz$. These pairs of magnitudes are not really a generalized coordinate and its corresponding momentum in the sense of Hamiltonian mechanics, but are normally used as such.

The trick to do the analysis of an ensemble of particles in phase space is to parametrize a closed curve in phase space and calculate the evolution of these parameters as the particles evolve in the transport line. Because, as we know, trajectories in phase space never cross, we can be sure that all the particles that were contained inside the initial parametric curve will be contained inside the final parametric curve.

The natural choice for the closed curve is an ellipse, this is so because the transformation of an ellipse through a linear differential equation will be an ellipse again and because the parametrization is very simple.

The phase space ellipse is parametrized by eq. 6.49 [55], where the Twiss parameters, α, β and γ define the shape of the ellipse and the emittance ϵ is related to its area. In addition, it is required that $\beta\gamma - \alpha^2 = 1$ in order to keep the relationship between the emittance and the area of the phase space ellipse.

$$\gamma x^2 + 2\alpha x x' + \beta x'^2 = \epsilon \tag{6.49}$$

The relationships between the Twiss parameters and the shape of the beam space ellipse may be seen in fig. 6.3.

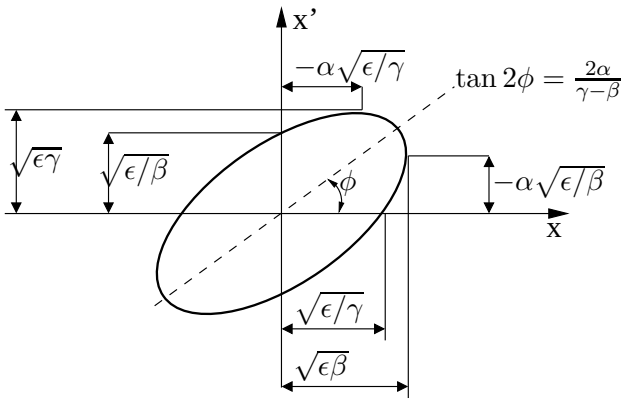

Figure 6.3 – Phase Space Ellipse with parameters

6.3.1 Transformation of the Twiss parameters through a transport line

We can define a vector $\mathbf{x}$ as,

$$\mathbf{x} = \begin{pmatrix} x \\ x' \end{pmatrix} \tag{6.50}$$

The equation of the phase space ellipse eq. 6.49 may be expressed in matrix form in the following way,

$$\begin{pmatrix} x & x' \end{pmatrix} \begin{pmatrix} \gamma & \alpha \\ \alpha & \beta \end{pmatrix} \begin{pmatrix} x \\ x' \end{pmatrix} = \mathbf{x}^T \mathfrak{T} \mathbf{x} = \epsilon \tag{6.51}$$

, where we have defined a Twiss parameter matrix $\mathfrak{T}$. To see how the Twiss parameters evolve from one point of the transport line to another, we may apply the transport matrix formalism,

$$\mathbf{x}_2 = \mathbf{M}_{12}\mathbf{x}_1 \tag{6.52}$$

and we can transform the Twiss ellipse from point 1 to 2,

$$\epsilon = \mathbf{x}_2^T \mathfrak{T}_2 \mathbf{x}_2 = (\mathbf{M}_{12}\mathbf{x}_1)^T \mathfrak{T}_2 (\mathbf{M}_{12}\mathbf{x}_1) = \mathbf{x}_1^T \mathbf{M}_{12}^T \mathfrak{T}_2 \mathbf{M}_{12} \mathbf{x}_1 \tag{6.53}$$

, so that the Twiss parameter matrix at point 1 will be given by,

$$\mathfrak{T}_1 = \mathbf{M}_{12}^T \mathfrak{T}_2 \mathbf{M}_{12} \tag{6.54}$$

And the forward transform will be given by,

$$\mathfrak{T}_2 = \mathbf{M}_{21}^T \mathfrak{T}_1 \mathbf{M}_{21} \tag{6.55}$$

, where the reverse transport matrix is given by the inverse,

$$\mathbf{M}_{21} = \mathbf{M}_{12}^{-1} = \begin{pmatrix} S' & -S \\ -C' & C \end{pmatrix} \tag{6.56}$$

We can explicitly obtain from eq. 6.55 the evolution of the Twiss parameters through a transport matrix $\mathbf{M}_{12}$.

$$\begin{pmatrix} \gamma_2 & \alpha_2 \\ \alpha_2 & \beta_2 \end{pmatrix} = \begin{pmatrix} S' & -C \\ -S & C \end{pmatrix} \begin{pmatrix} \gamma_1 & \alpha_1 \\ \alpha_1 & \beta_1 \end{pmatrix} \begin{pmatrix} S' & -S \\ -C' & C \end{pmatrix} \tag{6.57}$$

After performing the matrix multiplication, the evolution of the Twiss parameters will be,

$$\begin{pmatrix} \beta_2 \\ \alpha_2 \\ \gamma_2 \end{pmatrix} = \begin{pmatrix} C^2 & -2SC & S^2 \\ -CC' & (S'C + SC') & -SS' \\ C'^2 & -2S'C' & S'^2 \end{pmatrix} \begin{pmatrix} \beta_1 \\ \alpha_1 \\ \gamma_1 \end{pmatrix} \tag{6.58}$$

In order to obtain the differential equation ruling the evolution of the Twiss parameters, we start by expressing the generalized harmonic equation in matrix form,

$$\frac{d\mathbf{x}}{ds} = \begin{pmatrix} 0 & 1 \\ -k(s) & 0 \end{pmatrix} \mathbf{x} = \mathbf{A}\mathbf{x} \tag{6.59}$$

We can now take the derivative of the phase space ellipse equation,

$$\begin{aligned} 0 = \frac{d}{ds}\left(\mathbf{x}^T \mathfrak{T} \mathbf{x}\right) = \frac{d\mathbf{x}^T}{ds}\mathfrak{T}\mathbf{x} + \mathbf{x}^T \frac{d\mathfrak{T}}{ds}\mathbf{x} + \mathbf{x}^T \mathfrak{T} \frac{d\mathbf{x}}{ds} = \mathbf{x}^T \mathbf{A}^T \mathfrak{T}\mathbf{x} + \mathbf{x}^T \frac{d\mathfrak{T}}{ds}\mathbf{x} + \mathbf{x}\mathfrak{T}\mathbf{A}\mathbf{x} \\ = \mathbf{x}^T \left(\mathbf{A}^T \mathfrak{T}^T + \frac{d\mathfrak{T}}{ds} + \mathfrak{T}\mathbf{A}\right)\mathbf{x} \end{aligned} \tag{6.60}$$

, and we can obtain the derivative of the Twiss parameters matrix,

$$\frac{d\mathfrak{T}}{ds} = -\left((\mathfrak{T}\mathbf{A})^T + \mathfrak{T}\mathbf{A}\right) \tag{6.61}$$

From this equation, we can obtain the differential equations governing the Twiss parameters,

$$\frac{d}{ds}\begin{pmatrix} \gamma & \alpha \\ \alpha & \beta \end{pmatrix} = \begin{pmatrix} 2\alpha k & \beta k - \gamma \\ \beta k - \gamma & -2\alpha \end{pmatrix} \tag{6.62}$$

The propagation of the Twiss parameters, may then be calculates as,

$$\frac{d\beta}{ds} = -2\alpha \tag{6.63}$$

$$\frac{d\alpha}{ds} = \beta k - \gamma \tag{6.64}$$

6.4 Back to single particle trajectory: The phase advance concept.

In the previous section, we have analyzed how we can obtain the evolution of a whole phase plane region under the effect of the transport along a beam line. We have parametrized a certain region of the phase plane using the Twiss parameters and we have related the evolution of the parameters defining this region of the phase plane to the transport matrix of the single particle. In this section, we will follow the opposite approach and investigate how the evolution of a single particle may be derived from the Twiss parameters evolution. Although this may look as going backward in our analysis of the beam evolution, this is the key to introduce the effect of the perturbations in the particle dynamics. It is obvious that the non-linear forces are applied in the individual particles and not in the beam envelope as a whole, hence the interest of the formalism developed at this chapter. On the other hand, the phase advance will allow us to express the transport matrix easily in terms of the Twiss parameters.

At this stage, most textbooks start again from scratch and solve the generalized harmonic oscillator equation from scratch supposing a certain functional form of the solutions and applying it to the differential equation to obtain the solution. Here we will propose a different approach, as we already know the evolution of the Twiss parameters from eqs. 6.63. and 6.64. We will suppose that each individual particle in the phase space beam envelope is defined by a parameter ϕ_0 in the parametric equation,

$$x(s) = \sqrt{\epsilon\beta}\cos\left(\phi(s) + \phi_0\right) \tag{6.65}$$

, whose derivative will be,

$$x'(s) = -\alpha\sqrt{\frac{\epsilon}{\beta}}\cos\left(\phi(s) + \phi_0\right) + \sqrt{\epsilon\beta}\phi'(s)\sin\left(\phi(s) + \phi_0\right) \tag{6.66}$$

In order to be a valid parametrization of the movement of an individual particle in the phase space ellipse, $x(s)$ and $x'(s)$ must satisfy,

$$\gamma x^2 + 2\alpha x x' + \beta x^2 = \epsilon \tag{6.67}$$

Introducing eqs. 6.65 and 6.66 into eq. 6.67, we obtain,

$$\cos^2\left(\phi(s) + \phi_0\right) + \beta\phi'\sin^2\left(\phi(s) + \phi_0\right) = 1 \tag{6.68}$$

Obtaining the interesting result that if $\phi(s)$ is defined as,

$$\phi(s) = \int \frac{ds}{\beta} \tag{6.69}$$

, then the parametrization given by eq. 6.65 is not dependent of the individual particle ϕ_0 chosen. The change in the variable $\phi(s)$ is then just a property of the beamline and it is called, phase advance.

We can now relate the single particle evolution, the transport matrix, from one point of the beam line to another through the change of the Twiss parameters and the phase advance between then.

In order to obtain this relationship, we suppose that a certain point will be the origin of the phase, expanding eq. 6.65 and eq. 6.66 on this point, we can obtain,

$$\begin{bmatrix} x_0 \\ x'_0 \end{bmatrix} = \begin{bmatrix} \sqrt{\epsilon\beta_0} & 0 \\ -\alpha\sqrt{\frac{\epsilon}{\beta_0}} & \sqrt{\frac{\epsilon}{\beta_0}} \end{bmatrix} \begin{bmatrix} \cos\phi_0 \\ \sin\phi_0 \end{bmatrix} \tag{6.70}$$

The same expression may be obtained for the general case with a certain phase ϕ,

$$\begin{bmatrix} x \\ x' \end{bmatrix} = \begin{bmatrix} \sqrt{\epsilon\beta}\cos\phi & -\sqrt{\epsilon\beta}\sin\phi \\ -\alpha\sqrt{\frac{\epsilon}{\beta}}\cos\phi + \sqrt{\frac{\epsilon}{\beta}}\sin\phi & \sqrt{\frac{\epsilon}{\beta}}\sin\phi + \alpha\sqrt{\frac{\epsilon}{\beta}}\cos\phi \end{bmatrix} \begin{bmatrix} \cos\phi_0 \\ \sin\phi_0 \end{bmatrix} \tag{6.71}$$

It is possible to eliminate the initial phase ϕ_0 from eq. 6.70 and eq 6.71. Eq. 6.72 gives the final result of this operation.

$$\begin{bmatrix} C(s) & S(s) \\ C'(s) & S'(s) \end{bmatrix} = \begin{bmatrix} \sqrt{\frac{\beta}{\beta_0}}\left(\cos\phi + \alpha_0\sin\phi\right) & \sqrt{\beta\beta_0}\sin\phi \\ \frac{(\alpha-\alpha_0)\cos\phi - (1+\alpha\alpha_0)\sin\phi}{\sqrt{\beta\beta_0}} & \sqrt{\frac{\beta_0}{\beta}}\left(\cos\phi - \alpha\sin\phi\right) \end{bmatrix}. \tag{6.72}$$

6.5 The complex formulation

It has been known since many years that the phase space ellipse that is normally used to model the phase space extension of a beam in linear dynamics may be represented by a complex number. This complex number has several interesting properties and it has normally been emphasized its similarity to a complex impedance in electrical circuits. Actually the method was created by Hereward in order to use electrical circuit methods for the design of beam transport lines. Although mentioned in many places, this method has never been very popular in comparison with transport matrices or Twiss parameters. To our knowledge, this method has never been fully developed, and only the transport transformation of several circuit has been presented. In this paper, I complete the formalism by obtaining a general differential equation and solving it to show that the general transformation is a Moebius one. The Moebius transformation is then analyzed and several properties presented. Some properties of the Moebius transformation are used to obtain known results of the beam transport theory in a completely different way. In addition, the result that beam transport is a conformal mapping of the Moebius type opens the possibility of studying the effect of the beam line on a domain of the complex plane and not only on a single point. Although the complex formalism may be obtained without using the Twiss parameters, we will refer to them because it may be easier for the reader used to them.

When the beam is transported through a drift space, the point of maximum divergence will keep its divergence $\gamma_2 = \gamma_1 = \gamma$, while its position will shift according to x' and the drift length L. This may be stated as,

$$-\alpha_2\sqrt{\frac{\epsilon}{\gamma}} = -\alpha_1\sqrt{\frac{\epsilon}{\gamma}} + L\sqrt{\epsilon\gamma} \tag{6.73}$$

So, through a drift space,

$$\frac{1}{\gamma_2} = \frac{1}{\gamma_1} \tag{6.74}$$

$$-\frac{\alpha_2}{\gamma_2} = -\frac{\alpha_1}{\gamma_1} + L \tag{6.75}$$

We can show in the same way that through a thin lens of focal length f, the following relationships will follow,

$$\frac{1}{\beta_2} = \frac{1}{\beta_1} \tag{6.76}$$

$$-\frac{\alpha_2}{\beta_1} = -\frac{\alpha_1}{\beta_1} - \frac{1}{f} \tag{6.77}$$

We can create two complex numbers as,

$$Z = \frac{1}{\gamma} - j\frac{\alpha}{\gamma} \tag{6.78}$$

$$Y = \frac{1}{\beta} + j\frac{\alpha}{\beta} \tag{6.79}$$

It may be seen by direct multiplication that $ZY = 1$ In addition, through a drift space we will have, $Z_2 = Z_1 + jL$, and through a thin lens $Y_2 = Y_1 + j/f$.

If we use the Y parameter, the size of the beam will be proportional to $\sqrt{\epsilon/\mathrm{Real}Y}$, while the lines passing through the origin are of constant α. The upper part of the complex plane corresponds to converging beams and the lower to diverging ones.

Fig. 6.4, shows a qualitative representation of the shape of the phase space ellipses according to their position in the Y plane.

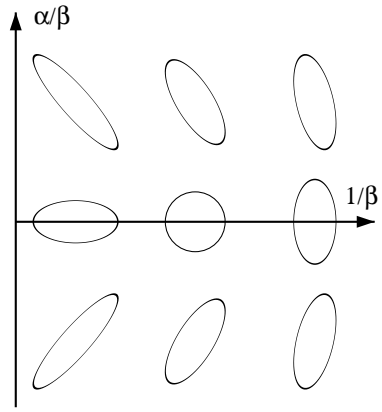

Figure 6.4 – Shape of the phase space ellipses according to their location in the Y plane. Each ellipse is drawn in a local x-x' system.

6.5.1 The general differential equation of the complex form

All the previous material has been studied in the past, starting with the report of Hereward, [32], and is cited extensively, [46], [35]; but as long as it is known to the author, the general differential equation governing the complex representation of the phase space ellipse has not been obtained. In order to obtain this equation, we analyze an infinitesimal displacement through a lens of strength per unit length k. Because the displacement is infinitesimal we can superpose the effect of the lens, which is straightforward in Y, with the effect of the drift ds, which is straightforward in Z. This superposition may be expressed in terms of Z or Y, but we prefer the later, because its real part is related to β, which in turn is related to the beam size.

$$dY = dY_{lens} + dY_{drift} = jkds + d\left(\frac{1}{Z}\right)_{drift} = \\ jkds + \frac{-dZ_{drift}}{Z^2} = jkds - Y^2 jds = \left(k - Y^2\right) jds \quad (6.80)$$

Finally, we obtain the following Riccati differential equation,

$$\frac{dY}{ds} = j\left(k - Y^2\right) \quad (6.81)$$

To solve the Riccati equation, we start by applying a substitution,

$$Y = -j\frac{u'}{u} \quad (6.82)$$

which converts the Riccati equation in a second order linear differential equation,

$$u'' + k(s)u = 0 \quad (6.83)$$

This is the generalized oscillator equation that governs the one particle problem. The solutions to eq. 6.83 may be expressed as a linear combination of the fundamental functions $C(s)$ and $S(S)$, which satisfy $C(0) = 1$, $C'(0) = 0$, $S(1) = 0$, $S'(0) = 1$. We have found then 2 particular solutions to the eq. 6.81, which may be written as:

$$Y_1 = -j\frac{C'}{C} \quad (6.84)$$

$$Y_2 = -j\frac{S'}{S} \quad (6.85)$$

With one particular solution, for instance the one based on C, we can reduce the Riccati equation to a first order linear equation,

$$Y = Y_1 + \frac{1}{z} \quad (6.86)$$

and we obtain,

$$z' - 2\frac{C'}{C}z = j \tag{6.87}$$

Because we know a second particular solution of the Riccati equation, we know, as well, a particular solution of eq. 6.87,

$$z_1 = \frac{1}{Y_2 - Y_1} = jCS \tag{6.88}$$

, where we have used that $CS' - C'S = 1$ because of the constancy of the Wronskian of eq. 6.83

With this particular solution of eq. 6.87, we may obtain its general solution as the sum of the general solution of the homogeneous equation and the particular solution

$$z = AC^2 + jCS \tag{6.89}$$

, where A is an integration constant. Replacing eq. 6.89 in eq. 6.86, we obtain the general solution of the Riccati equation,

$$Y = -j\frac{C'}{C} + \frac{1}{AC^2 + jCS} \tag{6.90}$$

We can obtain the integration constant by imposing $Y(0) = Y_0$, to obtain $A = Y_0^{-1}$. After some algebra, we obtain the final result:

$$Y = \frac{S'Y_0 - jC'}{jSY_0 + C} \tag{6.91}$$

, and therefore we conclude that the transformation of the complex parameter is a Moebius transformation of the shape given by eq. 6.91. A similar expression is found in [32], but the proof is restricted to drift spaces and lenses.

This result is very important, because the Moebius transformations are a group, i.e. the composition of Moebius transformations is new transformation. Because, any general transformation following the eq. 6.81 may be expressed as a composition of individual transformations, we may conclude that at any point in a transfer line there will be Moebius transformation representing the position of the line.

6.5.2 Phase advance in the complex formulation

Phase advance may be expressed in the complex formulation in an elegant way, which may be as well visualized graphically. First of all, lets start with the standard expression of phase advance,

$$\Delta\phi = \int \frac{ds}{\beta} \tag{6.92}$$

We can replace the integration between two points of the transport line by integration along β by using, $ds = \frac{ds}{d\beta}d\beta$, in which case, we obtain,

$$\Delta\phi = \int \frac{ds}{\beta} = \int \frac{1}{\beta}\frac{d\beta}{\frac{d\beta}{ds}} = -\int \frac{d\beta}{2\alpha\beta} \tag{6.93}$$

Finally, we express the phase advance in terms of the real and imaginary part of Y as,

$$\Delta\phi = \int \frac{\beta}{2\alpha} d\left(\frac{1}{\beta}\right) = \frac{1}{2}\int \frac{d\left(\frac{1}{\beta}\right)}{\frac{\alpha}{\beta}} \tag{6.94}$$

So that the phase advance may be expressed as the area between the *inverse* of the curve defining the movement of the beam in the complex plane and the abscissa axis. For periodical transport lines, the area will correspond to the one inside the closed region created by the inverse of the closed loop in the complex plane. It is interesting to note that because all periodical transport lines will have at least two points with α equal to zero, the inverse loop will have at least two vertical asymptotes. Nevertheless, the total area must remain bounded.

6.5.3 Some special transformations

With the general result of eq. 6.91 and the values of the transport matrices from standard textbooks, we can now build the Moebius transformations associated to several beam line elements.

A drift space

$$Y_2 = \frac{Y_1}{jLY_1 + 1} \tag{6.95}$$

The effect on the complex plane of the drift space in $Z = Y^{-1}$ is a vertical displacement in the upward direction. The complex inverse of a straight line in the complex plane is a circle passing through the origin. Therefore the trajectory in the Y plane will be a sector of a circle passing through the origin and tangent to the imaginary axis, the particle will move clockwise, because the inversion implies a change of sign with respect to the movement as seen from the origin. Fig. 6.5, shows the effect of a drift on the Z plane and the Y one.

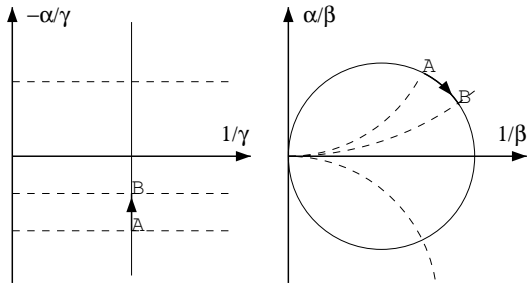

Figure 6.5 – Effect of a drift on the Z and the Y plane

We may see, as well, that the distance of the drift is measured as the difference in the vertical distance of the two extreme points defining the drift, A and B. We could imagine that all the horizontal lines of the Z plane are labeled by their constant pure imaginary coordinate $-\alpha/\gamma$. These lines are transferred to the Y plane as circles passing through the origin and tangent to the real plane. Each of these circles correspond to a certain $-\alpha/\gamma$.

A thin lens

$$Y_2 = Y_1 + \frac{j}{f} \tag{6.96}$$

This represents a vertical displacement upward when the lens is focusing and downward when it is defocusing.

A Thick lens

$$Y_2 = \frac{\cos(\sqrt{k}l)Y_1 + j\sqrt{k}\sin(\sqrt{k}l)}{j\sin(\sqrt{k}l)/\sqrt{k}Y_1 + \cos(\sqrt{k}l)} \tag{6.97}$$

A similar equation is given in [2] without proof.

This transformation is as well a circle centered in the real axis. It may be seen by dividing the numerator and denominator of eq. 6.97 by $\cos\sqrt{k}l$ and considering,

$$Y_2 = \frac{Y_1 + j\sqrt{k}\tan(\sqrt{k}l)}{j\tan(\sqrt{k}l)/\sqrt{k}Y_1 + 1} = \frac{Y_1 + j\sqrt{k}u}{ju/\sqrt{k}Y_1 + 1} \tag{6.98}$$

, as a Moebius transform of u=tan($\sqrt{k}l$), ie. the real axis. As it is known, Moebius transformations convert lines to circles (or lines in some cases). In order to obtain the parameters of the circle, we will write the Riccati equation expressed in terms of its real and imaginary components, $Y = x + jy$.

$$\frac{dx}{ds} = -2xy \tag{6.99}$$

$$\frac{dy}{ds} = k - \left(x^2 - y^2\right) \tag{6.100}$$

We may see, that when we change the sign of y, only the horizontal derivative changes sign, which is what we would expect from a circle centered on the real axis. Therefore, the circle must follow the equation,

$$(x - x_c)^2 + y^2 = R^2 \tag{6.101}$$

To obtain the parameters of the circle, we apply that when the vertical derivative eq. 6.100 cancels, we are on maximum of y, the point with (x_c, R) coordinates. We have then the following pair of equations defining the circle passing through the point (x_0, y_0) and with a focusing strength of k,

$$(x_0 - x_c)^2 + y_0^2 = R^2 \tag{6.102}$$

$$k - x_c^2 + R^2 = 0 \tag{6.103}$$

And the desired parameters will be,

$$x_c = \frac{k + x_0^2 + y_0^2}{2x_0} \tag{6.104}$$

$$R = \sqrt{x_c^2 - k} \tag{6.105}$$

We can see, that when $k > 0$, the circle is fully contained in the right part of the complex plane, having a bounded value of the complex parameter; while when $k < 0$, the circle is partly contained on the left part of the complex plane.

6.5.4 Some properties of the Moebius transformation

The Moebius transformation has been extensively studied [42] and there are many results that may be used in our analysis of transfer lines.

The matrix representation of the Moebius transformation

A general Moebius transformation,

$$w = \frac{az + b}{cz + d} \qquad \text{with } ad - bc \neq 0 \tag{6.106}$$

may be represented by a matrix

$$\mathfrak{H} = \begin{bmatrix} a & b \\ c & d \end{bmatrix} \tag{6.107}$$

and the composition of Moebius transformations corresponds to the matrix multiplication. This correspondence may be clearly seen if the complex numbers are written in homogeneous coordinates, $z = z_1/z_2$.

$$\frac{\omega_1}{\omega_2} = \frac{a\frac{z_1}{z_2} + b}{c\frac{z_1}{z_2} + d} = \frac{az_1 + bz_2}{cz_1 + dz_2} \tag{6.108}$$

We can express the Moebius transform in homogeneous coordinates as,

$$\begin{bmatrix} \omega_1 \\ \omega_2 \end{bmatrix} \begin{bmatrix} a & b \\ c & d \end{bmatrix} \begin{bmatrix} z_1 \\ z_2 \end{bmatrix} \tag{6.109}$$

We will represent the column vector of homogeneous coordinates with an underline, and the matrices of Moebius transformations (and later of circles) in Gothic characters. The Moebius transformation, will then be expressed as,

$$\underline{\omega} = \mathfrak{H}\underline{z} \tag{6.110}$$

In our case, the matrix $\mathfrak{H}$ will be given by the more restricted form,

$$\mathfrak{H} = \begin{bmatrix} S' & -jC' \\ jS & C \end{bmatrix} \tag{6.111}$$

, which has a certain resemblance to the transport matrix for a single particle, but remember that in the present case, we are dealing with a complex number representing the whole phase space ellipse of the beam. As $|\mathfrak{H}| = 1$, the Moebius transformation is normalized. We will often use the inverse matrix, which may be expressed as,

$$\mathfrak{W} = \mathfrak{H}^{-1} = \begin{bmatrix} C & -jC' \\ -jS & S' \end{bmatrix} \tag{6.112}$$

The fixed points and circles of the transformation

The fixed points are these left invariant by the transformation. We can obtain these points by using,

$$Y_{\pm} = \frac{j(C - S') \pm \sqrt{4 - (C + S')^2}}{2S} \tag{6.113}$$

There are three possibilities, if $|C + S'| < 2$, eq. 6.113 will have two complex solutions symmetrical with respect to the imaginary axis,if $|C + S'| = 2$, there will be only one double solution in the imaginary axis and if if $|C + S'| > 2$, there will be two solutions contained in the imaginary axis.

The circle preserving properties

One interesting possibility that opens when considering a beam line transformation as a complex plane transformation, is that entire regions of the complex plane may be transformed as conformal mappings. For instance, one of the properties of the Moebius transform is that circles are transformed to circles. It is possible then to find a set of initial conditions, envelope them with a circle and transform the circle along the beam line. All the initial conditions will remain inside the transformed circle. Because it is possible to analyze the evolution of the radius of the circle along the transformed planes, it is possible for instance to know if the solutions converge or not and at which speed.

We will proceed as in [47], in order to prove the circle preserving property, we will learn how to express the equation of the circle in the complex plane in the more general way. A circle of radius ρ and center at γ, may be expressed as,

$$|z - \gamma| = \rho \tag{6.114}$$

, or,

$$(z - \gamma)\,\overline{(z - \gamma)} = \rho^2 \tag{6.115}$$

$$z\overline{z} - z\overline{\gamma} - \overline{z}\gamma + \left(\gamma\overline{\gamma} - \rho^2\right) = 0 \tag{6.116}$$

We multiply eq. 6.116 by an arbitrary factor A, and write it in matrix form,

$$\begin{bmatrix} \overline{z} & 1 \end{bmatrix} \begin{bmatrix} A & -A\overline{\gamma} \\ -A\gamma & A\left(\gamma\overline{\gamma} - \rho^2\right) \end{bmatrix} \begin{bmatrix} z \\ 1 \end{bmatrix} = \begin{bmatrix} \overline{z} & 1 \end{bmatrix} \begin{bmatrix} A & B \\ C & D \end{bmatrix} \begin{bmatrix} z \\ 1 \end{bmatrix} = 0 \tag{6.117}$$

The circle will be represented by the Hermitian matrix $\mathfrak{C}$. It is possible to represent z by its column vector of homogeneous coordinates, $\underline{z}$. The circle will then be represented by the expression,

$$\underline{z}^H \mathfrak{C} \underline{z} = 0 \tag{6.118}$$

The superindex H will represent the conjugate of the transpose of a matrix. We may see by construction that $\mathfrak{C}$ must be Hermitian, as the diagonal elements are real and the non-diagonal elements are conjugate of each other. The arbitrary factor A has been introduced in order to include the straight lines as a particular case of the circles. In the projective plane, a line may be considered as a circle with a point at infinite. With the representation of eq. 6.118, all circles and lines of the complex plane may be represented as the quadratic form of a Hermitian matrix with respect to the homogeneous coordinates of the complex plane.

The determinant of the circle matrix $\mathfrak{C}$ is equal to $-A\rho^2$, and it is called the discriminant of the circle. Real circles will have a negative discriminant. The discriminant will be zero if $\mathfrak{C}$ represents a line or a zero radius circle. A positive discriminant is due to a circle of imaginary radius, which cannot be represented in the ordinary complex plane.

In order to check how the Moebius transform changes a given circle at the origin plane of the transformation, we will suppose that it is defined at the start of the transformation by,

$$\underline{z}^H \mathfrak{C}_1 \underline{z} = 0 \tag{6.119}$$

If $\mathfrak{W}$ is the reversed transformation, i.e. the one causing,

$$\underline{z} = \mathfrak{W} \underline{\omega} \tag{6.120}$$

then the circle will be transformed in the target plane to,

$$\underline{\omega}^H \mathfrak{W}^H \mathfrak{C}_1 \mathfrak{W} \underline{\omega} = 0 \tag{6.121}$$

The matrix inside the quadratic form of eq. 6.121 is Hermitian as well, and will represent a new circle in the transformed plane.

$$\mathfrak{C}_2 = \mathfrak{W}^H \mathfrak{C}_1 \mathfrak{W} \tag{6.122}$$

6.5.5 The complex parameters on a circular accelerator

In a circular accelerator, or in general a periodical line, we expect the beam to repeat its configuration in phase space. This is equivalent to operate in one of the fixed points of the Moebius transformation of eq. 6.91. Because we need a real part for the fixed point, we reproduce the classical result of the need to have $|C + S'| < 2$ in order to have a periodical solution for a periodical lattice.

This result can be expressed in the language of Moebius transforms via the classification of the transformation through the parameter σ. This parameter is invariant through any equivalence transformation, and is obtained as,

$$\sigma = \frac{(a+d)^2}{ad-bc} - 4 \tag{6.123}$$

, which is the quotient of the square of the trace by the determinant minus four. This definition of the transformation invariant is made so as to have a value of zero for the identity transformation. With regards to this parameter, all Moebius transformations may be classified as,

$$\begin{cases} \text{Elliptic if } -4 \leq \sigma < 0 \\ \text{Proper hyperbolic if } \sigma > 0 \\ \text{Improper hyperbolic if } \sigma \leq -4 \\ \text{Loxodromic if } \sigma \text{ is no real} \end{cases} \tag{6.124}$$

The behavior of an iterative application of the same Moebius transform with respect to the fixed points is fully described by the transformation type. The most important aspect for our study of the transversal dynamics is that only for the elliptic transformation does no of the invariant point not represent an attractor. That is, for all other transformation types, the iterative application of the transformation has as a limit one of invariant points. In addition, the invariant points for the case $|C + S'|$ lie on the imaginary axis and therefore $\beta \to \infty$, which shows that the beam will grow without limit in size for the hyperbolic case.

This condition will ensure as well that the Moebius transformation is of the elliptical type.

We can as well, use the result of the fixed point to obtain the Twiss parameters as a function of the fundamental solutions,

$$\beta = \frac{1}{\mathrm{Re}Y_+} = \frac{2S}{\sqrt{4-(C+S')^2}} \tag{6.125}$$

$$\alpha = \frac{\mathrm{Im}Y_+}{\mathrm{Re}Y_+} = \frac{C-S'}{\sqrt{4-(C+S')^2}} \tag{6.126}$$

This is, of course, a classical result of the theory of the Twiss parameters. We will use now the theory of the complex transform to obtain the structure of the solutions of the transport of the beam on a periodic line, which are not easily obtained from the classical theory, and that will show a beautiful structure when seen under the light of the Moebius transform.

We will start by asking if there are not only points, but also circles which are invariant under the Moebius transform, the answer is positive. First, we will prove that if there are two invariant circles, we can obtain a one-dimensional set of circles having this property. A pencil of circles is formed by the linear combination of two circles.

$$\mathfrak{C}(\lambda_1, \lambda_2) = \lambda_1 \mathfrak{C}_1 + \lambda_2 \mathfrak{C}_2 \tag{6.127}$$

It can be easily proved that if $\mathfrak{C}_1$ and $\mathfrak{C}_2$ are invariant circles, all the circles of their pencil are invariant. The pencil is one-dimensional, because eq. 6.127 may be multiplied by a constant without modifying the circle of the pencil.

As the basis of the pencil of invariant circles, we can use the zero radius circles with center in

the fixed points of the transformation. We will call the two fixed points Y_+ andY_-, according to the sign of the real part of the fixed points given by eq. 6.113. Their respective Hermitian matrices are,

$$\mathfrak{C}_\pm = \begin{bmatrix} 1 & -\overline{Y_\pm} \\ -Y_\pm & Y_\pm\overline{Y_\pm} \end{bmatrix} \tag{6.128}$$

The parametrization of the invariant circles will be,

$$\mathfrak{C}_\lambda = (1+\lambda)\,\mathfrak{C}_+ - \lambda\mathfrak{C}_+ \tag{6.129}$$

This parametrization ensures that the A term is one, so that the circle is normalized and that λ equal zero corresponds to the invariant point with positive real part. It is now possible to obtain the invariant circle of the invariant pencil that passes through any point, y_0 by solving λ from the equation,

$$\underline{y_0}^H \mathfrak{C}_\lambda \underline{y_0} = 0 \tag{6.130}$$

The solution of the invariant circle passing through point y_0 will be,

$$\mathfrak{C}_\lambda = \frac{-\underline{y_0}^H \mathfrak{C}_- \underline{y_0}}{\underline{y_0}^H \mathfrak{C}_+ \underline{y_0} - \underline{y_0}^H \mathfrak{C}_- \underline{y_0}} \mathfrak{C}_+ + \frac{\underline{y_0}^H \mathfrak{C}_+ \underline{y_0}}{\underline{y_0}^H \mathfrak{C}_+ \underline{y_0} - \underline{y_0}^H \mathfrak{C}_- \underline{y_0}} \mathfrak{C}_- \tag{6.131}$$

As an example of the use of the theory of invariant circles on a periodic transport line, let us analyze the structure of the solutions of the beam when injected not necessarily well matched on a FODO line. In a qualitative way, we can show the evolution of the beam along the line for a well matched condition in Fig. 6.6, which shows the trajectory in the Y plane of a beam in a symmetrical FODO cell. The focusing thin lens is the line CD, the upper circle arc, DA is the drift going to the defocusing lens, AB is the defocusing lens and BC the drift space going to the focusing lens.

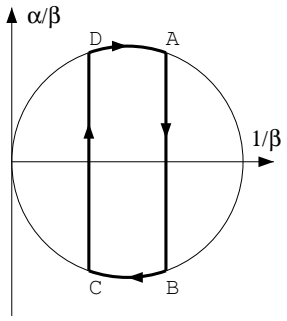

Figure 6.6 – Trajectory on the Y plane of a beam through a FODO cell

To use a more quantitative approach, we will define a thick lens FODO cell which quadrupoles of 0.2 m length and drift spaces of 2 m length. The strength of the quadrupoles is ± 4 m^{-2}. Quite arbitrarily, we will analyze the behavior of the horizontal solution at 1/3 of the length of the focusing quadrupole. The cell, with the horizontal Twiss parameters for the injection matched at the invariant point may be seen in fig. 6.7.

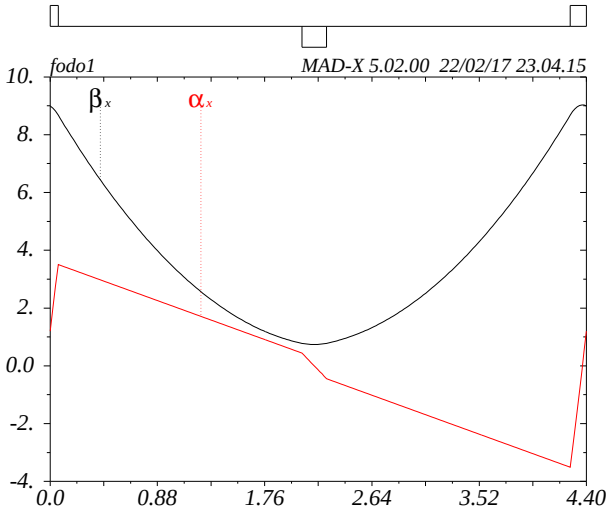

Figure 6.7 – Horizontal Twiss parameters in the example cell

The same cell may be described by the movement of the beam point in the complex plane. This is shown in fig. 6.8. The matching parameters at the injection point are β 9 m and α roughly 1.1, or the corresponding complex parameter.

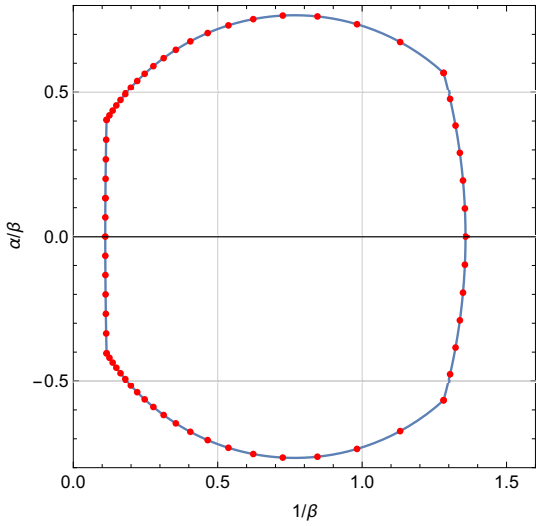

Figure 6.8 – The same cell described in the complex plane

In case that the injection parameters are not well matched, the beam will oscillate around the periodic parameters in a way in which is difficult to find any apparent order, for instance, at fig. 6.9 the beam has been injected with a β of 5 m and α equal to 0.5. In this condition, the beam wiggles around the ideal fixed point.

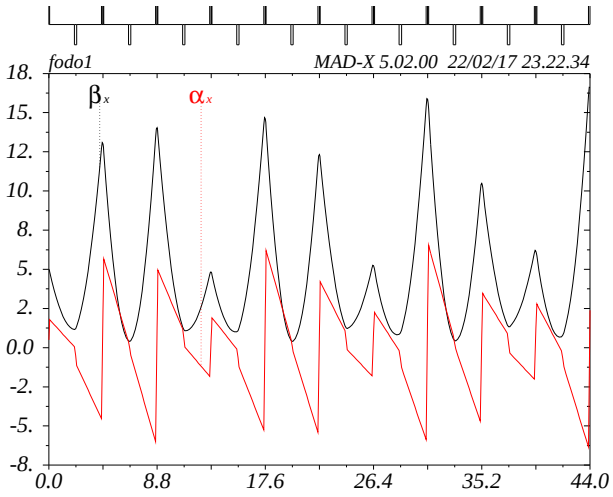

Figure 6.9 – Horizontal Twiss parameters in the example cell for the case of a non-matched injection.

The situation is more clear, when the different complex points are plotted in the complex plane after each period. This situation is shown in fig. 6.10. The points must remain in the circle of the invariant pencil of circles that passes through the point defined by the injection parameters. At some passages, the point will be at the right side of the fixed point, corresponding to a smaller beam and at other passages, the point will be at the left, which corresponds to a larger beam. Nevertheless, the beam size will be bounded by the left-most side of the invariant circle, which is easily obtained by the parameters of the $\mathfrak{C}_\lambda$ invariant circle of eq. 6.131.

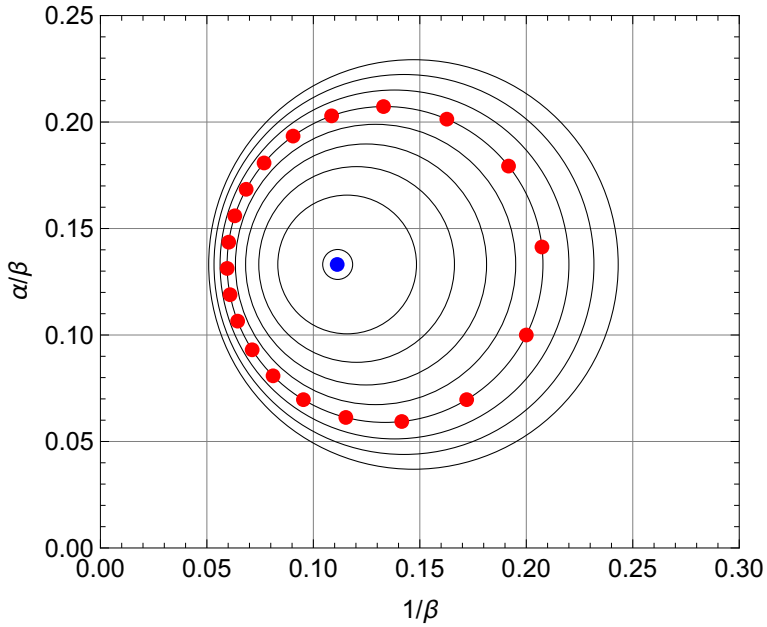

Figure 6.10 – The pencil of invariant circles at 1/3 o of the length of the quadrupole. We have shown the position of the passes of the beam during several periods and the fixed point

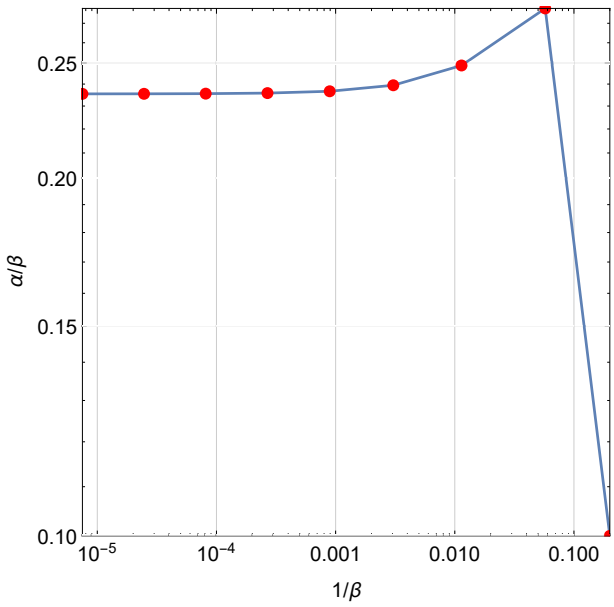

Figure 6.11 – The same FODO cell but with unstable parameters. We can see that the movement of the beam converges to one of the stable points located at the imaginary axis. Note the logarithmic scale that is required to show all points as the convergence towards the fixed point is exponential.

For the sake of comparison, we have increased the strength of the quadrupoles until the Moebius transform has become hyperbolic. In this case, the behavior of the movement of the particles have changed dramatically, and instead of showing a rotation around one of the fixed points, now it converges to one of the fixed points, which actually is located at the imaginary axis and therefore it represents a beam of infinite size, $\beta \to \infty$. This situation is shown in 6.11.

6.6 The effect of an accelerating gap on the transverse dynamics

In this section, we will see the relationship between the longitudinal dynamics, that we studied in the previous chapter and the transversal dynamics that we are analyzing in the present one. We will divide the analysis in two sections, in this one we will see how the need to accelerate the beam requires a certain defocusing in the transversal plane, and in the next section we will see how this defocusing affects the stability in the transversal plane. With the knowledge of both effects, we can obtain the requirements of transversal focusing to successfully accelerate the beam to the desired energy.

An accelerating gap has a certain impact as well in the transverse dynamics. The main reason may be seen in fig. 6.12, in which we can see that away from the central axis of the accelerating gap, the electric field has a radial component as well as an axial one. This field is focusing at the beginning of the gap and defocusing at the end. The overall effect of the gap on the transverse movement of the particles depends on how these two parts of the radial electrical field balance each other. There are two competing effects on this balance,

1. The electrical field is changing during the transit of the particle through the gap. As

typically linacs operate in the accelerating mode, with negative synchronous phase, ϕ_s, the field is increasing during the transit. Therefore, the net effect of the gap is defocusing, as the particles will see a larger radial electrical field pointing outwards near the end of the gap.

2. If the field is accelerating the particles will increase their energy during the transit, and will arrive with a higher electrical rigidity to the second half of the gap. This effect will then be focusing on average. Nevertheless, this effect is only important when a significant increase in the electrical rigidity of the particle may be obtained in a single gap, typically in electron linacs

In this work, we will only study the first effect, which is in most cases the dominant one.

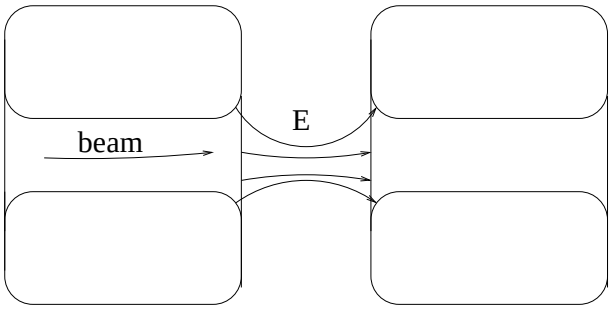

Figure 6.12 – Shape of the electric field lines in the gap

The radial electrical field is related to the axial one due to the the zero divergence of the field. In cylindrical coordinates, the divergence may be expressed as,

$$\frac{1}{r}\frac{\partial}{\partial r}\left(rE_r\right) + \frac{\partial E_z}{\partial z} = 0 \tag{6.132}$$

In addition, the on-axis electrical field does not change on first order with the radius, as it may be immediately derived from the Faraday equation. From the divergence equation, the radial field near the axis may be related to the variation of the axial one as,

$$E_r = -\frac{r}{2}\frac{\partial E_z}{\partial z} \tag{6.133}$$

This equation says to us that the radial field will be outwards on one side of the gap and inwards on the other side (of course, the absolute direction changes with the phase). The situation may be seen in fig. 6.13.

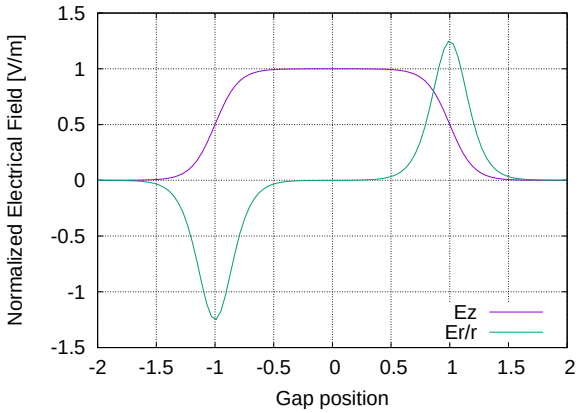

Figure 6.13 – Radial and axial electrical field on an idealized gap

The expression including the dependence with time will be,

$$E_r = -\frac{r}{2}E'(z)\cos(\omega t + \phi) \tag{6.134}$$

In addition, there will be an azimuthal magnetic field created by the changing electrical field. From Ampere's law including the displacement current, we can state,

$$B_\theta 2\pi r = \frac{1}{c^2}\frac{d}{dt}\left(E_z \pi r^2\right) \tag{6.135}$$

The magnetic field will be,

$$B_\theta = \frac{r\omega}{2c^2}E(z)\sin(\omega t + \phi) \tag{6.136}$$

The change in radial momentum may be calculated by the Lorentz force equation,

$$\frac{dp_r}{dt} = e\left(E_r - \beta c B_\theta\right) \tag{6.137}$$

Which may be expressed as an integral along the gap changing the variable of integration taking into account that in the paraxial approximation, $z = \beta ct$.

$$\Delta p_r = e\int_{-L/2}^{L/2}\left(\frac{E_r}{\beta c} - B_\theta\right)dz \tag{6.138}$$

We will calculate independently the effect of the electrical and magnetic field in order to understand the effect of each of them,

$$\Delta p_r^e = e\int E_r\,dt = \frac{e}{\beta c}\int E_r\,dz = -\frac{er}{2\beta c}\int_{-L/2}^{L/2}E'(z)\cos\left(\frac{\omega}{\beta c}z + \phi\right)dz \tag{6.139}$$

, where the integral extends to a region where the axial field vanishes. In this condition, the integral may be evaluated by parts as,

$$\Delta p_r^e = -E(z)\cos\left(\frac{\omega}{\beta c}z+\phi\right)\Big|_{-L/2}^{L/2} - \frac{er\omega}{2\beta^2c^2}\int_{-L/2}^{L/2} E_z \sin\left(\frac{\omega}{\beta c}z+\phi\right)\,dz \tag{6.140}$$

The first term will disappear due to the vanishing of the electrical field at both extremities of the gap. In the second term we can expand the sinus in its both term, and considering that the field in the gap is even, only the cosine term in z will remain,

$$\Delta p_r^e = -\frac{er\omega\sin\phi}{2\beta^2c^2}\int_{-L/2}^{L/2} E_z\cos\left(\frac{\omega}{\beta c}z\right)\,dz = -\frac{er\omega V_0 T\sin\phi}{2\beta^2c^2} \tag{6.141}$$

The effect of the magnetic field is easier to calculate, as no part integration is required,

$$\Delta p_r^m = -\int_{-L/2}^{L/2} eB_\theta\,dz = \frac{er\omega V_0 T\sin\phi}{2c^2} \tag{6.142}$$

Because the synchronous phase must be negative to provide stability, the electrical field will have a defocusing effect and the magnetic field a focusing one. Because the term in the electrical field is divided by β^2 it will be dominant at the low energy range. The magnetic field will start to cancel the electrical one only approaching the relativistic regime, $\beta \to 1$. The total effect will be,

$$\Delta p_r = \Delta p_r^e + \Delta p_r^m = -\frac{er\omega V_0 T\sin\phi}{2c^2}\left(\frac{1}{\beta^2}-1\right) = -\frac{er\omega V_0 T\sin\phi}{2c^2\beta^2\gamma^2} \tag{6.143}$$

The defocusing effect may be modeled as a kick dependent on the radial error of the particle, i.e. it may be modeled as a thin defocusing quadrupole,

$$\frac{\Delta r'}{r} = \frac{\Delta p_r}{p_z r} = \frac{\Delta p_r}{m\gamma\beta c r} = -\frac{e\omega V_0 T\sin\phi}{2mc^3\beta^3\gamma^3} \tag{6.144}$$

In the next section, we will use eq. 6.144 to obtain the defocusing effect of an accelerating gap and see under which circumstances may the acceleration be stable.

6.7 The Smith and Gluckstern stability chart

The Smith and Gluckstern stability chart plots in the abscissa the focusing strength of the accelerating gaps, related to the RF level for a certain linac, and the focusing elements strength in the ordinate. Then the plot is divided in regions of stability and instability, and the stable regions may be equipped with constant phase advance lines.

The unit cell of the transverse dynamics of an accelerating structure may be seen in fig. 6.14.

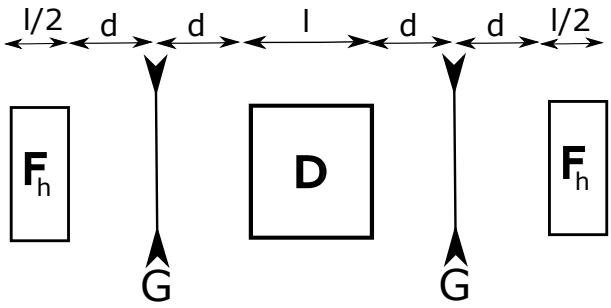

Figure 6.14 – Unit cell of an accelerating structure. The cell starts at the middle of a focusing quadrupole. G represent the gap as a thin lens, D is a defocusing quadrupole and F_h is half a focusing quadrupole.

For the X axis an adimensional parameter characterizing the defocusing strength of the gap is chosen, this gap is the ratio between the length of the cell, i.e. the distance between two points at which the phase if the RF repeats, this parameter is called Δ_0, and it is defined as,

$$\Delta_0 = \frac{\beta\lambda}{f_g} \tag{6.145}$$

Where the focal length may be obtained from eq. 6.144. In the Y axis it is represented the focusing strength of the quadrupoles, in addimensional form, the parameter is,

$$\theta_0 = K\beta\lambda = \sqrt{G/\eta_m}\beta\lambda \tag{6.146}$$

In addition, we define the quadrupole filling factor, Λ, defined as,

$$\Lambda = \frac{l}{l + 2d} \tag{6.147}$$

The transport matrix, from the center of a focusing quadrupole to the center of the nest one will be,

$$M = F_{1/2} \cdot d \cdot G \cdot d \cdot D \cdot d \cdot G \cdot d \cdot F_{1/2} \tag{6.148}$$

From this transport matrix, the periodical transport properties of the beam, stability, phase advanced, beam size and so on may be obtained, they are summarized in the Smith and Gluckstern stability plots, that may be seen in fig. 6.15.

The adimensional dimension of the beam may be expressed by a parameter $\gamma = \beta/l_{cell}$, curves of constant γ may be seen in fig. 6.15.

In addition to a simple FODO cell, it is possible to have a FOFODODO cell, in which there are two consecutive focusing and defocusing quadrupoles. This solution tends to allow the use of weaker quadrupoles, as may be seen in the reduced ordinates axis span of fig. 6.15, right; but it has a reduced stability margin and requires larger beam values and apertures.

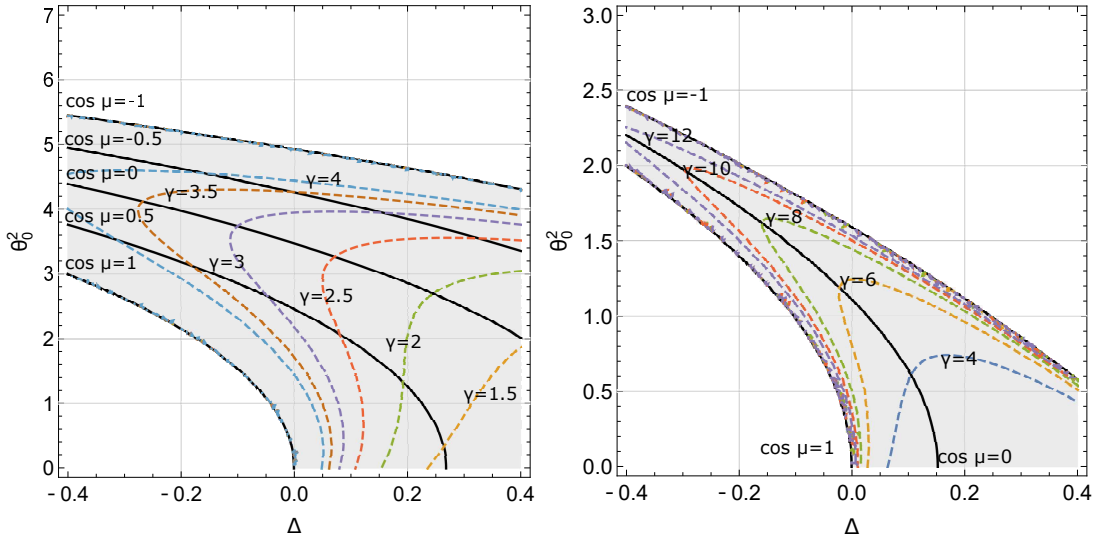

Figure 6.15 – Smith and Gluckstern stability charts for N=1 (left) and N=2 (right), for $\Lambda = 0.5$

We can see in the chart of fig. 6.15 that the acceleration decreases the region in which the beam is stable, this effect is specially marked in the case where the cell is FOFODODO. The maximum size of the beam increases, as well, with the acceleration. The minimum beam size is obtained near a phase advance of 90°, although this is an approximate relationship.

The main use of the Smith and Gluckstern chart is conceptual. In it we can observe the reduction of the stability zone with the increase of the acceleration in the gap, the existence of the optimal focusing power with respect to beam size, and many other properties of the focusing system in multi-gap accelerating structures. Nevertheless, its practical use must be complemented with a more detailed simulation tool, as some of its limitations, i.e. constant filling factor quadrupoles, no space charge, and others are very important in the actual behavior of the beam.

6.8 Types of transverse focusing

There are several ways in which the transverse focusing may be provided, we will center in two of them, solenoids and quadrupoles, which are widely used in linacs. Solenoid focusing has the advantage of being focusing at both planes at the same time, but it is normally much weaker, as it depends on an indirect effect. Quadrupole focusing applies direct force by the coupling of dominantly axial velocity and radial fields, but because of the nature of the magnetic field it must be focusing in one plane and defocusing in the transverse one, which force us to use combination of quadrupoles with alternating polarity to provide focusing on both planes.

Another way to provide focusing in both planes is provided by the weak focusing principle. We have seen that the first order equations have in the dispersive plane a focusing term of strength $1/\rho^2$. This focusing may be distributed in both planes by using a weak gradient that provides focusing in the non-dispersive plane, while does not reduce below zero the geometrical focusing in the dispersive one. This kind of focusing was dominant in the accelerators until the discovery that the alternating gradient focusing provided by quadrupoles allows for a significant reduction in the cost of the magnetic systems required for beam confinement.

6.8.1 Solenoid focusing

Solenoid focusing is widely used for focusing particle beams at the low energy range. The main advantage of this type of focusing is that both transverse axes are focused at the same time by only one magnetic element. We will see that the focusing capability of an asymmetric system scales as the inverse of the square of the magnetic rigidity, and hence the limitation of the use of solenoids for the focusing of low energy beams.

At the entrance of the solenoid there is a region where the radial magnetic field increases significantly with the radius of the incoming particle. This radial field creates a tangential component of the velocity that will couple with the axial field of the solenoid to provide the desired radial focusing. A very intuitive qualitative description of the focusing effect of solenoids may be seen in [37].

For obtaining the equation determining the focusing strength of a solenoidal lens, we start proving a very general and important result. We start with the Lagrangian formulation of the movement of a charged particle in a static magnetic field. The Lagrangian is [18],

$$\mathcal{L} = -mc^2\sqrt{1-(v/c)^2} + e\vec{v}\cdot\vec{A} = -mc^2\sqrt{1-\frac{\dot{r}^2+r^2\dot{\phi}^2+\dot{z}^2}{c^2}} + er\dot{\phi}A_\phi \tag{6.149}$$

Due to the symmetry of the problem, the azimuthal component of the vector potential may depend only on r and z, but not on ϕ. Therefore, ϕ is a cyclic variable, and its generalized momentum if conserved.

$$P_\phi = \frac{\partial\mathcal{L}}{\partial\dot{\phi}} = \gamma m r^2\dot{\phi} + erA_\phi = \text{constant} \tag{6.150}$$

This very remarkable result is called Busch theorem and it is the basic of the analysis of beam transport in axisymmetric problems. In most cases, we can assume that the azimuthal velocity outside of the lens is zero, so that the constant value in eq. 6.150 is zero. In this case, the azimuthal velocity at any point inside the lens will be,

$$v_\phi = -\frac{eA_\phi}{\gamma m} \tag{6.151}$$

If we now apply the Euler-Lagrange equation to the radial component of the Lagrangian, we obtain,

$$\gamma m\ddot{r} = \gamma m r\dot{\phi}^2 + e\dot{\phi}r\left(\frac{A_\phi}{r}+\frac{\partial A_\phi}{\partial r}\right) = \gamma m r\dot{\phi}^2 + e\dot{\phi}rB_z \tag{6.152}$$

The first term in the right term is the centrifugal force, and the second the Lorentz force. The value of the azimuthal speed, $\dot{\phi}$, may be obtained from the conservation of the azimuthal canonical moment and the radial equation may be expressed as,

$$\ddot{r} = \left(\frac{e}{\gamma m}\right)^2\left(\frac{A_\phi^2}{r} - A_\phi B_z\right) \tag{6.153}$$

We will now use the paraxial approximation to express the time derivatives as longitudinal derivatives,

$$\frac{d^2}{dt^2} = v^2\frac{d^2}{dz^2} \tag{6.154}$$

Because the field is purely magnetic, the modulus of the velocity is constant and can be extracted from the derivative.

With this simplifications, we obtain,

$$\frac{d^2r}{dz^2} = \left(\frac{e}{\gamma m v}\right)^2 \left(\frac{A_\phi^2}{r} - A_\phi B_z\right) = \frac{1}{\eta_m^2}\left(\frac{A_\phi^2}{r} - A_\phi B_z\right) \tag{6.155}$$

We can see that the dependence of the focusing capability of the magnetic system decreases with the square of the magnetic rigidity of the beam. We can further simplify eq. 6.155 supposing that the particles only have very small excursions away from the solenoid axis. In this case, the axial magnetic axis is constant, and the vector potential may be expressed as,

$$A_\phi = \frac{1}{2} r B_z\left(z, 0\right) \tag{6.156}$$

And the focusing equation may be expressed as a function of the axial magnetic field at the origin as

$$\frac{d^2r}{dz^2} + \left(\frac{B_z^2\left(z,0\right)}{4\eta_m^2}\right) r = 0 \tag{6.157}$$

Although we have mentioned several times that the main limitation of the solenoid focusing is the dependence of the strength on the square of the magnetic rigidity; it is interesting to note, that the effect of the magnetic field also increases with the square of the magnetic field. This implies that the use of superconducting magnets may be very advantageous, as the value of the axial field may be several times higher than when using normally conducting solenoids. Actually, many linacs use nowadays superconducting solenoids in combination with superconducting radiofrequency.

An interesting application of a periodic system of solenoid focusing for a muon cooling channel may be seen in [3].

6.8.2 Quadrupole focusing

In general terms, a form of focusing based on a field which is mostly transverse to the beam direction has the potential of being more performing. The reason is that the transverse forces responsible for the focusing are created by the interaction of the main component of the particle speed and the main component of the magnetic field.

The focusing will be created by a quadrupole, a magnet which creates a field whose modulus increase linearly with the distance from the ideal particle trajectory. The ideal field of the quadrupole corresponds to the second term of the Taylor expansion of the complex field in terms of the complex variable. In real terms, the 2D field of an ideal quadrupole may be expressed as,

$$B_x = gy \tag{6.158}$$

$$B_y = -gx \tag{6.159}$$

, where g is the gradient or the linear variation of the modulus of the field with the radius. An important consequence of the field equations is that the sign of the gradient with respect

to two perpendicular axes changes. This fact implies that the magnetic field of a quadrupole must be focusing in one direction and defocusing in the other.

Normal conducting quadrupoles could be used for the focusing of drift tube linac. In some circumstances, the possibility of adapting the magnetic field during the beam commissioning or the need to use the linac at several energies or with different particles requires the use of electromagnetic quadrupoles, that must be integrated inside the drift tubes. Fig. 6.16 shows the design of a quadrupole performed by the author for an old version of the drift tube linac of IFMIF. The design was based on an original work of Saclay for IFMIF, see for instance [33]. This design has a very interesting cooling of the coils based on flooding the inside of the drift tube with water that circulates through the stem in a coaxial circuit.

On the other hand, electromagnetic quadrupoles tend to be bulky and impose a constraint in the RF design of the linac unit, requiring a larger diameter of the drift tube and decreasing the performance of the whole linac. The PMQs have a significant advantage in size and simplicity, allowing a much reduced drift tube, which allows improving the RF design of the DTL.

It is interesting to note that the drift tubes aperture is typically small, as the distance between the drift tubes is short and the high spatial frequency of the focusing array causes the beam to remain small.

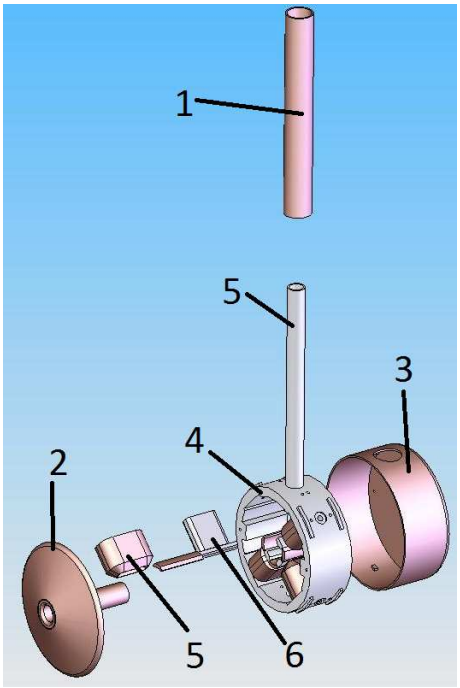

Figure 6.16 – Drift tube with an electromagnetic quadrupole integrated in it. (1) Drift tube stem, (2) and (3) Drift tube, (4) quadrupole yoke, (5) quadrupole coil, (6) detachable pole.

6.9 Design of a wide aperture spectrograph

A very interesting application of the transversal dynamics consist in the separation of particles of different magnetic rigidity by a magnetic field. As we have seen in the previous sections, the difference in magnetic rigidity causes the particles to follow a different trajectory from the source to a certain plane perpendicular to the trajectory where the amount of each type of particle is measured.

A typical spectrograph will create a set of different particles from a particle source with a definite aperture and divergence, the particles will be accelerated from the source to a transport line by an electrostatic or an RF field, will be separated by the spectrograph and will be collected in a detector to measure the amount of each type of particle. The main task of the spectrograph is to separate spatially the particles with different magnetic rigidity in spite of the finite aperture and divergence of source.

In most spectrographs, the requirement to separate particles with very similar magnetic rigidities implies that the beam that enters the spectrograph must have a small divergence and aperture to avoid the non-linear components of the magnetic field disturbing the trajectories and mixing particles of different magnetic rigidity. However, this increased resolution implies a reduction of the current entering the spectrograph, and if the desired particles are scarce, the amount of time required to collect a certain amount of the desired species may increase largely.

6.9.1 Principle of operation

As an example of an spectrograph that may circumvent the problem of the degradation of current with the increase of resolution , the author designed the dipole magnet described in [25], [4]. This spectrograph is installed in the CMAM (*Centro de microanálisis de materiales*) in the Universidad Autonoma at Madrid, and is used for high-resolution depth profiling of heavy elements using Rutherford scattering of light ions (RBS) and of light elements using elastic recoil detection (ERD). Typically the spectrographs used for this type of applications require collimating most of the secondary beam in order to obtain the desired resolution. In the novel design, the position of the incoming ions is measured prior to entering the spectrograph. This allows to increase the angle acceptance of the spectrograph to 14 msr, two order of magnitude larger than for most spectrographs.

In order to detect the time and position of the entering ion, it passes through a thin foil, 5 nm thick diamond-like, under an angle of 45

The time of flight technique is used to obtain the velocity of the particle, while the magnetic rigidity, mv/q for the non-relativistic ions, is obtained by the spectrograph. In such a way, it is possible to obtain the mass to charge ratio.

6.9.2 Design of the multipole magnet

The challenge of the design of the spectrograph magnet is to allow the transport of all particles entering in a large acceptance angle, $\pm 4.5°$ in the horizontal plane and $\pm 6°$ in the vertical plane of the spectrograph; into the one-dimensional silicon detector located on the image plane of the spectrograph. Because the angle of acceptance is so large, most of the ions

will travel through highly non-linear fields and the typical design equations of the focusing of dipoles are only a help to provide a starting point for the simulations of the dipole. In addition, all particles with an energy spread, $\Delta E/E$ of $\pm 2.5\%$ of the central energy must reach the detector.

The design of the spectrograph was based on building a finite element method of the magnet and using ray tracing to check that all particles entering the acceptance cone ended in the detector. The degrees of freedom implemented in the model were:

1. The bending angle

2. The entrance and exit angles of the dipole

3. The multipolar content of the field in the central zone up to 4th order

Some of these parameters are shown in fig. 6.17. The last set of parameters (the multipolar components of the central part) are explained in the next section.

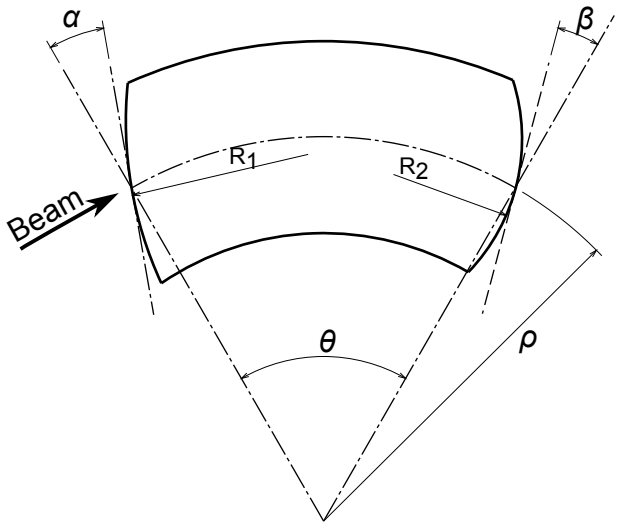

Figure 6.17 – Parameters defining the pole shape

6.9.3 Generation of a general multipolar field

We will describe the complex potential in sect. 7.3. The imaginary part of the complex potential is the scalar magnetic potential, which has the property that the magnetic induction is derived from it as $\vec{B} = -\nabla\Phi$. Therefore, the magnetic induction will be perpendicular to the lines of constant Φ. From the boundary conditions of the magnetic field $\vec{H}$, which has a tangential component that in absence of surface current, must be the same on both sides of a boundary; the field on the air boundary of a ferromagnetic must be perpendicular to the boundary. We conclude, then, that the surfaces of the ferromagnetic materials are of constant Φ.

We will see in eq. 7.26, an expression relating the field coefficients to the scalar potential. Therefore, the shape of the poles will be given by eq. 6.160.

$$\sum_{n=1}^{\infty} \frac{r^n}{nR^{n-1}} \left(B_n \sin n\theta + A_n \cos n\theta\right) = \text{Constant} \tag{6.160}$$

In order to know which is the constant, Ampere law must be used. The total magnetomotive force connecting to poles of an iron dominated magnet may be calculated as,

$$Ni = \int \vec{H} \cdot d\vec{r} = \int H_x dx + H_y dy = \text{Im} \frac{1}{\mu_0} \int \left(B_y + iB_x\right)\left(dx + idy\right) = -\text{Im}\Delta\Psi \tag{6.161}$$

So that the variation between the scalar potential of two poles of an iron dominated magnet is equal to the total magnetomotive force around these poles. With the theory developed in this section, it is possible to obtain the ideal shape that several practical magnets must have and in addition which is the required magnetomotive force to obtain a certain value of field.

In the next sections, we will show a few examples of different magnetic fields.

An ideal dipole

In an ideal dipole, the curves of constant scalar potential may be obtained from eq. 6.160,

$$\Phi = -\frac{B_1}{\mu_0} r \sin\theta = -\frac{B_1}{\mu_0} y \tag{6.162}$$

And from eq. 6.161, the required magnetomotive force will be,

$$Ni = \frac{B_1}{\mu_0}\left(y_2 - y_1\right) = \frac{B_1}{\mu_0} g \tag{6.163}$$

where g is the gap of the magnet.

An ideal quadrupole

In the same way, it is possible to obtain a pure quadrupole by shaping the poles according to the lines of constant scalar potential,

$$\Phi = -\frac{B_2 r^2}{2R} \sin 2\theta = -g\left(r\sin\theta\right)\left(r\cos\theta\right) = -gxy \tag{6.164}$$

Where we have used that the gradient, g is B_2 divided by the reference radius. The ideal pole shapes are equilateral hyperbolae with the horizontal and vertical axes as asymptotes. Because the typical vacuum chamber inside the quadrupole is circular, we are interested in knowing which is the hyperbola tangent to a circle of diameter d centered on the origin. This will happen at 45° for symmetry reasons. Therefore, the scalar potential at the pole tangent to the circle will be,

$$\Phi = -g\frac{d^2}{8\mu_0} = -Ni_{\text{per coil}} \tag{6.165}$$

The total magnetomotive between two poles will be twice this value, but as typically there is one identical coil around each pole, eq. 6.165 gives the magnetomotive force required for each of these 4 coils.

A combined function magnet

A combined function has at the same time a dipole component and a quadrupole component. The curves of constant scalar potential will be then,

$$B_1 y + \frac{B_2}{R} xy = By + gxy = B_1 y \left(1 + b_2 \frac{x}{R}\right) = K \tag{6.166}$$

For this type of magnet, is quite common to use the field index that is defined as,

$$n = -\frac{\partial B_y / \partial x}{B/\rho} \tag{6.167}$$

Where, ρ is the radius of curvature. In this case, the equation of the pole shape will be,

$$B_1 y \left(1 - n \frac{x}{\rho}\right) = K \tag{6.168}$$

6.9.4 Ray tracing

Although the first design was performed with the classical linear equations for transport lines, using the matrix formalism. The aperture and divergence of the incoming beam is so large that the final design was performed by a trial and error system using a parametric FEM model of the magnet and a ray tracing. A ray tracing program was created for this purpose. This program reads the field calculated by the finite element model and launches a set of particles covering the whole range in the aperture ellipse and the energy spread. The program integrates the dynamical equations associated with the Lorentz force and checks that no particle is lost in the vacuum chamber and which are the intersection points in the detector (image) plane. The 6 scalar Ordinary Differential Equations that are solved are,

$$\frac{d\vec{r}}{ds} = \vec{\tau} \tag{6.169}$$

$$\frac{d\vec{\tau}}{ds} = \frac{\vec{\tau} \times \vec{B}\left(\vec{r}\right)}{\eta_m}. \tag{6.170}$$

Which are expressed in vector for and clearly show that all particles of the same magnetic rigidity will trace the same path.

Because of the vertical symmetry, only the particles launched with positive vertical velocity has been simulated. The center of curvature of the magnet is centered on the origin, the object plane is located at 800 mm from the start of the magnet, and the detector (image plane) is located at 700 mm from the magnet exit. Fig. 6.18 is a top view of the simulated trajectories, in which it may be seen the initial drift from the object plane, the bend in the dipole and the image formation at the detector.

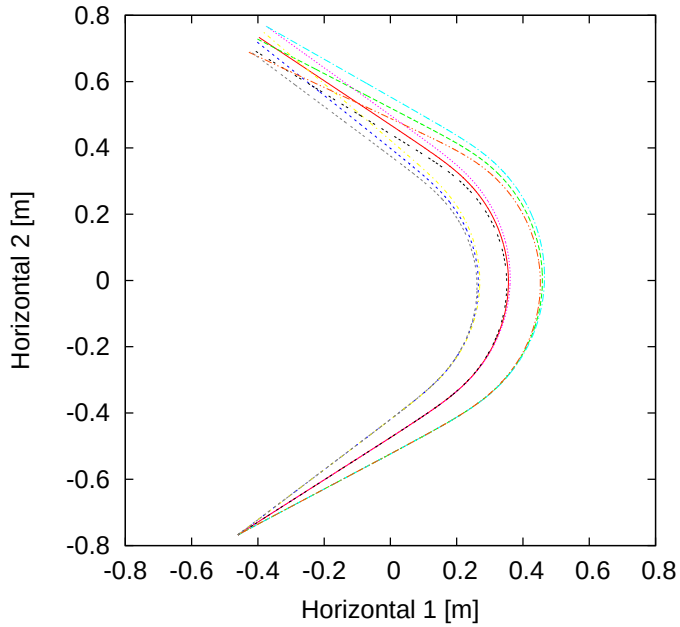

Figure 6.18 – Top view of the particle trajectories

A vertical view of the trajectories is shown in fig. 6.19. It is interesting to see the vertical focusing due to the pole face angles, which at the entrance produce a roughly horizontal beam and at the exit makes the particle converge towards the detector. This plot is useful to prove that a vertical mechanical aperture of 100 mm is enough for the magnet.

Fig. 6.20 shows the interception of the particles with the detector. There, it is shown that the objective of the design is reached, as all the particles fall in the active part of the detector, marked by a red frame.

6.9.5 Manufacturing of the magnet

Because of the complex shape of the pole, the magnet was machined using a CNC milling machine. The magnet is divided in a lower and an upper part, both parts are similar except that the lower one has interfaces for attaching the magnet supports, and the upper part has the interfaces for the alignment targets.

The pole and the columns were attached to the top and bottom plates and then the pole shape and the matting face of the columns were machined during the same operation. In such a way, it could be ensured that once the two halves were assembled, the relative position of the poles would match perfectly. Both magnet halves were connected using bolts and locating pins, so that they can be re-assembled in a repetitive way.

The coils were divided in several double pancakes, which were put electrically in series but hydraulically in parallel. The coils were insulated with glass fiber tape.

Fig. 6.21 shows the assembly of the lower part of the magnet and the final installation at the CMAM.

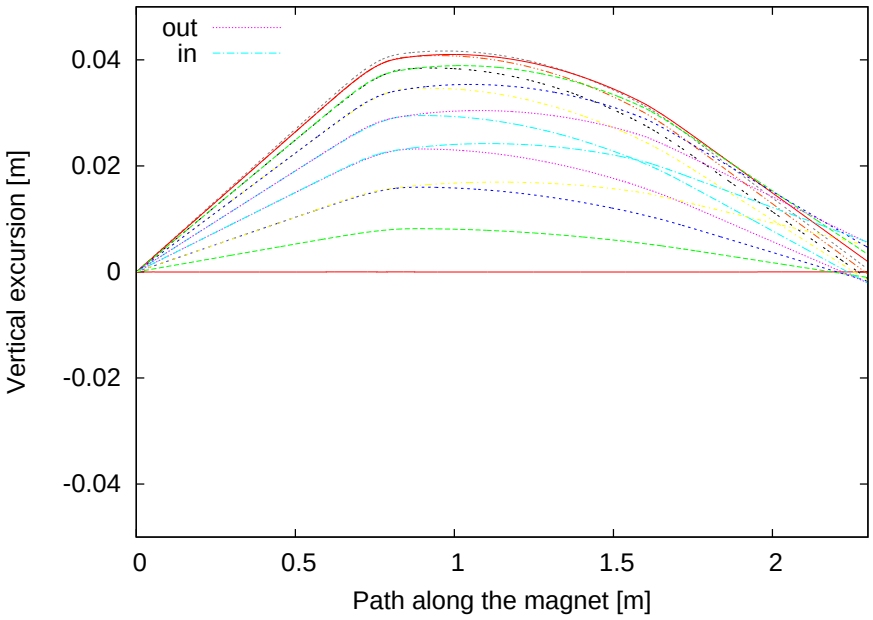

Figure 6.19 – Elevation view of the particle trajectories

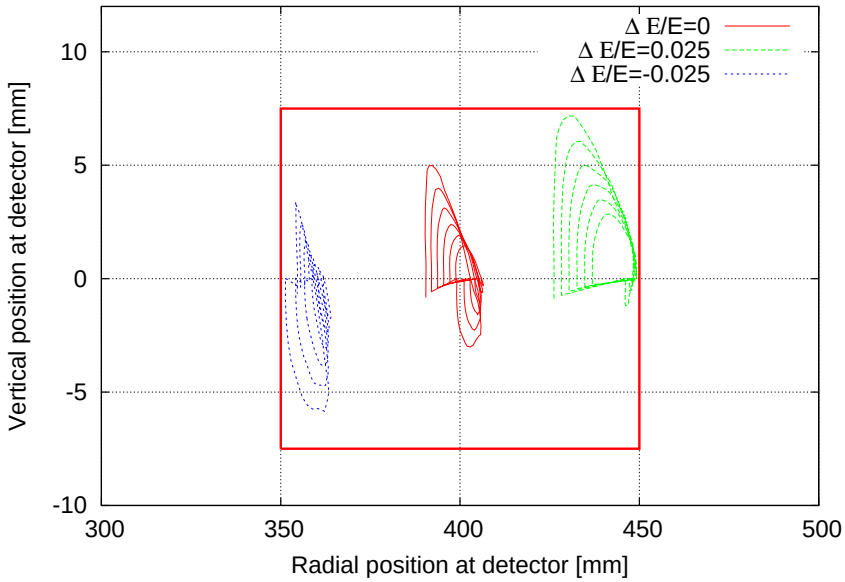

Figure 6.20 – Interception points of the particles at the detector plane. Please, note the very different scale on both axes

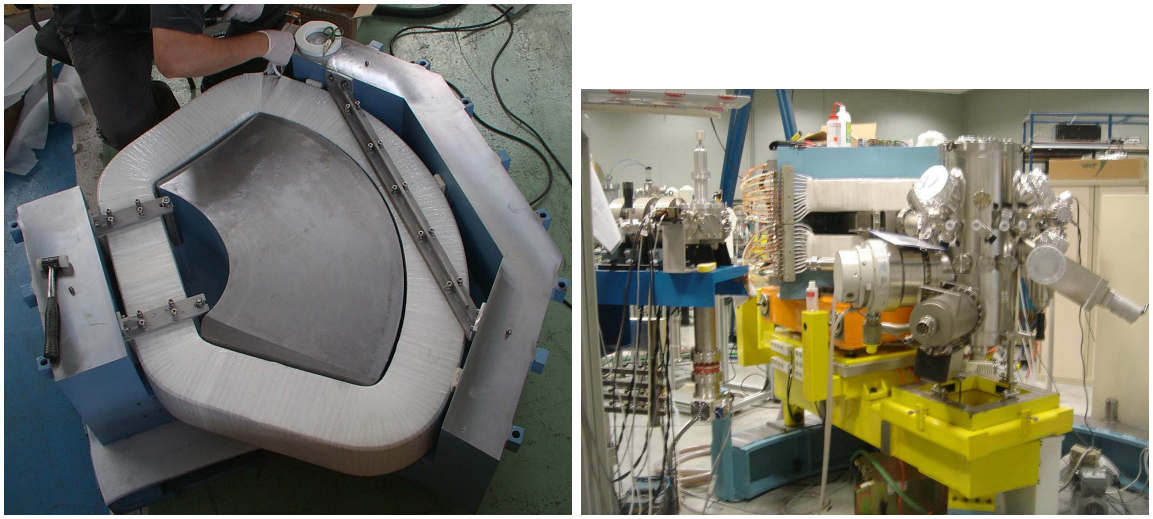

Figure 6.21 – Left, assembly of one of the magnet halves. Right, the magnet installed at the CMAM.

CHAPTER 7

Magnetics

The previous chapters have been related to the beam dynamics, otherwise stated, the way in which a certain distribution of electromagnetic field will affect an assembly of charged particles and the how they may be guided. In this chapter,we will change the focus to the methods of characterizing and creating the magnetic field, which is most often used to guide the particles at medium and high energy.

We will put emphasis on the 2D case, in which the magnet is sufficiently long with respect to the cross section, so as to produce most of it effect on the beam near its center, with the effect of the magnet extremities of minor importance. Of course, because most applications require high accuracy, the 3D effect must be added at a later stage as a perturbation of the 2D field. We will see, nevertheless, that the integral of the 3D field along a straight lines behave in many aspects as a 2D field.

7.1 The complex field and the 2D harmonic expansion

The complex formulation of the 2D magnetostatic field was introduced by Richard A. Beth, [9], [10], [11],[12], and it has become the standard formalism in accelerator magnets; both normal conducting and superconducting.

In all the following formalism, we will suppose that the magnet has its cross section on the $x-y$ plane with the beam traveling in the z direction.

The Maxwell equations limited to the magnetostatic case in vacuum are the following,

$$\nabla \cdot \vec{B} = 0 \tag{7.1}$$

$$\nabla \times \vec{B} = 0 \tag{7.2}$$

In the 2D case, these equations are reduced to the following set,

$$\frac{\partial B_x}{\partial x} = -\frac{\partial B_y}{\partial y} \tag{7.3}$$

$$\frac{\partial B_y}{\partial x} = \frac{\partial B_x}{\partial y} \tag{7.4}$$

Eqs. 7.3 and 7.4 are equivalent to the Cauchy-Riemann equations, and therefore, the following complex function is analytical,

$$F = B_y + iB_x \tag{7.5}$$

There are many consequences of the field function of eq. 7.5 being analytic. One of the most important is that if the Cauchy-Riemann conditions are satisfied in a circle of complex center ξ and radius r, the function may be expanded as a convergent Taylor series,

$$F = \sum_{n=1}^{\infty} (B_n + iA_n) \left(\frac{z-\xi}{R} \right)^{n-1} , |z-\xi| < r \tag{7.6}$$

R is a reference radius which is used to homogenize the units of the field harmonics. Typically, this reference radius is specified to be in the range of 66% to 80% of the aperture. In addition, in most cases, the circle center, ξ, around which the function is developed is taken as the origin.

Very often the integrated field is developed, as well, in the same way as the 2D field. The integrated field is defined as[1],

$$IB_x = \int_{-\infty}^{\infty} B_x(x,y,z)\, dz \tag{7.7}$$

$$IB_y = \int_{-\infty}^{\infty} B_y(x,y,z)\, dz \tag{7.8}$$

The integrals satisfy, as well, the Cauchy-Riemann conditions. This may be obtained directly by integration along z for the curl equation, while for the divergence one may be proved as,

$$\int_{-\infty}^{\infty} \left(\frac{\partial B_x}{\partial x} + \frac{\partial B_y}{\partial y} \right) dz = -\int_{-\infty}^{\infty} \frac{\partial B_z}{\partial z} dz = -B_z(\infty) + B_z(-\infty) = 0 \tag{7.9}$$

, as long as the axial cancels when we are far away the magnet ends cancels when we are far away the magnet ends. Therefore, the complex function $IB_y + iIB_x$ is analytical as well.

7.2 The field in polar coordinates

In some cases, it is interesting to obtain the polar coordinates of the magnetic field. In this section, we show how to calculate them from the complex field and how the expression of the radial field in Fourier series allows to calculate the standard field harmonics.

A simple rotation of the coordinate system in which the field is expressed provides:

$$B_r = B_x \cos\theta + B_y \sin\theta \tag{7.10}$$

$$B_\theta = -B_x \sin\theta + B_y \cos\theta \tag{7.11}$$

We can combine both expressions in a complex one

[1] In this expression and the following, z represents the Cartesian coordinate perpendicular to the cross section, and not the complex coordinate

$$(B_y + iB_x)e^{i\theta} = (B_y + iB_x)(\cos\theta + i\sin\theta) = \\ = (-B_x\sin\theta + B_y\cos\theta) + i(B_x\cos\theta + B_y\sin\theta) = (B_\theta + iB_r) \quad (7.12)$$

It is interesting to express the radial and azimuthal field from the harmonic components of the complex field.

$$(B_\theta + iB_r) = \sum_{n=1}^{\infty}(B_n + iA_n)\left(\frac{z}{R}\right)^{n-1}e^{i\theta} = \sum_{n=1}^{\infty}(B_n + iA_n)\left(\frac{r}{R}\right)^{n-1}e^{in\theta} \quad (7.13)$$

We can now write the radial field for $r = R$ as a standard Fourier series:

$$B_r = \sum_{n=1}^{\infty}(B_n\sin n\theta + A_n\cos n\theta) \quad (7.14)$$

And the field harmonics may be obtained as:

$$B_n = \frac{1}{\pi}\int_0^{2\pi} B_r(\theta)\sin n\theta\, d\theta \quad (7.15)$$

$$A_n = \frac{1}{\pi}\int_0^{2\pi} B_r(\theta)\cos n\theta\, d\theta \quad (7.16)$$

7.3 The complex potential

The field may be expressed as the derivative of the potentials, outside of the sources we may express the field as the curl of the vector potential or as the gradient of the scalar potential. For analogy with the electrical potential, we introduce a minus sign in the expression of the scalar potential.

$$\vec{B} = \nabla\times\vec{A} = -\nabla\Phi \quad (7.17)$$

We can now represent the components as the partial derivatives of either the vector or the scalar potential.

$$B_x = \frac{\partial A_z}{\partial y} = -\frac{\partial\Phi}{\partial x} \quad (7.18)$$

$$B_y = -\frac{\partial A_z}{\partial x} = -\frac{\partial\Phi}{\partial y} \quad (7.19)$$

The previous expressions may be seen as the Cauchy-Riemman conditions of the analytic function:

$$\Psi = A_z + i\phi \quad (7.20)$$

And the complex field is the derivative of the complex potential:

$$\frac{d\Psi}{dz} = -(B_y + iB_x) \tag{7.21}$$

We can now integrate the series expansion of the complex field in order to relate the standard coefficients with the complex potential. This is very useful in the post-processing of the solutions of numerical methods that calculate first the vector potential and obtain the fields as the derivative of the vector potential. In this case, obtaining the harmonics directly from the vector potential eliminates the derivative, which may introduce additional error in the final result.

$$\begin{aligned}\Psi = -\int \sum_{n=1}^{\infty} (B_n + iA_n) \left(\frac{z}{R}\right)^{n-1} dz = -\sum_{n=1}^{\infty} \frac{(B_n + iA_n)}{nR^{n-1}} z^n = \\ = -\sum_{n=1}^{\infty} \frac{(B_n + iA_n)\, r^n}{nR^{n-1}} (\cos n\theta + i \sin n\theta)\end{aligned} \tag{7.22}$$

We can obtain now the vector potential as the real part of the previous equation.

$$A_z = \sum_{n=1}^{\infty} \frac{r^n}{nR^{n-1}} (A_n \sin n\theta - B_n \cos n\theta) \tag{7.23}$$

And the standard coefficients will be:

$$B_n = -\frac{nR^{n-1}}{\pi r^n} \int_0^{2\pi} A_z(\theta) \cos n\theta \, d\theta \tag{7.24}$$

$$A_n = \frac{nR^{n-1}}{\pi r^n} \int_0^{2\pi} A_z(\theta) \sin n\theta \, d\theta \tag{7.25}$$

The expression of the scalar potential in terms of the field coefficients will be useful to obtain the pole shapes of iron dominated magnets. It is,

$$\Phi = -\sum_{n=1}^{\infty} \frac{r^n}{nR^{n-1}} (B_n \sin n\theta + A_n \cos n\theta) \tag{7.26}$$

An interesting application of eq. 7.26 is the qualitative understanding of the effect of the mechanical errors of a magnet in the field quality. For this purpose, we can use the inverse procedure, and see how much the surfaces of constant scalar magnetic potential get distorted when a multipolar term is added to the pure multipolar field that we desire to obtain. This method has been applied in fig. 7.1. A small amount of multipolar error has been introduced in the scalar potential expansion of a pure quadrupole to check which type of movements of the pole faces would caused this multipolar error. We can, for instance, observe that a pure B_3 is caused by an unequal gap between the left and right set of poles, the gap being smaller at the left than at the right for a positive B_3. For the case of A_3 the two vertical gaps are unequal.

In the case of B_4, both horizontal gaps and both vertical gaps are equal, but they are different in pairs. For instance both vertical gaps are smaller for positive B_4. The case of A_4

is different and cannot be easily identified with a displacement of the poles. It requires that the poles are deformed, with opposed poles being equal but with different curvature than the other pair of poles.

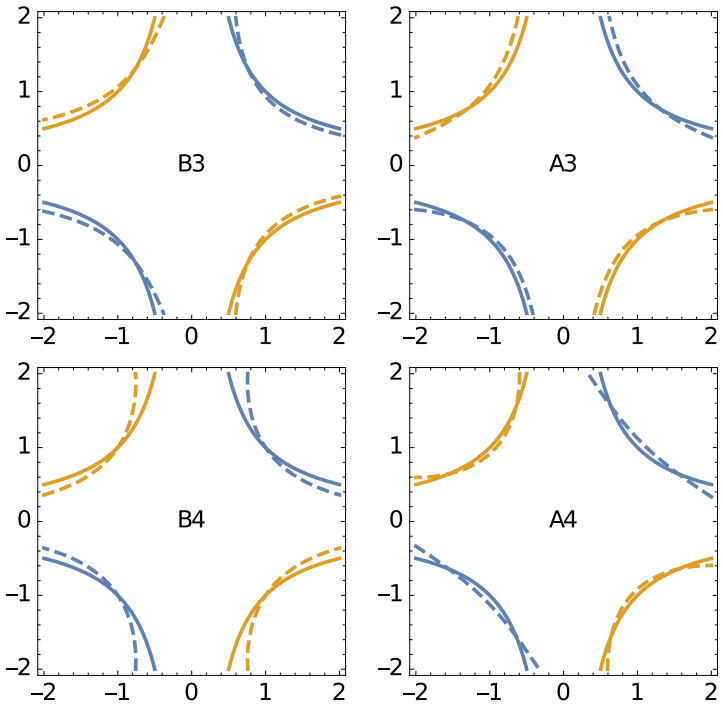

Figure 7.1 – Effect of a pure b_3, left top; a pure a_3, right top; a pure b_4, bottom left and a pure a_4 bottom right, with respect to the ideal hyperbolic shape required for a quadrupole. Both the amount of error and the dimensions are arbitrary

We can see in fig. 7.2 the application of this philosophy of measurement to a quadrupole. The relative separation between adjacent and opposite poles are measured using a column. In such a way, it is possible to correlate the error in these distances with respect to the harmonic content of the quadrupole. Using this method, it is possible to specify the mechanical tolerance required in order to achieve the desired magnetic field quality.

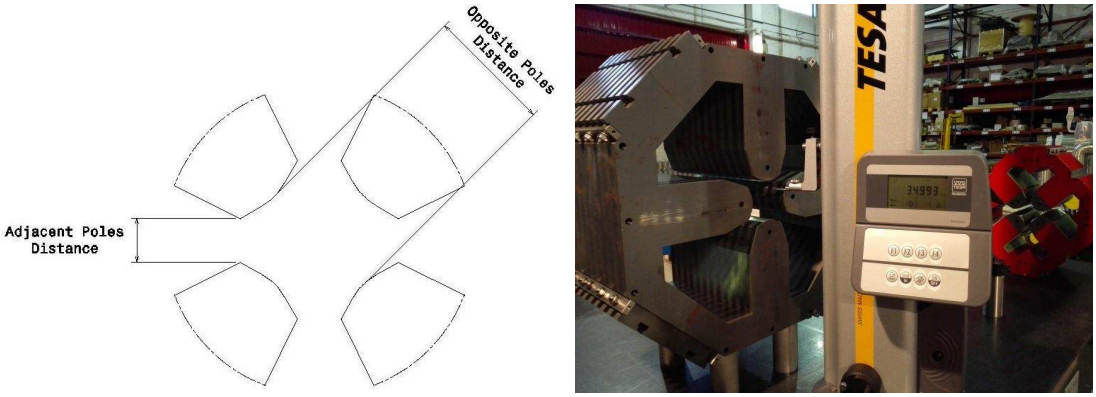

Figure 7.2 – Measuring of a quadrupole poles

7.4 Relationship between the field harmonics and the field modulus

We can calculate the field modulus in 2D by multiplying the expansion of the field in harmonics by its conjugate.

$$B_y + iB_x = \sum_{n=1}^{\infty} C_n \left(\frac{z}{R}\right)^{n-1} \tag{7.27}$$

$$B_y - iB_x = \sum_{m=1}^{\infty} \overline{C_m} \left(\frac{\bar{z}}{R}\right)^{m-1} \tag{7.28}$$

So that the modulus will be given as the double sum:

$$B^2 = \sum_{n=1}^{\infty}\sum_{m=1}^{\infty} C_n \overline{C_m} \left(\frac{r}{R}\right)^{m+n-2} e^{i(n-m)\phi} \tag{7.29}$$

Where we have expressed z in polar form. Now, we will suppose that the field has a very dominant harmonic of order p, which is the case in most technically relevant systems, in which we are interested in obtaining a pure multipole and the other terms are only perturvative. Letts suppose then that $|C_p| \gg |C_m|$ for all $p \neq m$. In this case, only the terms containing C_p will be relevant. In addition, we will suppose that only the normal harmonic (and not the skew) is desired, so that $C_p = B_p$ is a real number. We may write the field modulus as:

$$\begin{aligned} B^2 &= B_p \sum_{n-p=1}^{\infty} \left(\overline{C_n} e^{-i(n-p)\phi} + C_n e^{i(n-p)\phi}\right) \left(\frac{r}{R}\right)^{n+p-2} e^{i(n-p)\phi} + B_p^2 \left(\frac{r}{R}\right)^{2p-2} = \\ &= B_p \sum_{n-p=1}^{\infty} 2\left(B_n \cos(n-p)\phi - A_n \sin(n-p)\phi\right) \left(\frac{r}{R}\right)^{n+p-2} + B_p^2 \left(\frac{r}{R}\right)^{2p-2} \end{aligned} \tag{7.30}$$

We can now reformulate eq. 7.30 to obtain the relative error to the main field:

$$\frac{B^2 - B_p^2 \left(\frac{r}{R}\right)^{2p-2}}{B_p^2 \left(\frac{r}{R}\right)^{2p-2}} = \sum_{n-p=1}^{\infty} 2\left(\frac{B_n}{B_p}\cos(n-p)\phi - \frac{A_n}{B_p}\sin(n-p)\phi\right) \left(\frac{r}{R}\right)^{n-p} \tag{7.31}$$

This equation relates the error in the modulus of the field at a certain radius with the relative harmonics of other existing angular frequencies. The ripple to the otherwise uniform modulus appears at the $n - p$ angular frequency.

7.5 Transformation of the field harmonics

7.5.1 Translation of the reference frame for the harmonic expansion

In some cases it is interesting to translate by a complex number δ the reference system of the magnet. This is made for instance to align the measurement axis with the mechanical axis in order to cancel the dipole component of the field. As we will see, the higher harmonics contribute to the lower ones in a series that converges as powers of $|\delta|/R$. If we apply a

displacement to the harmonics, the field expansion in the new coordinates will be:

$$(B_y + iB_x) = \sum_{n=1}^{\infty} C_n \left(\frac{z+\delta}{R}\right)^{n-1} = \sum_{n=1}^{\infty} C_n \frac{\sum_{j=0}^{n-1} \binom{n-1}{j} z^{n-1-j}\delta^j}{R^{n-1}} = \sum_{n=1}^{\infty}\sum_{j=0}^{n-1} C_n \binom{n-1}{j} \frac{z^{n-1-j}\delta^j}{R^{n-1}} \tag{7.32}$$

We can now group all terms of constant power in the complex coordinate by making the substitution $k = n - j$.

$$(B_y + iB_x) = \sum_{k=1}^{\infty}\sum_{j=0}^{\infty} C_{k+j} \binom{k+j-1}{j} \left(\frac{\delta}{R}\right)^j \left(\frac{z}{R}\right)^{k-1} \tag{7.33}$$

This expression is the expansion of the field around the new point, with the new field coefficients being:

$$\bar{C_k} = \sum_{j=0}^{\infty} C_{k+j} \binom{k+j-1}{j} \left(\frac{\delta}{R}\right)^j \tag{7.34}$$

7.5.2 Rotation of the measurement around the vertical axis

One interesting transformation is the rotation of the magnet around the y axis. This is useful because sometimes a magnet must be measured independently from both sides, because the probe is not long enough or for any other reason.

First of all, the new complex reference system has the sign of the x coordinate changed:

$$z' = -x + iy = -\bar{z} \tag{7.35}$$

And additionally, the x coordinate of the complex field has changed of sign.

$$F' = B_y - iB_x = \bar{F} \tag{7.36}$$

The new expansion will be:

$$\begin{aligned} F' = \bar{F} = \overline{\sum_{n=1}^{\infty} (B_n + iA_n) \left(\frac{z}{R}\right)^{n-1}} = \sum_{n=1}^{\infty} (B_n - iA_n) \left(\frac{\bar{z}}{R}\right)^{n-1} = \\ = \sum_{n=1}^{\infty} (B_n - iA_n) \left(\frac{-z'}{R}\right)^{n-1} = \sum_{n=1}^{\infty} \left((-1)^{n-1} B_n + i(-1)^n A_n\right) \left(\frac{z'}{R}\right)^{n-1} \end{aligned} \tag{7.37}$$

And therefore,

$$B'(n) = (-1)^{n-1} B_n \tag{7.38}$$

$$A'(n) = (-1)^n A_n \tag{7.39}$$

Which we could rephrase as even normal harmonics and odd skew harmonics change sign.

7.6 Magnetic field calculations for 2D current and magnetization distributions

The theory of the complex field may be used to obtain powerful results for current dominated magnetic systems. Instead of adding up the contribution of the different current lines to the magnetic field in a given point of space, we will show that it is possible to obtain the harmonic contribution of the line of current to the complete interior field problem and add up the contribution of the different line currents to a given harmonic.

The use of the complex formulation to analyze a permanent magnet system has been used at least since [31], here we obtain the same results and a few more using a different method. The key is the used of the complex magnetic moment, that will be defined in section. 7.7. In this work, we will concentrate in the Hallbach type arrangement, although some other approaches like the quasi-sheet multipole [48] may be advantageous in some cases.

7.6.1 Field of current lines and current distributions

To calculate the field created by a current line, we will suppose without loss of generality that the current line is located at the origin. In this case, Ampere law may be expressed as,

$$B_r = 0 \tag{7.40}$$

$$B_\theta = \frac{\mu_0 I}{2\pi r} \tag{7.41}$$

From eq. 7.12, we can obtain the complex field as,

$$B_y + iB_x = e^{-i\theta}\left(B_r + iB_\theta\right) = \frac{\mu_0 i}{2\pi z} \tag{7.42}$$

For a current line of value I, located at the complex position ξ, the value at the complex point z may be obtained by a shift of eq. 7.42,

$$F = \frac{\mu_0 I}{2\pi\left(z-\xi\right)} \tag{7.43}$$

We could expand in an harmonic series the complex field and obtain directly the harmonics from the position of the current line. We will take the particular case of an internal field $|z| < |\xi|$.

$$F = \frac{\mu_0 I}{2\pi\left(z-\xi\right)} = -\frac{\mu_0 I}{2\pi\xi\left(1-\frac{z}{\xi}\right)} = -\frac{\mu_0 I}{2\pi\xi}\sum_{n=1}^{\infty}\left(\frac{z}{\xi}\right)^{n-1} \tag{7.44}$$

If we compare it now with the standard complex harmonic distribution, we will obtain:

$$B_n + iA_n = -\frac{\mu_0 I R^{n-1}}{2\pi\xi^n} \tag{7.45}$$

7.6.2 Harmonics of a line current distribution

We could integrate now eq. 7.45 to obtain the harmonics of a constant surface current sheet of linear current density λ going from complex points ξ_1 to ξ_2. In this case we can parametrize the complex variable with a parameter t going from 0 to 1 and the integral will be:

$$B_n + iA_n = -\frac{\mu_0 \lambda R^{n-1}}{2\pi} \int_0^1 \frac{|\xi_2 - \xi_1|\, dt}{(\xi_1 + (\xi_2 - \xi_1)t)^n} =$$
$$= -\frac{\mu_0 \lambda R^{n-1}}{2\pi} \frac{|\xi_2 - \xi_1|}{(\xi_2 - \xi_1)} \int_0^1 \frac{(\xi_2 - \xi_1)\, dt}{(\xi_1 + (\xi_2 - \xi_1)t)^n} = \begin{cases} -\frac{\mu_0 \lambda R^{n-1}}{2\pi} \frac{|\xi_2 - \xi_1|}{(\xi_2 - \xi_1)} \ln \frac{\xi_2}{\xi_1} & \text{if } n = 1, \\ \frac{\mu_0 \lambda R^{n-1}}{2\pi(n-1)} \frac{|\xi_2 - \xi_1|}{(\xi_2 - \xi_1)} \left(\frac{1}{\xi_2^{n-1}} - \frac{1}{\xi_2^{n-1}} \right) & \text{if } n > 1. \end{cases} \tag{7.46}$$

7.7 The field of a magnetic dipole

In this section, we will extend the complex formalism to include the field generated by 2D magnetic dipoles. We could imagine two current lines of the same value but different sign placed at a complex distance, Δ, the situation if shown in fig. 7.3. The complex field would be,

$$F = \frac{\mu_0 I}{2\pi} \left(\frac{1}{z - (\xi + \Delta/2)} - \frac{1}{z - (\xi - \Delta/2)} \right) = \frac{\mu_0 I}{2\pi} \frac{-\Delta}{(z - \xi)^2 - (\Delta/2)^2} \tag{7.47}$$

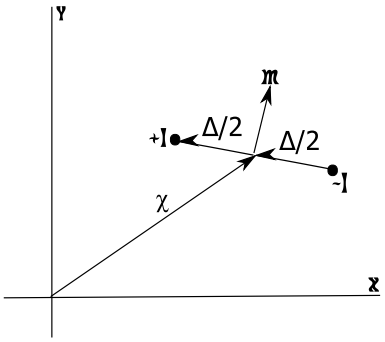

Figure 7.3 – Calculation of the field of two current lines

We could take now the limit of Δ to zero, while the product $I\Delta$ takes a finite value. To relate the magnitudes that we are using with the conventional magnetic moment (per unit length), we should do:

$$m = iI\Delta \tag{7.48}$$

As the magnetic moment is perpendicular to the line that goes from the positive to the negative current line. Finally, the complex field of a magnetic moment per unit length m located at the complex coordinate ξ, at a complex coordinate z will be:

$$F = \frac{\mu_0 m i}{2\pi \left(z - \xi\right)^2} \tag{7.49}$$

We will now expand the complex field in powers of z for an internal field. This is indicated for magnets used for beam focusing or steering. If $|z| < |\xi|$, then:

$$F = \frac{\mu_0 m i}{2\pi \left(z - \xi\right)^2} = \frac{\mu_0 m i}{2\pi \xi^2 \left((z/\xi) - 1\right)^2} = \frac{\mu_0 m i}{2\pi \xi^2} \sum_{n=1}^{\infty} n \left(\frac{z}{\xi}\right)^{n-1} \tag{7.50}$$

The usual field expansion used for accelerator magnets is:

$$F = B_y + i B_x = \sum_{n=1}^{\infty} \left(B_n + i A_n\right) \left(\frac{z}{R}\right)^{n-1} \tag{7.51}$$

Where R is an arbitrary reference radius which is used so that all harmonics B_n and A_n have dimensions of magnetic induction. We may compare eq. 7.50 and eq. 7.51 to obtain the harmonic contribution for the dipole m at position ξ:

$$B_n + i A_n = \frac{i \mu_0 m n R^{n-1}}{2\pi \xi^{n+1}} \tag{7.52}$$

A very interesting property of eq. 7.52 is its linearity with respect to the complex magnetization m. This linearity affects both the modulus and the argument of the complex magnetization. Therefore, if the magnetization is rotated by an angle ϕ, the complex magnetization will be multiplied by a factor $e^{i\theta}$ and so will be the complex field. This property is very useful when understanding the effect of angular error in the magnetization of the permanent magnet blocks.

7.8 Generation of pure multipoles

Eq. 7.52 may be used for obtaining a magnetization distribution which creates a pure harmonic field. If we express the field source position ξ in radius and angle, we obtain:

$$B_n + i A_n = \frac{i \mu_0 m n R^{n-1}}{2\pi r^{n+1}} \left(\cos(n+1)\phi - i \sin(n+1)\phi\right) \tag{7.53}$$

We will calculate the effect of magnetization per unit of surface M_s which is of constant modulus and rotates m times over a complete turn of 2π, i.e.:

$$dm = i M_s e^{im\phi} r d\phi \tag{7.54}$$

The complex unit i in front of the second term is used to align the magnetization with the complex axis at ϕ equal zero. We can perform the integration over the *crust* to obtain:

$$B_n + iA_n = \frac{i\mu_0 M_s n R^{n-1}}{2\pi r^n}\int_0^{2\pi} ie^{im\phi}e^{-i(n+1)\phi}d\phi = \\ -\frac{\mu_0 M_s n R^{n-1}}{2\pi r^n}\int_0^{2\pi} e^{i(m-(n+1))\phi}d\phi = \begin{cases} 0 & \text{if } m \neq n+1, \\ -\frac{\mu_0 M_s n R^{n-1}}{r^n} & \text{if } m = n+1. \end{cases} \quad (7.55)$$

This equation may be generalized to a shell of finite thickness by integrating the result over r. Letts assume now that we have the appropriate rotation of the magnetization ($m = n+1$) and that the magnetization per unit of volume is M. In this case,we will obtain:

$$B_n = -\mu_0 M n R^{n-1}\int_{r_1}^{r_2}\frac{dr}{r^n} = \begin{cases} \frac{\mu_0 M n R^{n-1}}{n-1}\left(\frac{1}{r_1^{n-1}} - \frac{1}{r_2^{n-1}}\right) & \text{if } n \neq 1, \\ -\mu_0 M \ln\frac{r_2}{r_1} & \text{if } n = 1. \end{cases} \quad (7.56)$$

For a practical magnet of relative permeability near 1, the product of the vacuum permeability times the magnetization is the residual magnetization B_r. For a quadrupole, and taking into account that the gradient is B_2 divided by the reference radius, we obtain the value:

$$g = 2B_r\left(\frac{1}{r_1} - \frac{1}{r_2}\right) \quad (7.57)$$

A similar expression may be obtained for a dipole,

$$B_1 = -B_r \ln\frac{r_2}{r_1} \quad (7.58)$$

An interesting property of eq. 7.58, is that B_1 may be significantly larger than B_r, depending on the geometry of the magnet. The value of the residual magnetization is not limiting the achievable central field. The field that may be reached is only limited by the demagnetizing field on the point where it is higher on any point on the magnets. Therefore, achieving high field does not only require a high B_r, but also a high irreversible demagnetizing field H_{ci}. The exact definition of each property will be given in chapter 8.

7.9 The Green's theorem in complex formulation

In this section, we proof a complex form of the Green Theorem which we will use to integrate the effect of blocks of homogeneous magnetization. The Green's theorem, states that for a given plane region $\Re$ an area integral is related to a line integral over the perimeter C.

$$\oint_C M\,dx + N\,dy = \iint_{\Re}\left(\frac{\partial N}{\partial x} - \frac{\partial M}{\partial y}\right)dx\,dy \quad (7.59)$$

If now, z is the complex variable $x + iy$, we can calculate the following complex contour integral by the Greents theorem.

$$\oint_C f(z)\bar{z}\,dz = \oint_C f(z)(x - iy)\,dx + f(z)(y + ix)dy \quad (7.60)$$

So that we may identify:

$$M = f(z)(x - iy) \tag{7.61}$$
$$N = f(z)(y + ix) \tag{7.62}$$

If we calculate the partial derivatives needed by the Greenŧs theorem, we obtain:

$$\frac{\partial M}{\partial y} = f'(z)i(x - iy) - f(z)i \tag{7.63}$$
$$\frac{\partial N}{\partial x} = f'(z)(y + ix) + f(z)i \tag{7.64}$$

The first terms will cancel in the subtraction of the integrand while the second will add up, giving an expression that may be used to calculate integrals of complex functions over regions of the complex plane:

And applying the Green's theorem:

$$\iint_{\Re} f(z)\,dx\,dy = \frac{1}{2i}\oint_C f(z)\bar{z}\,dz \tag{7.65}$$

It must be noted, nevertheless, that the integrand is not an analytic function because of the presence of the conjugate and the method of residues cannot be used to evaluate the integral. Of course, according to the Cauchy integral theorem, the function cannot be analytical if the integral must have a non-zero value.

7.10 Surface currents on the sides of constant magnetization blocks

From the point of view of the field generated outside the blocks, the magnetization may be replaced by a surface density current equal to the curl of the magnetization plus a linear current density on the edges of the block of value $\vec{M} \times \vec{n}$, where $\vec{n}$ is the normal pointing outside of the block. Therefore the linear current density, in 2D, will be:

$$\lambda = M_x n_y - M_y n_x = -\left(\tau_x M_x + \tau_y M_y\right) \tag{7.66}$$

$$\lambda\,ds = -\frac{1}{2}\left(M d\bar{\xi} + \bar{M} d\xi\right) \tag{7.67}$$

7.11 Harmonics of blocks of constant magnetization

We can now combine eq. 7.52, with Greenŧs theorem to obtain the harmonics of a block of constant magnetization by a line integral on the contour of the block.

$$B_n + iA_n = \iint_A \frac{i\mu_0 M n R^{n-1}}{2\pi\xi^{n+1}} dxdy = \frac{\mu_0 M n R^{n-1}}{4\pi}\oint_C \frac{\bar{\xi}\,d\xi}{\xi^{n+1}} \tag{7.68}$$

It is now possible to integrate by parts the line integral in order to obtain a simplified expression.

$$\oint_C \frac{\bar{\xi}\, d\xi}{\xi^{n+1}} = -\frac{\bar{\xi}}{n\xi^n} + \frac{1}{n}\oint_C \frac{d\bar{\xi}}{\xi^n} = \frac{1}{n}\oint_C \frac{d\bar{\xi}}{\xi^n} \tag{7.69}$$

Because the part that goes out of the integral cancels over a closed loop. We obtain finally:

$$B_n + iA_n = \frac{\mu_0 M R^{n-1}}{4\pi}\oint_C \frac{d\bar{\xi}}{\xi^n} \tag{7.70}$$

It is interesting to note that the effect of the constant magnetization block may be obtained in a different but related way. As shown in the previous section, the field of the block may be obtained by replacing the magnetization by a surface current density on the outer surface of the block with value $\lambda = \vec{n} \times \vec{M}$, where $\vec{n}$ is the vector normal to the block.

7.11.1 Harmonics created by a cylinder of uniform magnetization

As a first example of the use of eq. 7.70, we will calculate the harmonics created by a cylinder of constant magnetization. Fig. 7.4 shows the geometry used for the calculation, the circle is centered on the complex number ξ_0 and has a radius r.

The circle may be parametrized by equation:

$$\xi = \xi_0 + re^{i\phi}, \qquad 0 \le \phi < 2\pi \tag{7.71}$$

The harmonics created by the cylinder will be:

$$B_n + iA_n = \frac{\mu_0 M R^{n-1}}{4\pi}\oint_0^{2\pi} \frac{-ire^{-i\phi}\, d\phi}{(\xi_0 + re^{i\phi})^n} = -\frac{i\mu_0 M R^{n-1} r}{4\pi\xi_0^n}\oint_0^{2\pi} \frac{e^{-i\phi}\, d\phi}{\left(1 + \frac{re^{i\phi}}{\xi_0}\right)^n} \tag{7.72}$$

As long as the origin is not contained in the cylinder $|\xi_0| > r = |re^{i\phi}|$, and therefore the denominator may be expanded as:

$$B_n + iA_n = -\frac{i\mu_0 M R^{n-1} r}{4\pi\xi_0^n}\oint_0^{2\pi} e^{-i\phi}\left(1 - n\frac{re^{i\phi}}{\xi_0} + \frac{1}{2}n(n+1)\frac{r^2 e^{2i\phi}}{\xi_0^2} - \cdots\right) d\phi \tag{7.73}$$

Only the term in the parenthesis that contains the term $e^{i\phi}$ will contribute to the total integral and the final result will be:

$$B_n + iA_n = \frac{i\mu_0 M R^{n-1} r^2}{2\xi_0^{n+1}} \tag{7.74}$$

7.11.2 General polygonal block

For a general polygonal block, we will use the integral of eq. 7.70 over the external shape. An example of the geometry may be seen in fig. 7.5. The polygon will be made by a series of edges with a running index e, each of them going from vertex ξ_e to vertex ξ_{e+1}. The closed loop integral will be replaced by an integral over the edges, which each edge parametrized as,

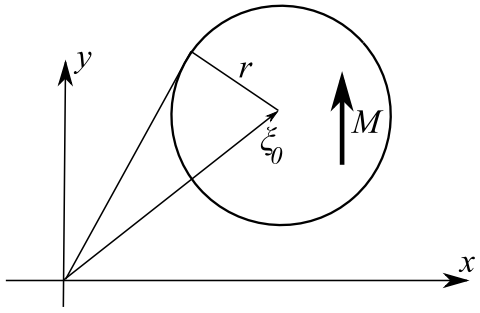

Figure 7.4 – Geometry used to calculate the effect of a uniformly magnetized cylinder.

$$\xi = (\xi_{e+1} - \xi_e)\, t + \xi_e \tag{7.75}$$

So that the ξ dependent part of eq. 7.70 may be expressed as,

$$\oint_c \frac{d\overline{\xi}}{\xi^n} = \sum_e \int_0^1 \frac{\overline{(\xi_{e+1} - \xi_e)} dt}{((\xi_{e+1} - \xi_e)\, t + \xi_e)^n} = \frac{1}{n-1} \sum_e \frac{\overline{(\xi_{e+1} - \xi_e)}}{(\xi_{e+1} - \xi_e)} \begin{cases} \left(\frac{1}{\xi_e^{n-1}} - \frac{1}{\xi_{e+1}^{n-1}} \right), \text{for } n \neq 1 \\ \ln \frac{\xi_e}{\xi_{e+1}}, \text{ for } n = 1 \end{cases} \tag{7.76}$$

This equation contains a term which is the ratio between the conjugate of the complex number defining the edge and the edge itself, $(\xi_{e+1} - \xi_e)$. If we define the edge in modulus and argument, $r_e \exp(i\theta_e)$, the ratio will be $\exp(-2i\theta_e)$. This a complex number obtained by squaring the unitary complex number parallel to the edge and making a symmetry on the real axis. This term is a complex number of unitary modulus, that multiplies the contribution of the edge, and that actually avoids the integral being null because the direct contribution of each vertex appears twice in the complete integral, the first time with positive sign and the second with negative sign. The contribution of each vertex may be obtained by subtracting the edge term of the edges that share the vertex. In this case, the summation on the edges of eq. 7.76, may be replaced by a summation over the vertices of the polygon. The contribution of the edges and the vertices for a square may be seen on the right side of fig. 7.5.

For instance for a rectangular block with edges parallel to the axis the field harmonics will be given by eq. 7.78.

$$B_n + iA_n = \frac{\mu_0 M R^{n-1}}{2\pi(n-1)} \left(\frac{1}{\xi_1^{n-1}} - \frac{1}{\xi_2^{n-1}} + \frac{1}{\xi_3^{n-1}} - \frac{1}{\xi_4^{n-1}} \right) \text{if } n \neq 1 \tag{7.77}$$

$$B_1 + iA_1 = -\frac{\mu_0 M}{2\pi} \ln \left(\frac{\xi_1 \xi_3}{\xi_2 \xi_4} \right) \tag{7.78}$$

7.12 Structures made of several blocks

For calculating the effect of the other blocks of the magnet we will not integrate the blocks in their actual position, but we will transfer them to the real axis as the first block in fig. 7.5 calculate the harmonics using eqs. 7.77 and 7.78 and then translating the harmonics to the

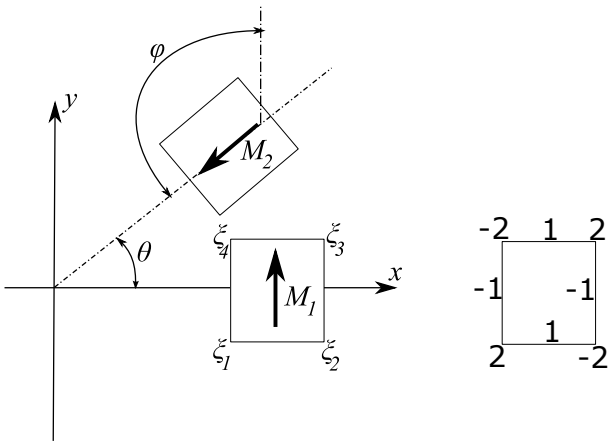

Figure 7.5 – Left, calculation of the harmonics created by a constant magnetization block. Right, terms associated to the edge angle and contribution to the vertex term for a square with the edges parallel to the axes.

original reference system. If we consider the prime system as the one having the real axis coincident with the mid-plane of the second block in fig. 7.5. The harmonics created by the second block on the prime system will be coincident with the harmonics created by the first block on the original coordinate system , C_{n0}. Of course, to be so, the magnetization of the second block must keep the same angle with the prime real axis as the magnetization of the first block with the reference real axis. Taking into account this additional rotation of the magnetization and the absolute rotation ϕ, the harmonics created in the reference system by block 2, will be:

$$C_{n1} = C_{n0} e^{-in\theta} e^{-i\theta} e^{i\phi} = C_{n1} e^{i(\phi-(n+1)\theta)} \tag{7.79}$$

If we choose a rotation of the magnetization ϕ which is equal to $(n+1)\theta$, we obtain that the contribution to the n^{th} harmonic is constant for the first and the second block. Of course, this can be generalized to an arbitrary number of blocks.

Letts now concentrate in a special case of technical interest. The magnet is formed from s sectors, each an angle of $2\pi/s$, running from $b = 0$ to $b = s - 1$. We wish to create the m^{th} harmonic, so that we choose $\phi = (m+1)\theta$. In this case, we have:

$$C_{nb} = C_{n0} e^{-2\pi i \frac{b(n-m)}{s}}. \tag{7.80}$$

A similar equation is obtained, but not added at [39].

This is, obviously a geometrical series, where b is the power of each term. It is possible to sum the effect of all the blocks to obtain the total field:

$$C_n = C_{n0} \sum_{b=0}^{s-1} e^{-2\pi i \frac{b(n-m)}{s}} = C_{n0} \frac{1 - e^{-2\pi i (n-m)}}{1 - e^{-2\pi i \frac{n-m}{s}}} = \begin{cases} 0 & \text{if } (n-m)/s \text{ is not an integer} \\ sC_{n0} & \text{if } (n-m)/s \text{ is integer} \end{cases} \tag{7.81}$$

According to the result of eq. 7.81, the harmonics created by the blocks are 0 except

for some allowed harmonics, in which case, the contribution of each block is the same. For instance, to calculate the effect on the desired harmonic, $n = m$, it is sufficient to multiply the result of the first block by the number of blocks, s.

It is very interesting to see the individual effect of the magnetization of each block in the field harmonics. We can do it by calculating each coefficient of eq. 7.80 for a particular case. For instance, in eq. 7.82, we show the individual contributions of each block to the field harmonics for an 8 block quadrupole (m=2,s=8).

$$\begin{pmatrix} C_1 \\ C_2 \\ C_3 \\ C_4 \\ C_5 \\ C_6 \\ C_7 \\ C_8 \\ C_9 \\ C_{10} \end{pmatrix} = \frac{C_{n0}}{M_0} \begin{pmatrix} 1 & e^{\frac{i\pi}{4}} & i & e^{\frac{3i\pi}{4}} & -1 & e^{-\frac{3i\pi}{4}} & -i & e^{-\frac{i\pi}{4}} \\ 1 & 1 & 1 & 1 & 1 & 1 & 1 & 1 \\ 1 & e^{-\frac{i\pi}{4}} & -i & e^{-\frac{3i\pi}{4}} & -1 & e^{\frac{3i\pi}{4}} & i & e^{\frac{i\pi}{4}} \\ 1 & -i & -1 & i & 1 & -i & -1 & i \\ 1 & e^{-\frac{3i\pi}{4}} & i & e^{-\frac{i\pi}{4}} & -1 & e^{\frac{i\pi}{4}} & -i & e^{\frac{3i\pi}{4}} \\ 1 & -1 & 1 & -1 & 1 & -1 & 1 & -1 \\ 1 & e^{\frac{3i\pi}{4}} & -i & e^{\frac{i\pi}{4}} & -1 & e^{-\frac{i\pi}{4}} & i & e^{-\frac{3i\pi}{4}} \\ 1 & i & -1 & -i & 1 & i & -1 & -i \\ 1 & e^{\frac{i\pi}{4}} & i & e^{\frac{3i\pi}{4}} & -1 & e^{-\frac{3i\pi}{4}} & -i & e^{-\frac{i\pi}{4}} \\ 1 & 1 & 1 & 1 & 1 & 1 & 1 & 1 \end{pmatrix} \cdot \begin{pmatrix} M_0 \\ M_1 \\ M_2 \\ M_3 \\ M_4 \\ M_5 \\ M_6 \\ M_7 \end{pmatrix} \tag{7.82}$$

And the matrix for a 16 block magnet is:

$$\begin{pmatrix} 1 & e^{\frac{i\pi}{8}} & e^{\frac{i\pi}{4}} & e^{\frac{3i\pi}{8}} & i & e^{\frac{5i\pi}{8}} & e^{\frac{3i\pi}{4}} & e^{\frac{7i\pi}{8}} & -1 & e^{-\frac{7i\pi}{8}} & e^{-\frac{3i\pi}{4}} & e^{-\frac{5i\pi}{8}} & -i & e^{-\frac{3i\pi}{8}} & e^{-\frac{i\pi}{4}} & e^{-\frac{i\pi}{8}} \\ 1 & 1 & 1 & 1 & 1 & 1 & 1 & 1 & 1 & 1 & 1 & 1 & 1 & 1 & 1 & 1 \\ 1 & e^{-\frac{i\pi}{8}} & e^{-\frac{i\pi}{4}} & e^{-\frac{3i\pi}{8}} & -i & e^{-\frac{5i\pi}{8}} & e^{-\frac{3i\pi}{4}} & e^{-\frac{7i\pi}{8}} & -1 & e^{\frac{7i\pi}{8}} & e^{\frac{3i\pi}{4}} & e^{\frac{5i\pi}{8}} & i & e^{\frac{3i\pi}{8}} & e^{\frac{i\pi}{4}} & e^{\frac{i\pi}{8}} \\ 1 & e^{-\frac{i\pi}{4}} & -i & e^{-\frac{3i\pi}{4}} & -1 & e^{\frac{3i\pi}{4}} & i & e^{\frac{i\pi}{4}} & 1 & e^{-\frac{i\pi}{4}} & -i & e^{-\frac{3i\pi}{4}} & -1 & e^{\frac{3i\pi}{4}} & i & e^{\frac{i\pi}{4}} \\ 1 & e^{-\frac{3i\pi}{8}} & e^{-\frac{3i\pi}{4}} & e^{\frac{7i\pi}{8}} & i & e^{\frac{i\pi}{8}} & e^{-\frac{i\pi}{4}} & e^{-\frac{5i\pi}{8}} & -1 & e^{\frac{5i\pi}{8}} & e^{\frac{i\pi}{4}} & e^{-\frac{i\pi}{8}} & -i & e^{-\frac{7i\pi}{8}} & e^{\frac{3i\pi}{4}} & e^{\frac{3i\pi}{8}} \\ 1 & -i & -1 & i & 1 & -i & -1 & i & 1 & -i & -1 & i & 1 & -i & -1 & i \\ 1 & e^{-\frac{5i\pi}{8}} & e^{\frac{3i\pi}{4}} & e^{\frac{i\pi}{8}} & -i & e^{\frac{7i\pi}{8}} & e^{\frac{i\pi}{4}} & e^{-\frac{3i\pi}{8}} & -1 & e^{\frac{3i\pi}{8}} & e^{-\frac{i\pi}{4}} & e^{-\frac{7i\pi}{8}} & i & e^{-\frac{i\pi}{8}} & e^{-\frac{3i\pi}{4}} & e^{\frac{5i\pi}{8}} \\ 1 & e^{-\frac{3i\pi}{4}} & i & e^{-\frac{i\pi}{4}} & -1 & e^{\frac{i\pi}{4}} & -i & e^{\frac{3i\pi}{4}} & 1 & e^{-\frac{3i\pi}{4}} & i & e^{-\frac{i\pi}{4}} & -1 & e^{\frac{i\pi}{4}} & -i & e^{\frac{3i\pi}{4}} \\ 1 & e^{-\frac{7i\pi}{8}} & e^{\frac{i\pi}{4}} & e^{-\frac{5i\pi}{8}} & i & e^{-\frac{3i\pi}{8}} & e^{\frac{3i\pi}{4}} & e^{-\frac{i\pi}{8}} & -1 & e^{\frac{i\pi}{8}} & e^{-\frac{3i\pi}{4}} & e^{\frac{3i\pi}{8}} & -i & e^{\frac{5i\pi}{8}} & e^{-\frac{i\pi}{4}} & e^{\frac{7i\pi}{8}} \\ 1 & -1 & 1 & -1 & 1 & -1 & 1 & -1 & 1 & -1 & 1 & -1 & 1 & -1 & 1 & -1 \end{pmatrix} \tag{7.83}$$

The interesting part of eq. 7.82, is that it may be used for sorting the permanent magnets used for assembling the quadrupole. This is so, because ot is clearly shown which pairs (or groups of magnet) cancel each other for each harmonics. For instance, for the 8 blocks structure, we can derive the following consequences,

1. The dipole field is canceled by having diametrically opposed magnets of the same magnetization. This is clear from the fact that in the first row of the matrix, elements four columns apart have the same value but of opposite sign

2. The second row shows that the quadrupole is an allowed harmonic. All blocks contribute the same to the harmonic. The same is true for the last row (C_{10}).

3. Specially interesting is the case of C_6, this harmonic is allowed by the quadrupolar symmetry, but in our case, it cancels if the magnets in the even and the odd positions are equal. In real magnets with a relative permeability different of 1, the magnets in the

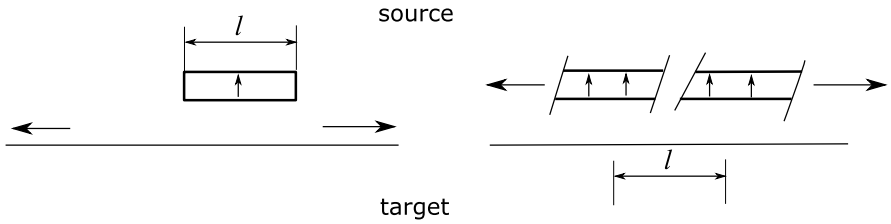

Figure 7.6 – Sketch of the duality of the integral field of a finite system (left) and the relationship to the solution of the 2D case

odd positions are under a larger demagnetizing field, and the actual magnetization is smaller. This originates a C_6 component because it is allowed by the problem symmetry.

7.13 Relationship between the 2D and the 3D case

An important point for the practical use of the complex, 2D, expressions is how well they relate to the engineering systems they will be used at, which are, of course of finite length. In this section we will prove that for systems of constant section along one axis the 2D solutions my be used without losing any accuracy. Letts imagine a system of constant cross section A, on which a magnetization is imposed, which extends from 0 to l over the z axis (left of fig. 7.6).

The field at any point of the space may be found by integrating over the sources a certain kernel.

$$\vec{B}(x,y,z) = \iint_A dx_s dy_s \int_0^l dz_s \vec{\vec{G}}(x-x_s, y-y_s, z-z_s) \cdot \vec{M}\,(x_s, y_s, z_s) \tag{7.84}$$

For the distributed magnetization system, the integrating kernel is shown in eq. 7.85, although we will not use explicit use of it.

$$\begin{pmatrix} B_x \\ B_y \\ B_z \end{pmatrix} = \begin{pmatrix} \frac{3x^2}{r^5} - \frac{1}{r^3} & \frac{3xy}{r^5} & \frac{3xz}{r^5} \\ \frac{3xy}{r^5} & \frac{3y^2}{r^5} - \frac{1}{r^3} & \frac{3zy}{r^5} \\ \frac{3xz}{r^5} & \frac{3zy}{r^5} & \frac{3z^2}{r^5} - \frac{1}{r^3} \end{pmatrix} \cdot \begin{pmatrix} m_x \\ m_y \\ m_z \end{pmatrix} \tag{7.85}$$

For beam optics in paraxial approximation, we will be interested in the integral of the magnetic field over lines parallel to the central trajectory, eq. 7.86.

$$I\vec{B}(x,y) = \int_{-\infty}^{\infty} \vec{B}(x,y,z)dz = \iint_A dx_s dy_s \int_0^l dz_s \int_{-\infty}^{\infty} dz \vec{\vec{G}}(x-x_s, y-y_s, z-z_s) \cdot \vec{M}\,(x_s, y_s, z_s) \tag{7.86}$$

If we make the following substitution of variables:

$$z_s = z_s \tag{7.87}$$

$$z = z_s + u \tag{7.88}$$

We can decouple the integral on the longitudinal axis over the kernel and over the magne-

tization.

$$I\vec{B}(x,y) = \iint_A dx_s dy_s \int_0^l dz_s \int_{-\infty}^{\infty} du\vec{\vec{G}}(x-x_s, y-y_s, u) \cdot \vec{M}\,(x_s, y_s, z_s) =$$
$$\iint_A dx_s dy_s \left(\int_{-\infty}^{\infty} du\vec{\vec{G}}(x-x_s, y-y_s, u) \right) \cdot \left(\int_0^l dz_s \vec{M}\,(x_s, y_s, z_s) \right) =$$
$$l \iint_A dx_s dy_s \left(\vec{\vec{G}}_{2D}(x-x_s, y-y_s) \cdot \langle \vec{M}\,(x_s, y_s) \rangle_{z_s} \right) \quad (7.89)$$

This last equation states that the integral field of the 3D problem corresponds to the solution of the 2D problem with the magnetization averaged over z_s and multiplied by the length on which the magnetization is present.

The derivation we have made depends on the identification of the integral of the 3D kernel along one of its dimensions with the 2D kernel, i.e.,

$$\vec{\vec{G}}_{2D}(x-x_s, y-y_s) = \int_{-\infty}^{\infty} du\vec{\vec{G}}(x-x_s, y-y_s, u) \quad (7.90)$$

This identification is obvious if we think of the 2D problem as the solution of a 3D case, in which the effect of an infinite magnet block is added on any particular point at any cross section.

The present case may be compared to an electromagnet, in which the transport current must return on both ends of the magnet, and will create a different structure with respect to the cross section. In many practical problems, this region is the most difficult to design and have a negative impact on the guided beam. The lack of any coil heads, and the equivalence between the 2D and 3D cases is another strong point of the magnets created with pure permanent magnet blocks.

CHAPTER 8

Materials used in the PMQ

In this chapter we will study the properties of the materials that are used for the manufacturing of the PMQs. The Hallbach design requires just two types of different materials, the permanent magnet blocks and the holders. Losely stated, the magnetic properties of both should be as different as possible, with the permanent magnets being a hard magnetic material and the holders a paramagnetic or diamagnetic material.

The other components of the PMQ are the bolts used to block the magnets and the spacers used to fine-tune their position. These two components have similar requirements than the holders.

8.1 Permanent Magnets

8.1.1 Magnetic properties

In general, a permanent magnet is a material which after the appropriate treatment has magnetization even in the absence of an externally applied magnetic field. Magnetization remains even in the presence of an external magnetic field of opposite direction.The magnetic properties of permanent magnets are summarized in the magnetization graphs given in the second and third quadrants of an H-B plot. In these graphs, it is possible to show in the y-axis both the magnetic induction and $\mu_0 M$. An schematic magnetization plot may be seen in fig. 8.1

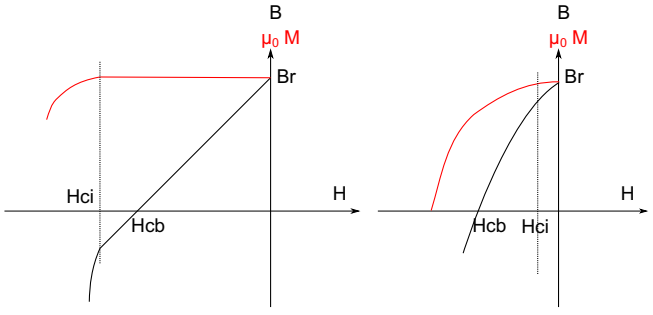

Figure 8.1 – Typical magnetization curves for a hard (left) and a soft magnetic (right) material

Hard permanent magnetic materials are the preferred choice for implementing accelerator magnets. They offer a roughly constant magnetization until the demagnetizing field reaches a critical value H_{ci}, which may well extend beyond the demagnetizing field that causes the

magnetic induction to reverse direction (H_{cb}).On the other hand, soft permanent magnets start to irreversibly lose some of the magnetization as soon as a small demagnetizing field is applied and the actual magnetization of the magnets depend on the history of their manipulation; they may, nevertheless, be useful if they are magnetized in their final configuration and never see a larger demagnetizing field. In practice, there are two basic families of hard permanent magnetic materials, the one based on neodymium-iron-boron (NdFeB) alloys and the one based on samarium-cobalt (SmCo) alloys. Typical values are shown in tab. 8.1

Table 8.1 – Comparative values of several permanent magnet materials

Family	Type	B_r(T)	H_{cb} (kA/m)	H_{ci} (kA/m)	E.Prod. (kJ/m^3)	Max. temp. (^{o}C)
NdFeB	Nd35	1.17-1.21	860 - 899	955	263-279	80
	Nd38	1.22-1.26	876-923	955	287-302	80
	Nd35UH	1.17-1.21	860-907	1990	263-279	180
SmCo	Sm1Co5	0.85-0.90	653-717	1194	127-143	250
	Sm2Co17	1.0-1.1	653-717	1194	183-223	350

NdFeB magnets have a larger remanent field, up to 1.26 T, excellent coercivity and very low permeability, 1.03. In addition they are mechanically tougher than SmCo magnets, and less expensive. Nevertheless, the operating temperature may be higher in Sm2Co17 magnets and the variation of magnetization under irradiation is much smaller; it is mostly because of radiation resistance that Sm2Co17 magnets were chosen for the present application.

8.1.2 Magnetization loss due to radiation

The radiation resistance of permanent magnets has been extensively studied [52], [13], [19], [49]. A long term loss of magnetization is observed in all kinds of magnets, but it is more intense in NdFeB magnets. The main reason for the difference in the behavior of both material seems to be the much better thermal behavior of Sm2Co17. Radiation seems to affect the long term magnetization by a mechanism of local heating, where the temperature increases due to the heat deposited by the impinging particles, briefly exceeding the required to go beyond H_{ci}. This mechanism would imply as well that magnets operating at higher demagnetizing fields would be more prone to degrade over time under radiation. The loss of magnetization due to irradiation is fully reversible, indicating that the degradation of the crystalline structure or material transmutation are of secondary importance when compared to the thermal mechanism.

From the point of view of the PMQ designer, the main guidelines for radiation resistance is the choice of a material with the highest possible H_{ci} at elevated temperatures and trying to minimize the demagnetizing magnetic field in the less favorable permanent magnet block. At the present state of technology, this implies to use Sm2Co17 of high temperature for most accelerator magnets under a significant radiation load.

8.2 Holder materials

The choice of the holder material depends on requirements related to mechanical properties, UHV (Ultra High Vacuum) compatibility and magnetic properties. In this section, we will analyze the requirements and the materials that are valid alternatives for the manufacturing of the holder.

8.2.1 Magnetic properties

The main requirement from the magnetic point of view is to have a magnetic susceptibility as low as possible. The magnetic susceptibility ξ is defined as the magnetization created by a magnetic field on a material,

$$\vec{M} = \xi \vec{H} \tag{8.1}$$

Because the magnets are designed to create the desired magnetic field by using only the magnetization of the permanent magnet blocks, any additional magnetization near the region of interest will create an undesired perturbation of the field. The magnetic susceptibility is related to the relative permeability as,

$$\vec{B} = \mu_0 \left(\vec{H} + \vec{M} \right) = \mu_0 \left(1 + \xi \right) \vec{H} = \mu_0 \mu_r \vec{H} \tag{8.2}$$

And therefore, the magnetic susceptibility is $\mu_r - 1$. According to the value of the magnetic susceptibility, the materials may be classified as,

1. Diamagnetic materials have a negative value of the susceptibility. They react to an external magnetic field by creating a magnetization opposing the imposed field. The absolute value of the susceptibility is normally very low and independent of temperature

2. Paramagnetic materials have a positive, but normally low value of the susceptibility. The susceptibility increases when the temperature is lowered according to the Curie-Weiss law

3. Ferromagnetic materials have a large positive value of the susceptibility. Because of this they have to be avoided in the holder of the PMQ

Because the requirement of low permeability, only diamagnetic and paramagnetic materials may be used for the holder. Almost all alloys based on Aluminum and Copper will show such a behavior. Steels have a particular problematic, at room temperature several phases of steel are meta-stable and may coexist. Austenite is non magnetic, while ferrite is ferromagnetic. The exact amount of austenitic and ferritic phase that may be present at a certain material depends on the chemistry and the treatments applied to the part. A preliminary idea of the behavior of a certain sample may be obtained from the chemical composition by using the Schaeffler or De Long diagrams. This diagram is based on obtaining a Nickel equivalent, which is a weighted average of elements enhancing the austenite production and the Chrome equivalent, a weighted average of elements promoting the formation of ferritic phase.

The determination of the Ni and Cr equivalents is given by eqs. 8.3 and 8.4 , where f_x represents the weight concentration of element x in the steel [36].

$$Ni_{eq} = f_{Ni} + 0.11 f_{Mn} - 0.0086 f_{Mn}^2 + 18.4 f_N + 24.5 f_C \tag{8.3}$$

$$Cr_{eq} = f_{Cr} + 1.21 f_{Mo} + 0.48 f_{Si} \tag{8.4}$$

Once the composition of a stainless steel is known, it is possible to introduce the point of coordinates (Ni_{eq}, Cr_{eq}) in the diagram to check if it is above the line of 0 δ-ferrites. At design stage the chemical composition of the material is not available and the choice of material must be made with the information of the composition range provided by the standards defining the materials. This situation may be seen in fig. 8.2, in which the regions for several austenitic steels have been indicated. For any batch of material, it should be possible to perform a chemical analysis that would provide a point on the Schaeffler diagram. This point should be on the left of the 0% δ-ferrite line for a safe use of the material for the magnet holder.

An important practical aspect is that the AISI standard is more loose than DIN in the chemical composition of the alloy, causing a larger area in the Schaeffler diagram for any given material. In any case, the best recommendation is to perform a chemical analysis of the base material if it is not possible to perform a permeability measurement according to ASTM A 342.

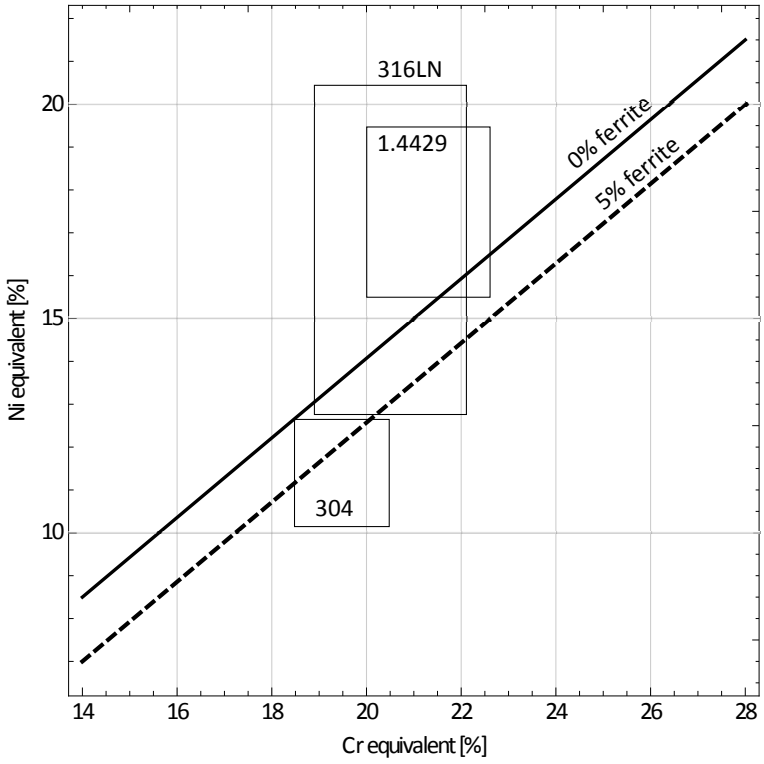

Figure 8.2 – Schaeffler diagram

Very often it is necessary to measure directly the magnetic properties of the low permeability material. In this case, the standard of reference is ASTM A 342, which provides 3 different ways of measuring the material. In the first method, the sample is introduced in the bore of a magnet, while a twin magnet is left with its aperture empty; both magnets are then

powered to a certain level of magnetic field and the flux for both solenoids is compared. The magnet with the feebly magnetic sample inside will have an additional amount of flux that will be due to the magnetization created in the sample. The second method is based on a long sample which enters in the bore of a magnet and whose other extremity is placed totally outside of the magnet, where the field is very low. When the magnet is energized a magnetic force appears that, for positive susceptibility, will tend to introduce the sample in the magnet. The reason to require a long sample is to make the force independent of the details of the fringe field of the magnet, as the force will only depend on the magnetic field in the center of the magnet. The force may be measured with a high resolution balance, that will detect an apparent variation of the weight. The third method is based on comparing the force exercised by a permanent magnet on the sample and on a reference calibration piece of known permeability. This method is very useful for determining the permeability of parts of which it is difficult to extract a sample, as welds.

The relationship between the ferrite content and the material permeability may be clearly seen in fig. 8.3, where the microstructure of a 316L stainless steel is compared to the magnetization of a material as measured in a vibrating sample magnetometer. The material with ferrite inclusions shows a higher magnetization until the ferrite inclusions saturate and then the magnetization increases at the same path that a purely austenitic material. In fig. 8.4, the effect of the paramagnetic magnetization of the austenitic matrix has been eliminated to show only the effect of the ferrite in the global measurement.

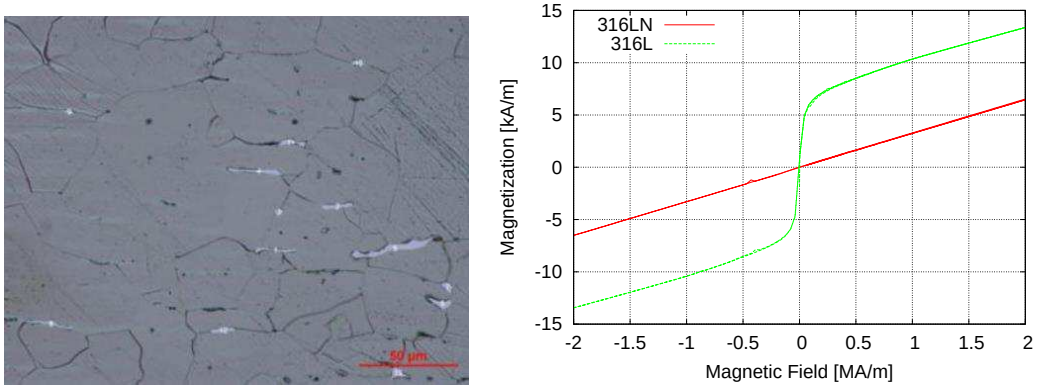

Figure 8.3 – Left, microphotograpy of 316L stainless steel performed by AIMME laboratory for ELYTT. Right, measurement of the magnetization of a sample of this steel compared to a 0% δ-ferrite 316LN material

In [34]it is shown how to calculate the content of ferrite from the magnetization measurement. The ferrite will have a saturation magnetization which is dependent on the composition of the stainless steel and that may be expressed as,

$$\begin{aligned}\mu_0 M_s[T] = 2.16 - 0.0275(\%Cr) - 0.033(\%Ni) - 0.028(\%Mn) - \\ 0.061(\%Si) - 0.026(\%Mo) - 0.067(\%Ti) - 0.063(\%Al)\end{aligned} \tag{8.5}$$

, where the components percentages are given in weight. With this equation, for instance, it is possible to state that the saturation magnetization, $\mu_0 M_s$ of the 316L ferrite is 1.1 T,

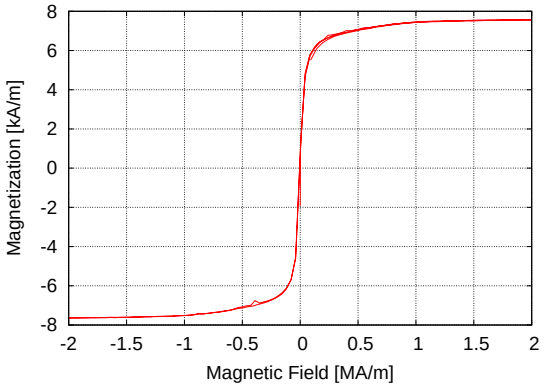

Figure 8.4 – Magnetization of the ferrite phase

and that the ferrite content is around 0.9%.

The final decision for the material of the linac4 was to used AISI316LN stainless steel. This material is almost always totally austenitic, due to the addition of Nitrogen. It is as well tough and the features built on it, like threads, are quite robust. The main problem with this material, apart from its cost, is that it is quite difficult to procure in small quantities. In the project, the material was provided by CERN that has a stock of the material as it can purchase larger amounts of material to be distributed to suppliers that only requires a small amount of it.

8.2.2 Vacuum properties

Because the linac4 magnets will operate in vacuum is important that the production of gas from the materials used in them is as low as possible. This emission of gas is called *outgassing* and it is related to the nature of the material and the cleanliness of its surface.

As in all sciences, the quantification of vacuum should start with the definition of the appropriate extensive magnitude. The ideal one for this science should be the number of moles on a given volume. However, this magnitude cannot be directly measured, and vacuum scientists use a proxy of it, the product of the pressure by the volume.

$$Q = PV \tag{8.6}$$

Of course, both magnitudes are related by the ideal gas law as,

$$n = \frac{Q}{RT} \tag{8.7}$$

So that in many cases both magnitudes are directly related. We should take into account that when temperature changes Q may change although the number of particles in the volume has not varied. This is, for instance, the case in the insulating vacuum of cryostats, in which Q decreases several orders of magnitude when the temperature of the cold walls is reduced. The large decrease of the pressure is due partially to the freezing of some particles on the cold walls (cryosorption) and to the reduction of the temperature of the gas.

Q is normally measured in mbar·l, or in more modern texts in $\mathrm{Pa} \cdot \mathrm{m}^3$.

The outgassing is defined as the amount of Q released by the material by unit of time. A proper outgassing requires careful cleaning, and if a very low rate is desired to termically activate the surfaces under vacuum before operation, the so called *bake-out*. In such a way, the interstitial impurities will migrate towards the surface and will be pumped away. Nevertheless, the complete PMQ cannot be baked due to the presence of the magnets which would demagnetize if the temperature is significantly increased.

The measurement of the outgassing requires to pump the magnet inside a vacuum vessel to a low enough pressure and, once the pumping stopped and the pump isolated from the vessel, to measure the increase of pressure over time. Often, it is necessary to correct for the outgassing of the vessel itself and for any possible leak from the outside of the vessel.

The PMQs must be cleaned in an ultrasonic bath using an appropriate detergent and then rinsed with de-ionized water and dried in a flow of clean air. To avoid any demagnetization of the permanent magnet blocks, the temperature of the air flow cannot be too high.

For linac4, the cleaning and vacuum measurement was performed by CERN. The process was successful, indicating that the choice of material and their handling was adequate.

CHAPTER 9

Design of the linac4 PMQ

The previous chapters are a preparation for the following ones. We have seen how a DTL accelerating structure works, why it requires a transverse focusing and how this may achieved with permanent magnet based structures. We have as well learn which materials and which topologies may be used for generating the required magnetic fields. With this basis, it is now time to go to the practical problem of designing, building and measuring a set of permanent quadrupoles that will be used for a real accelerator. In this case, the second and third tanks of the linac4 DTL at CERN.

In this chapter, we present the specifications as received by CERN and we design a family of PMQ that in the most economical and simple way satisfies these requirements. As we will see, this is obtained by using the most simple possible structure, an 8 block Hallbach array with square permanent magnet blocks.

9.1 Specification of the linac4 DTL PMQ

Table 9.1 shows the specifications given by CERN for the requirements of linac4 PMQ. These PMQs correspond to the later tanks of LINAC4, while the first tank was equipped with PMQs supplied by ASTER, a characterization of these magnets may be seen in [17]. The description of the DTL where the PMQ is to be integrated may be seen in [44] and [45].

Table 9.1 – Specifications of the linac4 PMQ

Number of pieces	70
Integrated gradient (Max)	2.0 Tesla
Integrated gradient (min)	1.2 Tesla
Mechanical Length	80 mm
Inner diameter	22 mm
Outer diameter	60 mm
Gradient integral error (rms)	± 0.5 %
Magnetic versus geometric axis	less than 0.1 mm
Maximum Harmonic content at 7.5 mm radius Bn/B2 for n=3,4,...10	0.01
Maximum Yaw/pitch	2 mrad
Maximum Roll	1 mrad
Machining tolerances ISO 2768-mK unless indicated in SPLACDTD00009	
Outgassing rate per magnet below 4.10^{-6} mbar l/ s^{-1}	

The roll specification refers to a rotation of an ideal quadrupole with respect to the beam

axis, the yaw is the rotation with respect to an horizontal axis perpendicular to the beam axis, and the pitch is the rotation with respect to a vertical axis.

Tab. 9.2 shows the specified strengths of the 70 PMQs that will be used for the tanks 2 and 3 of linac4. All the magnets have a length of 80 mm and an aperture of 22 mm. The minimum integrated gradient is 1.197 T and the maximum 2.031 T.

Table 9.2 – Specifications of the PMQs of the tanks 2 and 3 of linac4

Quad Name	**Length (m)**	**Grad (T/m)**	**Aperture radius (mm)**	**Abs Integrated Gradient (T) objective**
L4D.MQDP.0231	0.08	30.5367	11	2.031136
L4D.MQFP.0232	0.08	-23.3395	11	1.762152
L4D.MQFP.0233	0.08	-23.3395	11	1.762152
L4D.MQDP.0234	0.08	22.8865	11	1.74418
L4D.MQDP.0235	0.08	22.8865	11	1.74418
L4D.MQFP.0236	0.08	-21.4261	11	1.702012
L4D.MQFP.0237	0.08	-21.4261	11	1.702012
L4D.MQDP.0238	0.08	21.2464	11	1.690856
L4D.MQDP.0239	0.08	21.2464	11	1.690856
L4D.MQFP.0240	0.08	-20.6972	11	1.656788
L4D.MQFP.0241	0.08	-20.6972	11	1.656788
L4D.MQDP.0242	0.08	20.562	11	1.646004
L4D.MQDP.0243	0.08	20.562	11	1.646004
L4D.MQFP.0244	0.08	-20.1512	11	1.613084
L4D.MQFP.0245	0.08	-20.1512	11	1.613084
L4D.MQDP.0246	0.08	20.0204	11	1.602596
L4D.MQDP.0247	0.08	20.0204	11	1.602596
L4D.MQFP.0248	0.08	-19.6233	11	1.570652
L4D.MQFP.0249	0.08	-19.6233	11	1.570652
L4D.MQDP.0250	0.08	19.4965	11	1.560476
L4D.MQDP.0251	0.08	19.4965	11	1.560476
L4D.MQFP.0252	0.08	-19.1115	11	1.52948
L4D.MQDP.0253	0.08	-19.1115	11	1.52948
L4D.MQDP.0254	0.08	18.9879	11	1.519548
L4D.MQDP.0255	0.08	18.9879	11	1.519548
L4D.MQFP.0256	0.08	-18.6122	11	1.489324
L4D.MQFP.0257	0.08	-18.6122	11	1.489324
L4D.MQDP.0258	0.08	18.4915	11	1.479608
L4D.MQDP.0259	0.08	18.4915	11	1.479608
L4D.MQFP.0260	0.08	-18.1242	11	1.450012
L4D.MQFP.0261	0.08	-18.1242	11	1.450012
L4D.MQDP.0262	0.08	18.0378	11	1.440476
L4D.MQDP.0263	0.08	18.0057	11	1.440476

Quad Name	Length (m)	Grad (T/m)	Aperture radius (mm)	Abs Integrated Gradient (T) objective
L4D.MQFP.0264	0.08	18.0057	11	1.411444
L4D.MQFP.0265	0.08	-17.9209	11	1.411444
L4D.MQDP.0266	0.08	-17.9209	11	1.405008
L4D.MQDP.0267	0.08	17.7212	11	1.405008
L4D.MQFP.0268	0.08	17.7212	11	1.38432
L4D.MQFP.0269	0.08	-17.6454	11	1.38432
L4D.MQDP.0270	0.08	-17.6454	11	1.3798
L4D.MQDP.0271	0.08	17.1262	11	1.3798
L4D.MQDP.0331	0.08	17.1262	11	1.346284
L4D.MQDP.0332	0.08	-16.6297	11	1.346284
L4D.MQFP.0333	0.08	-16.6297	11	1.340516
L4D.MQFP.0334	0.08	16.5425	11	1.340516
L4D.MQDP.0335	0.08	16.5425	11	1.334468
L4D.MQDP.0336	0.08	-16.278	11	1.334468
L4D.MQFP.0337	0.08	-16.278	11	1.316076
L4D.MQFP.0338	0.08	16.1952	11	1.316076
L4D.MQDP.0339	0.08	16.1952	11	1.309348
L4D.MQDP.0340	0.08	15.9611	11	1.309348
L4D.MQFP.0341	0.08	-15.9443	11	1.288936
L4D.MQFP.0342	0.08	-15.9443	11	1.288936
L4D.MQDP.0343	0.08	15.8627	11	1.282296
L4D.MQDP.0344	0.08	15.8627	11	1.282296
L4D.MQFP.0345	0.08	15.8586	11	1.262176
L4D.MQFP.0346	0.08	-15.6152	11	1.262176
L4D.MQDP.0347	0.08	-15.6152	11	1.255604
L4D.MQDP.0348	0.08	15.5387	11	1.255604
L4D.MQFP.0349	0.08	15.5387	11	1.235708
L4D.MQFP.0350	0.08	-15.3066	11	1.235708
L4D.MQDP.0351	0.08	-15.3066	11	1.22918
L4D.MQDP.0352	0.08	15.2298	11	1.22918
L4D.MQFP.0353	0.08	15.2298	11	1.20936
L4D.MQFP.0354	0.08	-14.9971	11	1.20936
L4D.MQDP.0355	0.08	-14.9971	11	1.218028
L4D.MQDP.0356	0.08	14.9301	11	1.218028
L4D.MQFP.0357	0.08	14.9301	11	1.197136
L4D.MQFP.0358	0.08	14.7753	11	1.197136
L4D.MQDP.0359	0.08	-14.7273	11	1.460736

The sign of the gradient indicates whether the magnet will be used in focusing or defocusing configuration. CERN planned to have all the magnets built with the same configuration and then to use them in one or the other configuration by the choice of the locating pin on the outer radius of the holder. Due to a wrong interpretation of the drawings, we built the

quadrupoles with the polarity already implemented in them, so that all magnets have to be installed in the drift tubes in the same angular position. This error was more an additional difficulty in the construction of the quadrupoles than a problem for the user, as each magnet was already labelled for their final position.

9.2 Choice of the magnet structure

The main objective of the design is providing the most cost effective solution to the PMQ satisfying all the requirements with a large confidence.

In general, the 16 block structure is preferred over the 8 block structure because it can provide a higher magnetic field, lower harmonics and lower stray field outside of the magnet. Nevertheless, it is more complex because it requires magnets polarized along the diagonal, which reduces the possibilities of sorting and complicates the manufacturing. In addition, magnetizing along the diagonal is slightly more complicated that along the sides of a rectangle.

As for the shape of the magnets, sector magnets are optimal for providing a high gradient as they may fill most of the space with permanent magnet material. They are nevertheless, more difficult to manufacture and magnetize. They are, as well, more difficult to shim than square or rectangular magnets, as they have to be displaced radially by putting to equal shims on the tapered sides of the permanent magnet blocks. In addition, the material on the wide side of the wedge is less efficient in generating magnetic field due to the large dependence on the radius of the field created by a magnetic moment. Therefore, sector magnets should be used when the main requirement is higher gradient.

Rectangular magnets are at an intermediate position with respect to sector and square magnets. They are easier to build, magnetize and shim than square magnets, but nevertheless, at least two different types of magnetizations are required. In addition, for the magnets magnetized along the short side of the square, the coercitive field is higher than for square blocks. Numerical simulations as shown in [24] show that rectangular magnets are less sensitive than sector magnets to the angular error of the magnetization.

Square magnets are the simplest possible building elements. Only one type of magnetization is required and they can be easily and accurately shimmed on one flat surface. It has the highest possibility of sorting blocks and the coercitive field is low.

Therefore, the 8 square block PMQ is the solution that must be chosen if it satisfies in the available volume, the requirements of gradient, field quality and stray field. In the following section, we will prove that it is possible to find a solution of this type that fulfills all the requirements.

The main drawback of the 8-block solution is the presence of a nominal b_{10}, which does not exist in the 16-block one. Nevertheless, this is a minor problem, as the value of b_{10} is well bellow the acceptable one, and being a high order harmonic is more related to the design itself than to the manufacturing errors.

9.3 Choice of the permanent magnet block size

From the point of view of manufacturing, the simplest design uses only 8 blocks of square magnets, magnetized along the side. In addition, we are interested, if possible, in having only

one type of permanent magnet block for the whole range of series. In the present section, we will prove that such a choice of permanent magnet size exists for the list of gradients of linac4 tanks 3 and 4.

The first constraint is the aperture of the PMQ, that we know is 11 mm. Because the simplest design uses a radially inner wall of the holder to position the magnet, we are constraint by the minimum radial position of the magnet. In order to have a rigid enough wall and to minimize the risks of manufacturing the holder, we have fixed a minimum wall thickness of 2 mm; defining a minimum radial position of the permanent magnet block of 14 mm.

In addition, we require that the radially outermost position of the magnet is limited by the need to have the pushing grub bolts large enough. The minimum possible length of the grub bolts is 4 mm, and therefore the magnet cannot extend radially beyond 26 mm. The outermost radial position of the magnets will be then 26 mm minus the height of the magnet, with this constraints and eq. 7.77, we can draw fig. 9.1.

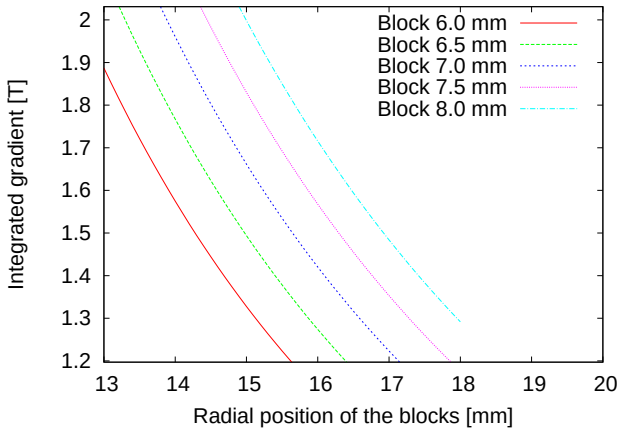

Figure 9.1 – Integrated gradient for several block sizes and radial positions of the blocks

In fig. 9.1 it may be seen that blocks smaller that 6.5 mm cannot reach the maximum gradient because they should be placed in a radial position incompatible with the minimum wall thickness in the innermost radius. In addition, magnets larger than 7.5 mm should be incompatible with the minimum length of the grub bolt while trying to obtain the smallest integrated gradient. Therefore, the range of square magnet blocks is limited in size to the range 6.5 mm to 7.5 mm.

The reason why 7.5 mm has been finally chosen may be seen in fig. 9.2.The magnets blocks in the lower range of the dimension have a nominal value of b_{10}, the first allowed harmonic for ideal magnets, which is significantly larger than the larger ones. This is due to the fact that the smaller magnets leave a large angular dimension of the aperture *uncovered*, and therefore cause a local field reduction in this area. This is the cause of the appearance of a higher value of b_{10}. With the chosen design, the maximum built-in value of b_{10} is 25 units approximately, which satisfies the specified field quality.

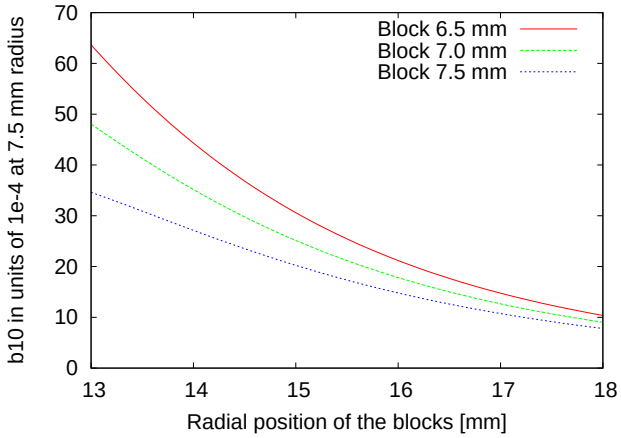

Figure 9.2 – b10 for several block sizes

9.4 Analysis with a finite element program

The analytical analysis described in the previous section was extremely useful in the initial stages of the design to perform the general dimensioning of the PMQ.It is very practical for choosing between 8 and 16 blocks designs and to sweep a family of designs with slightly different geometries. Nevertheless, it has some limitations, the most important one being the assumption of the relative permeability being one. As the magnets will work under their own demagnetizing field, the actual magnetization will not be exactly B_r/μ_0 . Even more important, the magnetic field varies from magnet to magnet and inside each magnet, creating a non-homogeneous magnetization that translates into some harmonics appearing, the most important b_6. In addition, the permanent magnets are not exactly rectangles, but their geometry may include other features such as fillets or a certain taper. Taking these effects into account, several finite element method (FEM) models were developed, both in 2D and 3D, which were used to confirm the analytical results and to model the additional effects mentioned above. 3D models were created to include end-effects that may affect performance. Fig. 9.3 shows the harmonics calculated with the FEM model.

The results of the higher order harmonics seem to be affected by numerical noise, but a trend may be observed with a value of b_6 going from 4 units at the higher gradients to 2 units at the lower integrated gradients; b_{10} has a more or less constant value of -1 unit.

Another very important piece of information obtained from the FEM analysis is the demagnetizing force applied to the material. For all the designs, the magnetic field was plotted in the direction of the magnetization, and then it was checked that the maximum allowed value was not exceeded at any point of the structure. We can see in fig. 9.4 a plot of the chose design in the less favorable position, i.e. with the PMQ with the highest integrated gradient. The peak value of H is 574 kA/m, well below the value of H_{ci}. An average value of H in the blocks is -370 kA/m.

It is interesting to note that to reproduce in the analytical calculations the values given by the finite element calculations, the apparent residual field B_r should be reduced according to the finite susceptibility of the material,

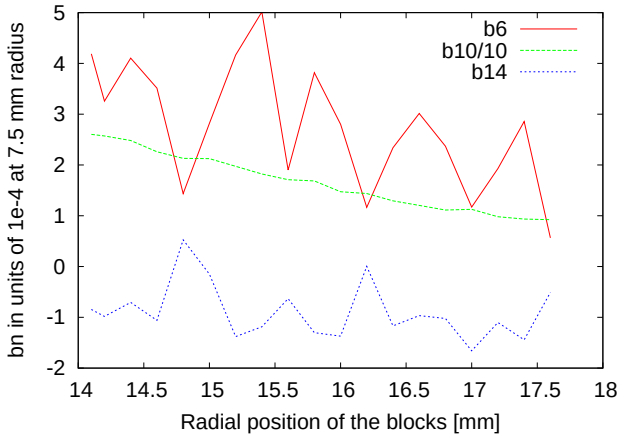

Figure 9.3 – Harmonics for the nominal design according to the FEM calculation

$$B_r' = B_r + \psi H = B_r + \mu_0 \left(\mu_r - 1\right) H \tag{9.1}$$

Using this equation and the values of the Sm2Co17, we obtain that we must use a value of 1.03 T for B_r in the analytical calculations instead of 1.06 T. This is the value used for instance in fig. 9.1 to obtain the integrated gradient for several block sizes and radial positions. On the other hand, we can observe in fig. 9.4 that the tangential block operates under a higher H that the radial block. The combination of this difference of magnetic field plus the finite susceptibility of the material creates the b_6, that is not existent in a PMQ of 8 blocks operating with blocks of uniform magnetization, see eq. 7.82.

9.5 Sensitivity of the magnetic field to the holder material

As it was mentioned previously, the holder and shim material should have a susceptibility as low as possible in order not to influence the magnetic field created by the permanent magnet blocks. Paramagnetic or diamagnetic metals would be an ideal choice, but previous experience had shown vacuum problems in the case of Aluminum, and Copper alloys were not considered.

To check for the effect of a slightly magnetic holder material, a FEM model that included the holder was created and the relative permeability of the material was varied from 1 to 2 and the integrated gradient and harmonic content was calculated, fig. 9.5. It is interesting to note that the effect of the relative permeability of the holder on the integrated gradient is very non-linear, with a small effect of values of relative permeability below 1.1. On the other hand, the effect on b_6 may be noticed even at low values of relative permeability. This results indicate that permeabilities around 1.05 or below are fully acceptable for the present design. This value can be easily obtained with a highly austenitic alloy as AISI 316LN, but it may be not achieved in lower grade steels.

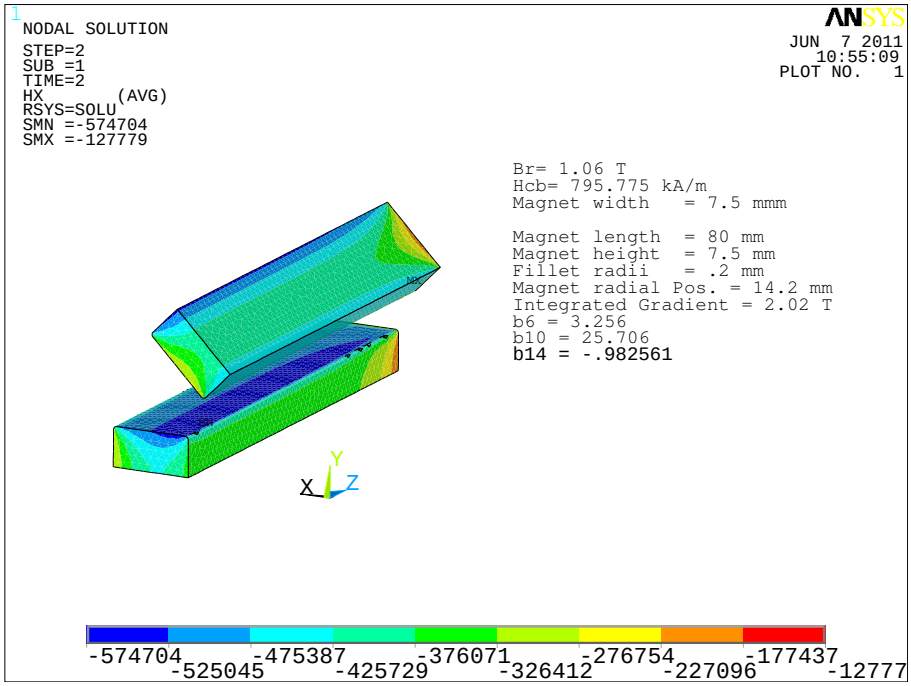

Figure 9.4 – Coercitive field H in the permanent magnet blocks assembled in the PMQ

9.6 Magnet engineering

The general design of the magnet may be seen in 9.6. It is based on a cylindrical AISI316LN holder which has been machined by wire erosion in order to have 8 slots for the insertion of the 8 permanent block prisms. Below the permanent magnet blocks, non magnetic stainless steel shims are placed in order to adjust the integrated gradient. The size of the slots have been designed to cover the whole range of the desired integrated gradient with just one holder design. Each magnet is blocked in position by two grub bolts distributed along the magnet length.

The magnet is centered in the drift tube by the external cylindrical shape and the angle defined by two small locating pins located at 90°. The two pin holes allow for installing the magnet as a QF or a QD depending on the relative angular position of the magnet with respect to the drift tube.

The pin holes must go through the thickness of the wall in order to avoid trapping a volume of gas at the bottom of the hole. The hole is made in two steps, with a reduction of diameter in order to support the pin in position. This design of the pin hole allows to pump the volume below the pin through the magnet slot.

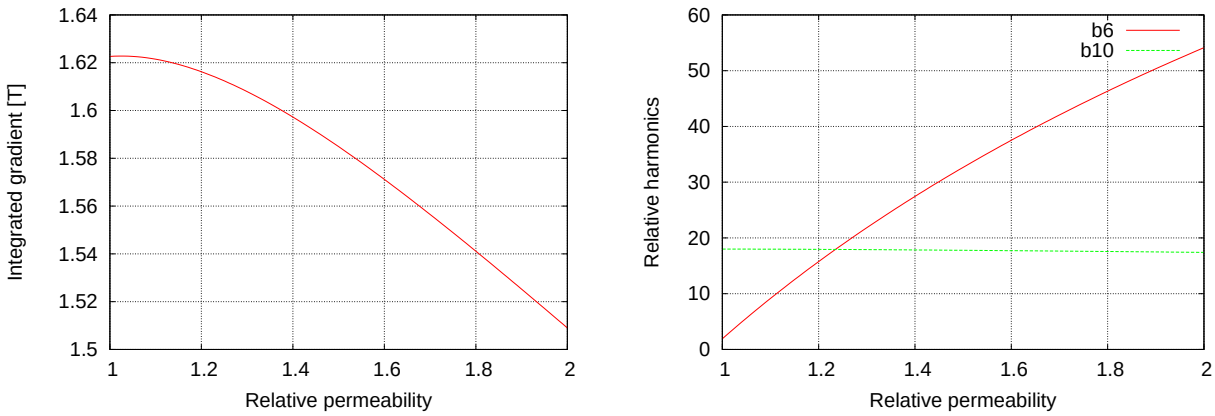

Figure 9.5 – Change of the integrated gradient and the harmonic content with respect to the holder relative permeability

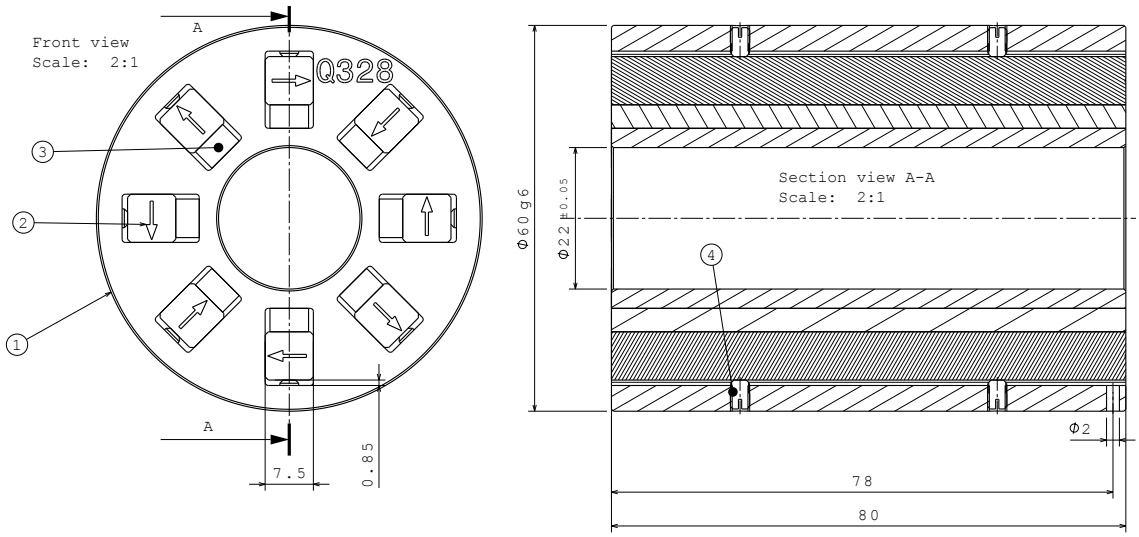

Figure 9.6 – Engineering drawing of the magnet. (1) Holder, (2) Permanent magnet blocks, (3) shims, (4) Grub bolts.

CHAPTER 10

Measurement of the permanent magnet blocks

A normal permanent magnet supplier, whose business is normally centered in permanent magnets for motors, actuators and other applications which do not require a highly accurate magnetic field, will provide a batch of magnets with a certain amount of imperfections that make them not directly useful in the permanent magnet assemblies of accelerator quality. These imperfections may be of several types:

1. Geometrical imperfections. In this case, the size or shape of the permanent magnet blocks are not accurate enough for the application. Usually, this problem is easily detected, at least for prismatic blocks, and the magnets are rejected at the factory

2. Magnetization value error. The level of the magnetization may vary between the different blocks of the batch. In general, the same PMQ must be assembled with blocks of the same magnetization in order to avoid magnetic field errors in the assembly. In order to use the low quality blocks in the high quality assemblies, it is necessary to measure the whole batch of blocks and carefully choose the appropriate blocks that may be combined together

3. Magnetization angle error. The permanent magnet suppliers cannot provide in general a magnetization angle accuracy better than 1°. This creates a problem because this error translates directly into a roll of the integrated magnetic field. As the typical tolerance of the roll of a PMQ is 1 mrad, it is necessary to compensate this error in the final assembly. This problem requires as well a careful measurement of the blocks to guide in the cancellation process

10.1 Measurement method of the permanent magnet blocks using a Hall probe scan

Because the most tight requirements involve the lower order harmonics of the integrated field, magnetic center given by the first harmonics, integrated gradient given by the normal second harmonic and roll given by the skew second harmonic; we are mostly interested on the average magnetization of the magnet and not in the details of the spatial distribution of any magnetization inhomogeinity. Such a magnetization gradient will be mostly expressed

in a higher order harmonic. Therefore, we have adopted a model of the permanent block as homogeneously magnetized but including a roll angle in the direction of the magnetization.

The estimation of the magnet magnetization is made in several steps:

1. First a finite element model of the magnet is made. This model is run twice, in the first run a unitary magnetization in the nominal direction is imposed in the permanent magnet block model and the magnetic field is calculated in the air regions around the block. In the second run, the magnetization is imposed in the direction perpendicular to the nominal and the problem is solved again.

2. The magnetic field around the magnet is measured by a Hall probe in a certain cloud of points including all three components of the magnetic field.

3. A minimum square optimization procedure is used to obtain the optimal nominal and skew magnetization that better match the measured values of the magnetic field with the values obtained in the finite element simulation.

10.1.1 The finite element model of the permanent magnet block

ANSYS^{TM}was used for modeling the permanent magnet blocks using finite elements. A 3D FEM model of the block was created and a B_r of 1 T was imposed to the material of the magnet. The problem was run twice, the first time with the magnetization in vertical direction (as it was going to be measured in the second phase) and the second time with the magnetization in the horizontal direction. For each of the runs, the vector value of the magnetic field was calculated on a cloud of 66 points on which the actual magnets were to be measured afterwards. The solutions of the field at these locations, provide the coefficients k_{ij} to be used in §10.1.3. Each of the coefficients represent the capability of a uniform magnetization on the block to create magnetic field at a certain point and direction.

10.1.2 Magnetic measurement of the permanent magnet blocks

Each block was measured twice, the first time with the north pole upwards and the second point with the south pole upwards. For every measurement, the field is obtained at 66 points, on a cloud of 11x3x2 with respect to the block length, width and height respectively. Because the used Hall probe is vector, in total 66x2x3 = 396 individual numbers are obtained to fit the only 2 parameters modeling the magnet block. The measurements along the length of the magnets extend 10 mm on each side to capture any effect of the stray field.

Fig. 10.1 shows the experimental set up used for the magnetic measurements of the blocks.

The measurement has been performed by using a vector Hall probe, Metrolab THM-1176. This Hall probe can measure the three components of the magnetic field at a given point. The Hall probe is attached to the arm of an aluminum body CNC machine. In order to accurately position the center of the Hall probe with respect to the permanent magnet block, a reference plate has been built on which the permanent magnet block is position and three reference pin holes are accurately referenced to the block slot. In each of these pin holes a reference magnet is located. The reference magnet, fig. 10.2 is built so as to have a very well defined point of

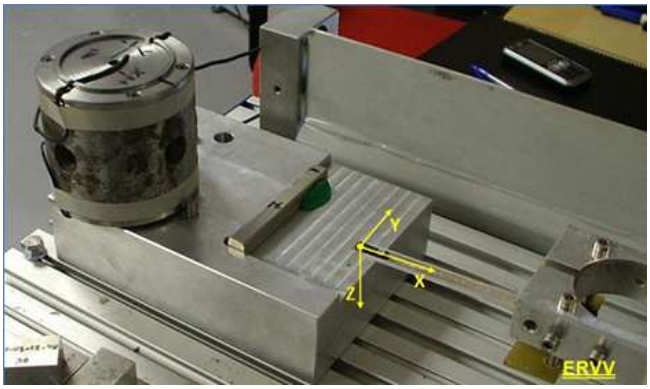

Figure 10.1 – Measurement of an individual permanent magnet block

zero magnetic field. This is obtained by powering the two coils of the reference magnet by current of opposite polarity obtaining by symmetry a point of zero field.

The reference magnet is located alternatively on the three pinholes. The first pinhole defines the origin of the reference systems, the line linking the first and second points defines the x-axis and the three points define the x-y plane. The z-axis is defined to be perpendicular to the x-y plane and form a destrogirus coordinate system. After locating the three points of zero field in space, the program controlling the CNC calculates a matrix transformation to convert the coordinates from the newly defined system, the bench system, to the CNC system. Because the pin holes have very accurate positions with respect to the magnet, it is possible now to measure the field on a given point with respect to the magnet block.

In addition, it is possible using the reference magnet to correct the rotation of the Hall probe with respect to the bench system. This is made taking advantage of the fact that the reference magnet is axisymmetric with respect to the bench z-axis. For an axisymmetric magnetic field, the field is purely radial in the central plane (the plane with 0 field component in the z-axis), in this case any movement of the Hall probe in the radial plane from the zero field point to a new point n the plane should only create a field component in the direction of the movement. In the same way, a movement in the direction of the z-axis, should only create a component of the B field in the z axis. If we perform three movements from the zero point field in the direction of the three coordinate axes in the bench system, we would measure three B fields which in the Hall probe reference system have all the components different from zero. As we know that each of the readings should only provide a non zero measurement in the direction of the displacement, we may calculate a rotation matrix that transforms the Hall probe system to the bench system.

In a more quantitative way, the 9 scalar readings may be summarized in a matrix of type,

$$\mathbf{M} = \begin{bmatrix} B_{xx} & B_{xy} & B_{xz} \\ B_{yx} & B_{yy} & B_{yz} \\ B_{zx} & B_{zy} & B_{zz} \end{bmatrix} \tag{10.1}$$

, where B_{xy} means the reading on the x-axis of the Hall probe when it is displaced in the y-axis. The transformation matrix must them be capable of converting the matrix of read outs $\mathbf{M}$ to a diagonal matrix.

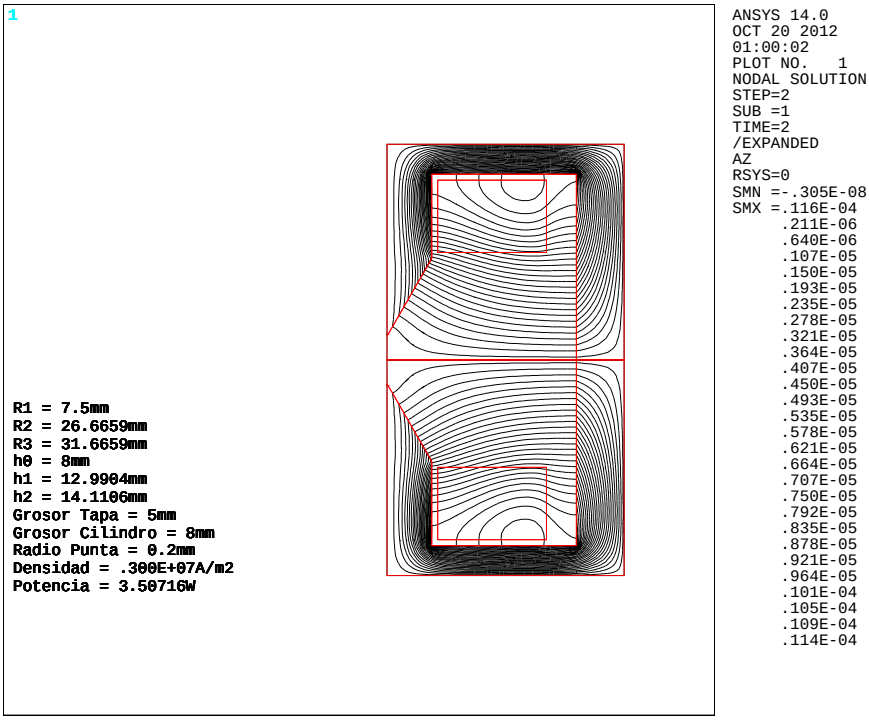

Figure 10.2 – Finite element model of the conical magnet. It is an axisymmetric model.

$$\mathbf{SM} = \mathbf{D} \tag{10.2}$$

The conversion matrix $\mathbf{S}$ must have the shape,

$$\mathbf{S} = \begin{bmatrix} \cos\alpha_1 & \sin\alpha_2 \sin\beta_2 & \sin\alpha_3 \cos\beta_3 \\ \sin\alpha_1 \cos\beta_1 & \cos\alpha_2 & \sin\alpha_3 \sin\beta_3 \\ \sin\alpha_1 \sin\beta_1 & \sin\alpha_2 \cos\beta_2 & \cos\alpha_3 \end{bmatrix} \tag{10.3}$$

, in which each column is a vector in the bench system pointing in the direction of one of the Hall probe sensors. The problem has 6 degrees of freedom, two per each Hall probe sensor corresponding to its direction in the bench system.

10.1.3 Fitting of the measurements to the model

In this section it is explained how the measurements are fitted to the permanent magnet block model, that as mentioned earlier, corresponds to an homogeneous magnetization with a normal component M_z and a skew component M_x, transverse to the permanent magnet block.

The finite element model has provided a series of coefficients k_{zx_i} and k_{zz_i} which provide the z component of the field at the point i when multiplied by the normal magnetization M_z and the skew one M_x, respectively.

$$B_{z_i} = k_{zx_i} M_x + k_{zz_i} M_z \tag{10.4}$$

Because the magnet is not ideal, we will use a minimum square fitting of the measurements of the magnetic field with the homogeneous magnetization values, i.e. we must find the minimum of the function,

$$f\left(M_x, M_z\right) = \sum_i \left(B_{z_i} - k_{zx_i} M_x - k_{zz_i} M_z\right)^2 \tag{10.5}$$

This function may be minimized by the standard method of taking the partial derivatives with respect to M_x and M_z and equating them to zero. The following system of two equations with two unknowns is obtained,

$$\sum_i k_{zx_i}^2 M_x + \sum_i k_{zz_i} k_{zx_i} M_z = \sum B_{z_i} k_{zx_i} \tag{10.6}$$

$$\sum_i k_{zz_i} k_{zx_i} M_x + \sum_i k_{zz_i}^2 M_z = \sum B_{z_i} k_{zz_i} \tag{10.7}$$

This pair of equations, provides us with the best fitting of the normal and the skew magnetization of the permanent magnet blocks, which are the main parameters used in the sorting to assign a certain set of blocks to a given PMQ.

The minimum square fitting is made independently on the north and south pole of each block and then the results are averaged.

10.2 Measurement of the permanent magnet blocks by use of an external coil

A different method of determining the total magnetization of a permanent magnet block is to introduce the block inside a coil and measure the flux variation created by the insertion of the magnet. To study how the method works, let us see the effect of a magnetic dipole $\vec{m}$ located at point $\vec{r'}$ on a coil located at $r(\vec{s})$, where s is the length along the coil. The flux created by the magnetic dipole on the coil is just the integral of the vector potential along the coil,

$$\lambda = \oint \vec{A} \cdot d\vec{r}(s) = \oint \frac{\mu_0}{4\pi} \frac{\vec{m} \times \left(\vec{r}(s) - \vec{r'}\right)}{|r(\vec{s}) - \vec{r'}|^2} \cdot d\vec{r}(s) = -\frac{\mu_0}{4\pi} \vec{m} \cdot \oint \frac{d\vec{r}(s) \times \left(\vec{r}(s) - \vec{r'}\right)}{|r(\vec{s}) - \vec{r'}|^2} \tag{10.8}$$

Where we have made a cyclic permutation of the triple vector product. Obviously, the flux will be measured by attaching a voltmeter to the terminals of the coil and integrating over time the voltage while the permanent magnet block moves from a position with zero flux linkage to the final position.

$$\lambda = -\int v(t)\, dt \tag{10.9}$$

We can compare eq. 10.8 with the one giving the magnetic induction caused by a current I circulating through the coil at $\vec{r'}$, using the Biot-Savart law,

$$\vec{B} = \frac{\mu_0}{4\pi} \oint \frac{I d\vec{r}(s) \times \left(\vec{r(s)} - \vec{r'}\right)}{|\vec{r(s)} - \vec{r'}|^2} \tag{10.10}$$

We see that the part in the integral is the same, and that we may write the flux created by the magnetization in the coils as,

$$\lambda = -\left(\frac{\vec{B}}{I}\right) \cdot \vec{m} \tag{10.11}$$

We must consider that in eq. 10.11, neither $\vec{B}$ nor I do actually exist, but the whole parenthesis just represent the magnetic induction that would be created at the point of the magnetic moment by a unitary current traversing the coil.

Because of the superposition principle, the effect of the complete permanent magnet block in the coil may be obtained by volume integration of the effect of the individual magnetization $d\vec{m} = \vec{M} dV'$.

$$\lambda = -\iiint \left(\frac{\vec{B}}{I}\right) \cdot \vec{M}\, dV \tag{10.12}$$

In order to obtain the total magnetization of the block we must use a coil that would create an homogeneous magnetic field in the region where the block will finish its *flux creating path*. This can be clearly seen by getting the magnetic field out of the integral of eq. 10.12. If on the other hand we would like to measure the north-south difference of a magnet we should place the magnet in a coil that would create a gradient field with the plane of zero field at the center of the permanent magnet block. One extreme application would be to introduce the magnet in a structure capable of generating an arbitrary field profile, like a set of nested multipolar coils each of them equipped with an independent voltage integrator, in this case, it would be possible to make a *tomography* of the magnet magnetization.

An interesting special case, is when a Helmholtz coil is used to measure the magnetization of the magnet. In this case, a pair of two small cross section coils, whose radius is equal to their separation is used either to create a nearly uniform field in a small region of space or to measure the total magnetization of the magnet. The field created near the origin by a Helmholtz coil is,

$$B = \left(\frac{4}{5}\right)^{3/2} \frac{\mu_0 n I}{R} \tag{10.13}$$

, where n is the number of turns on each coil.

In this case, the flux in the Helmholtz coil created by a magnetic dipole $\vec{m}$ aligned along the magnetic field of the Helmholtz coil will be,

$$\lambda = \left(\frac{4}{5}\right)^{3/2} \frac{\mu_0 n m}{R} \approx \left(\frac{4}{5}\right)^{3/2} \frac{\mu_0 n M V}{R} \tag{10.14}$$

One important point to compare the results of the measurements using both methods is

that the magnetic flux method gives the actual magnetization of the block, including the loss of magnetization due to the susceptibility of the permanent magnet material. On the other hand, the method using the Hall probe and the minimum square fitting to the finite element model will provide B_r, the remanence.Only in materials with a relative permeability of near 1, or when the geometry of the magnet makes it operate at very low demagnetizing field, will both methods give the same value. From the sorting point of view, this difference is unimportant, because we are comparing blocks of the same material and geometry; but when using the obtained values of magnetization to define the shimming of the PMQ it must be taken into account, because the result of the flux coil will apparently give a lower value of B_r.

The effect of the non-zero magnetic susceptibility is very clear in magnets whose imposed magnetization is not aligned with a symmetry axis of the magnet. In this case, the reversible magnetization will not be aligned with the imposed one, and the total magnetization will be rotated with respect to the desired one. A pair of orthogonal Helmholtz coils, will then measure a magnetization rotated with respect to the desired angle. This is typical of the permanent magnet quadrupoles using 16 blocks, of which some of them are at 45°with respect to the symmetry angle of the blocks. This effect is clearly shown in fig 10.3. The imposed magnetization is decomposed on to orthogonal axes parallel to the magnet faces. The demagnetizing field along the short side of the magnet is larger than along the long side, this causes that the total demagnetization has a larger component along the short side and the total magnetization is rotated towards the long axis of the magnet. This effect is measured by the two pairs of orthogonal Helmholtz coils and may be considered as an error of the magnetization, but it is just a consequence of the non-zero magnetic susceptibility of the magnet.

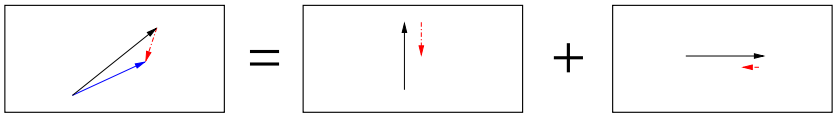

Figure 10.3 – Effect of the imposed magnetization not being aligned to a symmetry axis of the permanent magnet block. The imposed magnetization is drawn on black, the reversible demagnetization is drawn on red and the total one on blue.

.

10.3 Statistical analysis of the magnet blocks

The magnets for linac4 were produced, including magnetization, by the Spanish company IMA (http://www.ima.es). As it will be shown afterwards, the quality of the magnets was good, in spite of the normal application of its permanent magnets being industrial instead of scientific.

All the magnets were measured using the method of the Hall probe. The statistical distribution of the magnets is of the utmost importance, as the difficulty on sorting the permanent magnet blocks will depend on how disperse its distribution is. Fig. 10.4 shows the histogram of the residual magnetization, as measured and adjusted according to the method of the previous section. The distribution of magnetization follows well a normal distribution of average 1.071 T and standard deviation 0.0075.

Fig. 10.5 shows the distribution of the angular error. The general distribution and a more

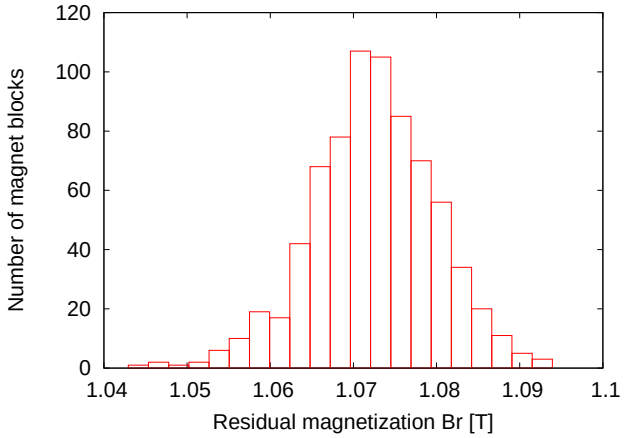

Figure 10.4 – Histogram of the residual magnetization

detailed histogram around the region of small angular errors, the only one interesting for building the PMQs. The average angular error of the whole population is 1.32^o, but if only the 560 permanent magnet blocks used for building the required magnets are considered, the average error is 0.764^o. In this region, the distribution is approximately uniform.

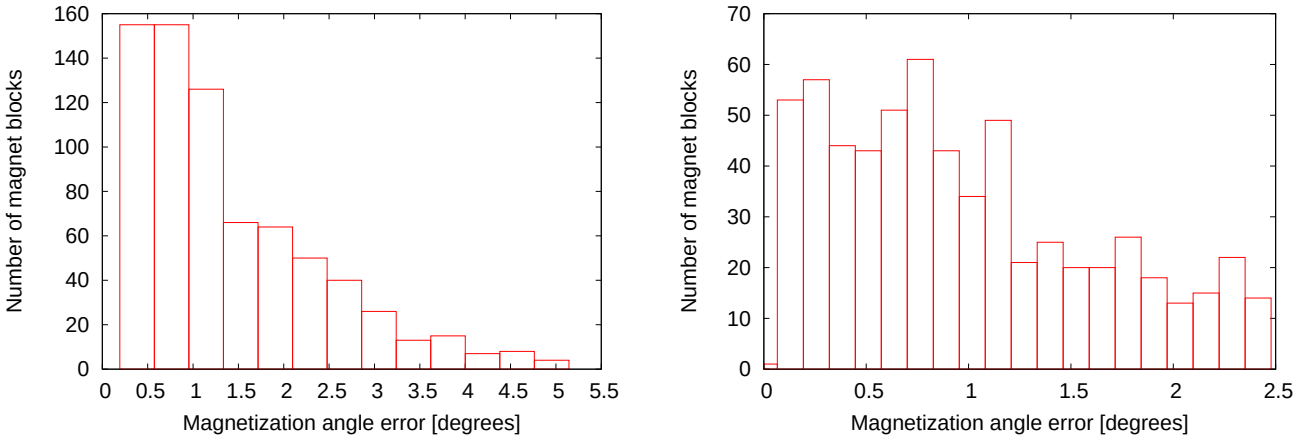

Figure 10.5 – Histogram of the angular error

It is interesting to note that there exists a significant correlation between magnet strength and angular error, fig. 10.6 shows a plot of the residual magnetization vs. the angular error. It can be easily observed that the blocks with the higher error tend to be weaker as well. These magnets are probably magnetized in a region of the magnetizing coil far from the center and present, therefore, both a strength and angle problem.

As each block is measured once with the north pole upwards and another time with the north pole downwards, we can compare the difference between both measurements. The histogram of frequencies of the north-south effect may be seen in fig. 10.7. Most of the population is below 0.5% and the effect seems not to be very worrying. Actually, the effect was not taken into account for the sorting, and the value that was used for this purpose is

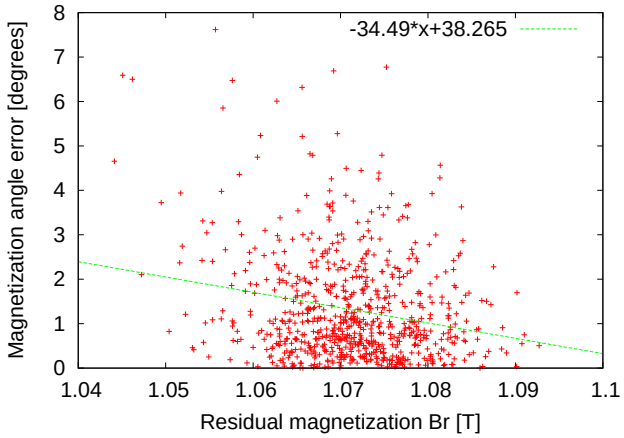

Figure 10.6 – Correlation between residual magnetization and angular error

the average between the north and south measurements.

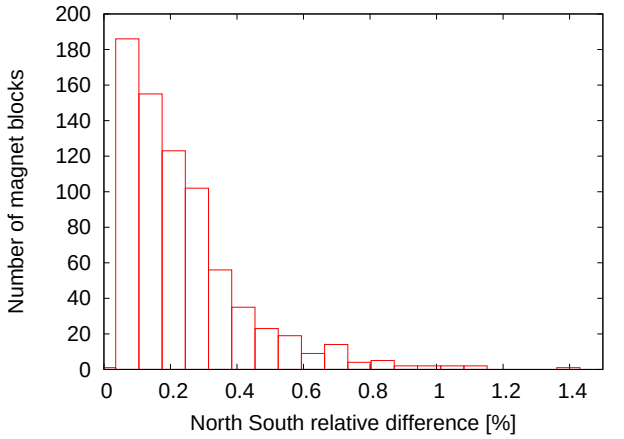

Figure 10.7 – North-South difference histogram

It is interesting to state that although the process of measuring all the magnet blocks in-house was very satisfactory from the technical point of view, it was rather time consuming and that for later projects of PMQs, we have preferred to have the magnets supplied with an individual manufacturer measurement. This was related not to a technical problem of the Hall probe measurement, but to the need to shorten the manufacturing cycle of the PMQs. A random measurement of a few magnets using both methods allows to perform a cross-check and to correlate the measurements taking into account that one of the methods provide B_r and the other the actual magnetization under the self-field.

CHAPTER 11

Assembly and measurement of the PMQ

11.1 Magnet sorting

With the measurements described in chapter 10, we have now characterized the magnetic properties of the permanent magnet blocks. It is time to sort the magnets in order to assembly the PMQs. Most of the rules used in this section are easily obtained from the analytical design principles that has been described previously. A very succinct description of the method used for sorting would be the following:

1. Sort the blocks by angular error in ascending order
2. Reject all the magnets that have a large angular error. In our case we have taken the best 560 magnet blocks and rejected the rest, about 200. This has left us only with magnet whose angular error is below 1°
3. Now, sort the magnets in either ascending or descending order according to their residual magnetization
4. A group of 8 consecutive magnets will be used for each PMQ
5. Inside each group two consecutive magnets must be diagonally opposed in order to keep the magnetic center
6. The four stronger magnets of each group must be in the tangential positions, while the 4 weakest must be in the radial ones, in order to limit B_6

The previous rules have been programmed in an Excel macro that automatically creates the groups of 8 magnets that must be put together. Now, we have to know to which PMQ assign this set of magnets and which is the shim that must be used.

11.2 Selection of the magnet sets and shimming

In principle, each of the PMQ integrated gradients given in tab. 9.2 could be built with several combinations of permanent magnet block strengths and shims; with each of these combinations giving a correct PMQ. In order to create all the combinations possible an Excel table has been created with one row per PMQ and a given value of radial and tangential shim in each column. The cell corresponding to a certain row and a certain column contains the

value of the residual magnetization that provides the integrated gradient of this PMQ with this set of shims.

In order to limit the value of B_6, a maximum difference of 0.1 mm is allowed between the radial and the tangential shims, and the radial shim is always equal or larger than the tangential one.

Because only residual magnetization between 1.04 T and 1.09 T are available, only some of the cells provide a valid solution. By marking these valid solutions, a band is created in the Excel sheet that provides the regions where a possible PMQ may be built. A small section of the used table is shown in tab. 11.1, where the possible solutions are shown with a red background.

The table should be used in the following way, each of the rows corresponds to a single magnet, the possible solutions are the cells with the red background, and the corresponding shims, radial and tangential, should be read on one of the upper rows.

Table 11.1 – Example of the Excel sheet that was used for the sorting of the magnets. Only the beginning of the spreadsheet is shown.

Radial Shim		1.00E-03	1.00E-03	1.10E-03	1.10E-03	1.20E-03	1.20E-03	1.30E-03	1.30E-03	1.40E-03	1.40E-03	1.50E-03	1.50E-03	1.60E-03
Tangential shim		9.00E-04	1.00E-03	1.00E-03	1.10E-03	1.10E-03	1.20E-03	1.20E-03	1.30E-03	1.30E-03	1.40E-03	1.40E-03	1.50E-03	1.50E-03
GdL		-1.78540299	-1.77116504	-1.75730906	-1.74333705	-1.72971862	-1.71603734	-1.70282799	-1.68939079	-1.67630779	-1.66309098	-1.65051663	-1.63763136	-1.62505802
L4D.MQDP.0231	2.031136	1.21807328	1.22786506	1.2375465	1.24746484	1.25728639	1.26731023	1.27714114	1.28729936	1.29734628	1.30765647	1.31761876	1.3279861	1.33826094
L4D.MQFP.0232	1.762152	1.05676344	1.0652585	1.07365782	1.08226267	1.09078354	1.09947993	1.10800892	1.11682188	1.12553829	1.1344831	1.14312608	1.15212047	1.16103461
L4D.MQFP.0233	1.762152	1.05676344	1.0652585	1.07365782	1.08226267	1.09078354	1.09947993	1.10800892	1.11682188	1.12553829	1.1344831	1.14312608	1.15212047	1.16103461
L4D.MQDP.0234	1.74418	1.04598562	1.05439404	1.06270769	1.07122479	1.07965876	1.08826645	1.09670846	1.10543154	1.11405905	1.12291263	1.13146746	1.14037011	1.14919334
L4D.MQDP.0235	1.74418	1.04598562	1.05439404	1.06270769	1.07122479	1.07965876	1.08826645	1.09670846	1.10543154	1.11405905	1.12291263	1.13146746	1.14037011	1.14919334
L4D.MQFP.0236	1.702012	1.02069745	1.02890258	1.03701524	1.04532642	1.05355649	1.06195608	1.07019399	1.07870618	1.08712511	1.09576464	1.10411265	1.11280006	1.12140998
L4D.MQFP.0237	1.702012	1.02069745	1.02890258	1.03701524	1.04532642	1.05355649	1.06195608	1.07019399	1.07870618	1.08712511	1.09576464	1.10411265	1.11280006	1.12140998
L4D.MQDP.0238	1.690856	1.01400719	1.02215854	1.03021803	1.03847473	1.04665086	1.05499539	1.0631793	1.0716357	1.07999944	1.08858234	1.09687563	1.10550611	1.11405959
L4D.MQDP.0239	1.690856	1.01400719	1.02215854	1.03021803	1.03847473	1.04665086	1.05499539	1.0631793	1.0716357	1.07999944	1.08858234	1.09687563	1.10550611	1.11405959
L4D.MQFP.0240	1.656788	0.9935766	1.00156371	1.00946081	1.01755115	1.02556254	1.03373894	1.04175797	1.05004398	1.05823921	1.06664918	1.07477537	1.08323196	1.0916131
L4D.MQFP.0241	1.656788	0.9935766	1.00156371	1.00946081	1.01755115	1.02556254	1.03373894	1.04175797	1.05004398	1.05823921	1.06664918	1.07477537	1.08323196	1.0916131
L4D.MQDP.0242	1.646004	0.98710943	0.99504455	1.00289025	1.01092793	1.01888718	1.02701036	1.03497719	1.04320926	1.05135115	1.05970638	1.06777968	1.07618122	1.08450781
L4D.MQDP.0243	1.646004	0.98710943	0.99504455	1.00289025	1.01092793	1.01888718	1.02701036	1.03497719	1.04320926	1.05135115	1.05970638	1.06777968	1.07618122	1.08450781
L4D.MQDP.0244	1.613084	0.96736729	0.97514371	0.98283249	0.99070942	0.99850948	1.0064702	1.01427769	1.02234513	1.03032418	1.0385123	1.04642414	1.05465765	1.06281771
L4D.MQFP.0245	1.613084	0.96736729	0.97514371	0.98283249	0.99070942	0.99850948	1.0064702	1.01427769	1.02234513	1.03032418	1.0385123	1.04642414	1.05465765	1.06281771
L4D.MQDP.0246	1.602596	0.96107763	0.96880349	0.97644228	0.984268	0.99201734	0.9999263	1.00768303	1.01569801	1.02362518	1.03176007	1.03962047	1.04780045	1.05590745
L4D.MQDP.0247	1.602596	0.96107763	0.96880349	0.97644228	0.984268	0.99201734	0.9999263	1.00768303	1.01569801	1.02362518	1.03176007	1.03962047	1.04780045	1.05590745
L4D.MQFP.0248	1.570652	0.94192079	0.94949266	0.95697919	0.96464892	0.9722438	0.97999511	0.98759723	0.99545245	1.00322161	1.01119435	1.01889807	1.026915	1.03486041
L4D.MQFP.0249	1.570652	0.94192079	0.94949266	0.95697919	0.96464892	0.9722438	0.97999511	0.98759723	0.99545245	1.00322161	1.01119435	1.01889807	1.026915	1.03486041
L4D.MQDP.0250	1.560476	0.93581824	0.94334105	0.95077908	0.95839912	0.96594479	0.97364588	0.98119875	0.98900308	0.9967219	1.00464299	1.01229679	1.02026178	1.02815571
L4D.MQDP.0251	1.560476	0.93581824	0.94334105	0.95077908	0.95839912	0.96594479	0.97364588	0.98119875	0.98900308	0.9967219	1.00464299	1.01229679	1.02026178	1.02815571
L4D.MQFP.0252	1.52948	0.91722992	0.92460331	0.93189359	0.93936227	0.94675806	0.95430619	0.96170903	0.96935834	0.97692384	0.98468759	0.99218937	0.99999615	1.00773328
L4D.MQDP.0253	1.52948	0.91722992	0.92460331	0.93189359	0.93936227	0.94675806	0.95430619	0.96170903	0.96935834	0.97692384	0.98468759	0.99218937	0.99999615	1.00773328
L4D.MQDP.0254	1.519548	0.9112737	0.9185992	0.92584214	0.93326232	0.94061009	0.9481092	0.95546397	0.96306361	0.97057998	0.97829331	0.98574638	0.99350246	1.00118935
L4D.MQDP.0255	1.519548	0.9112737	0.9185992	0.92584214	0.93326232	0.94061009	0.9481092	0.95546397	0.96306361	0.97057998	0.97829331	0.98574638	0.99350246	1.00118935
L4D.MQFP.0256	1.489324	0.89314835	0.90032815	0.90742703	0.91469962	0.92190124	0.92925119	0.93645967	0.94390815	0.95127503	0.95883494	0.96613976	0.97374157	0.98127557
L4D.MQFP.0257	1.489324	0.89314835	0.90032815	0.90742703	0.91469962	0.92190124	0.92925119	0.93645967	0.94390815	0.95127503	0.95883494	0.96613976	0.97374157	0.98127557
L4D.MQDP.0258	1.479608	0.88732166	0.89445462	0.90150719	0.90873233	0.91588697	0.92318897	0.93035043	0.93775032	0.94506913	0.95257972	0.95983689	0.96738911	0.97487396
L4D.MQDP.0259	1.479608	0.88732166	0.89445462	0.90150719	0.90873233	0.91588697	0.92318897	0.93035043	0.93775032	0.94506913	0.95257972	0.95983689	0.96738911	0.97487396
L4D.MQFP.0260	1.450012	0.86957293	0.8765632	0.8834747	0.89055533	0.89756685	0.9047228	0.911741	0.91899288	0.9261653	0.93352566	0.94063766	0.94803882	0.95537395
L4D.MQFP.0261	1.450012	0.86957293	0.8765632	0.8834747	0.89055533	0.89756685	0.9047228	0.911741	0.91899288	0.9261653	0.93352566	0.94063766	0.94803882	0.95537395
L4D.MQDP.0262	1.440476	0.86385418	0.87079849	0.87766453	0.88469859	0.89166401	0.89877289	0.90574494	0.91294912	0.92007437	0.92738633	0.93445156	0.94180404	0.94909094
L4D.MQDP.0263	1.440476	0.86385418	0.87079849	0.87766453	0.88469859	0.89166401	0.89877289	0.90574494	0.91294912	0.92007437	0.92738633	0.93445156	0.94180404	0.94909094
L4D.MQDP.0264	1.411444	0.84644368	0.85324802	0.85997569	0.86686798	0.87369301	0.88065862	0.88749015	0.89454914	0.90153078	0.90869537	0.9156182	0.9228225	0.92996253
L4D.MQFP.0265	1.411444	0.84644368	0.85324802	0.85997569	0.86686798	0.87369301	0.88065862	0.88749015	0.89454914	0.90153078	0.90869537	0.9156182	0.9228225	0.92996253
L4D.MQDP.0266	1.405008	0.842584	0.84935732	0.85605431	0.86291518	0.86970909	0.87664293	0.88344331	0.89047011	0.89741992	0.90455184	0.9114431	0.91861455	0.92572202
L4D.MQDP.0267	1.405008	0.842584	0.84935732	0.85605431	0.86291518	0.86970909	0.87664293	0.88344331	0.89047011	0.89741992	0.90455184	0.9114431	0.91861455	0.92572202
L4D.MQFP.0268	1.38432	0.8301774	0.83685099	0.84344937	0.85020921	0.85690308	0.86373483	0.87043508	0.87735841	0.88420588	0.89123279	0.89802259	0.90508844	0.91209126
L4D.MQFP.0269	1.38432	0.8301774	0.83685099	0.84344937	0.85020921	0.85690308	0.86373483	0.87043508	0.87735841	0.88420588	0.89123279	0.89802259	0.90508844	0.91209126
L4D.MQDP.0270	1.3798	0.82746675	0.83411855	0.84069538	0.84743315	0.85410517	0.86091461	0.86759298	0.87449371	0.88131883	0.88832279	0.89509042	0.9021332	0.90911315

11.3 Measurement methods useful for PMQ

In this section we describe several methods that are useful for measuring the PMQs. We pay special attention to field mapping with a Hall probe, as it is the method finally used to characterize the magnets at ELYTT.

11.3.1 The Hall probe method

When combined with a computer controlled displacement system a Hall probe may provide a detailed field map of the magnet. It is essential for obtaining the field in dipoles where the beam is curved by a large angle and in general for obtaining the field of magnets in which the paraxial approximation is not good. Typically PMQs are short and the integrating methods like the rotating coil or the stretch wire are better adapted. Nevertheless, because the availability of a Hall probe system at ELYTT, the method was chosen for the measurement of the linac4 PMQs. Although the time required to fully map a magnet was larger that the required by a rotating coil, the operation was not labor intensive, as the machine operates automatically once the system has been set up.

The calibration of the system followed a similar approach than the one that has been described for the measurement of the permanent magnet blocks. A dedicated V-shaped tooling was built in which the PMQ could be blocked and which was equipped with 3 pin holes for locating the zero field conical magnet. Before the PMQ was placed in the tooling, the conical magnet was placed alternatively in the pin holes and the 3 zero field points were located in the bench coordinates. A transformation matrix was then calculated to convert the bench coordinates to the magnet coordinates and vice versa. The methods for the transformation were programmed as a set of C++ classes using Visual C++. In addition, the probe was moved in 3 directions around the zero field point of the last position of conical magnet. By the construction of the magnet, the movement should bring the probe to a point were only field in the direction of the displacement exists. As the probe will normally measure field in all axes, it is possible to obtain the rotation matrix of the probe. The method is fully described in the chapter on the measurement of the permanent magnet block §10.1. Fig. 11.1 shows two photographs of the measurement of a PMQ similar in dimension to the linac4 ones.

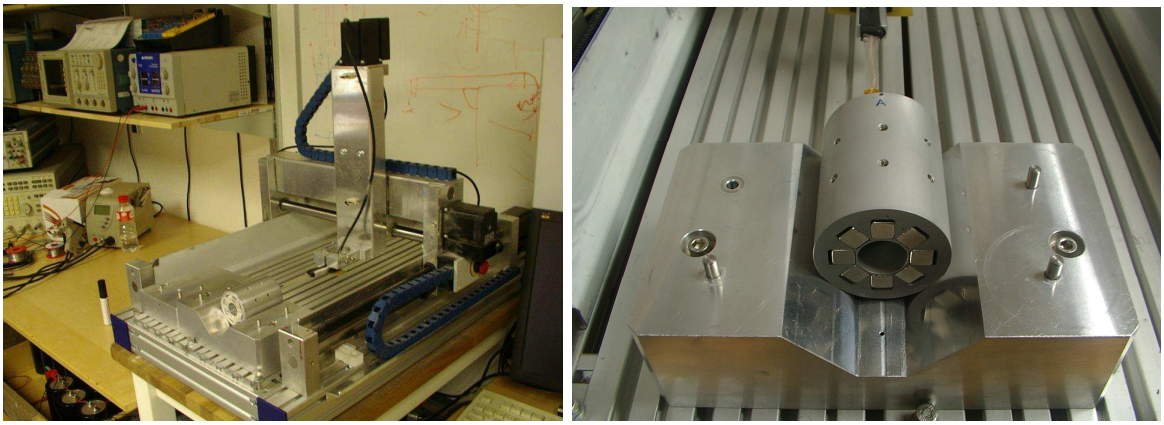

Figure 11.1 – Measuring a PMQ. Remark on the right photograph the locating pins for the conical magnet.

An additional problem with the measurement of the 80 mm long linac4 PMQs is that the Hall probe cannot enter into the magnet more than 40 mm before a thicker part of the probe clashes with the front of the magnet, therefore the magnet must be measured from both sides and the measurements must be jointed for the final interpretation of the results. There are two ways in which this addition of the measurements of both sides may be performed. In the

first method, the raw data are added by calculating which are the matching angles when the magnet is seen from each end and how the components change sign. In the second method the full harmonic analysis of each side is performed and then the harmonics are combined according to certain rules, as shown in §7.5.2.

The program to measure the magnet describes a cloud of points located at the maximum radius compatible with the magnet aperture and the Hall probe size. The number of angular measurements at a given axial position is 64 and the number of axial measurements from each side is 35, 70 points in total. In total 4480 measurements are taken per magnet.

The post-processing of the PMQ measurement starts with the axial integration of all the data at a certain angular position. This integral is obtained with the alternative extended Simpson rule [27].

$$\int_0^L f(z)\,dz = \frac{L}{n}\left(\frac{17}{48}f_1 + \frac{59}{48}f_2 + \frac{43}{48}f_3 + \frac{49}{48}f_4 + \sum_5^{n-4} f_i + \frac{49}{48}f_{n-3} + \frac{43}{48}f_{n-2} + \frac{59}{48}f_{n-1} + \frac{17}{48}f_n\right) \tag{11.1}$$

This integration method was used independently for all the angular positions and all the components of the magnetic field. Afterwards, the Cartesian components were combined to obtain the integrated radial components of the field at all the angular positions and finally a standard Fourier analysis of the radial field was performed to obtain the field harmonics.

For the particular application of the linac4 PMQ the mapping of the magnets with a Hall probe was very efficient and accurate to obtain the magnetic center (using the B_1 and A_1 harmonics), the integrated gradient and the quadrupolar field roll (using A_2)). Higher order harmonics could not be calculated as accurately as the lower ones due to the limited aperture available with respect to the Hall probe size and probably to the size of the actual magnetic field measuring chip. Nevertheless, by construction of the magnet is almost impossible to have the magnetic center and roll correct and to have the higher order harmonics higher than the allowed 100 units, as the higher order harmonics are efficiently canceled by having all magnets of similar strength and with a small magnetization angle error.

11.3.2 The rotating coil method

Although the rotating coil method was not used in the present project, it is very well adapted to measure PMQs and, therefore, is fully described here. The rotating coil method is based in measuring the voltage induced in a coil of special shape which is centered in the aperture of the magnet to be measured and rotated along the magnet axis. The time integral of the voltage is proportional to the flux linked by the coil, or otherwise stated, to the axial component of the vector potential along the measuring coil turns. From this vector potential, it is possible to obtain directly the field harmonics. Here, we will show the general theory and particularize it to a pair of typical cases.

For any magnetic system, the induced voltage in a coil is the time derivative of the flux passing through the coil. The flux can be expressed as a function of the flux density $\vec{B}$ or the vector potential $\vec{A}$ using the equation 11.2.

$$\Phi = \iint_S \vec{B}\cdot d\vec{S} = \oint_C \vec{A}\cdot d\vec{l} \tag{11.2}$$

If the system present a displacement symmetry axis (let it be z) the vector potential only has a component parallel to that axis and, of course, the value of that component doesn't depend on z. In that kind of system equation 11.2 reduces to eq. 11.3.

$$\Phi \;=\; L\,(A_2 - A_1) \tag{11.3}$$

A further generalization of 11.3 can be obtained if we consider a system of conductors placed along the z axis and interconnected alternatively at both extremities. The general expression for the flux is given by equation 11.4. The sign in this equation varies between two consecutively interconnected conductors.

$$\Phi \;=\; -\,L \sum_{m=1}^{h} \pm A_m \tag{11.4}$$

Where the sign applied to the vector potential is related to the direction that the current would have in the measuring coil would be used to transport current instead of being used to couple to the external magnetic flux.

The next step is to relate the field harmonics to the vector potential. The equation 11.5 is the expression of the field inside the aperture of the magnet as a function of the coefficients of the multipole expansion at a reference radius R. The value of the vector potential as a function of the field multipoles can be obtained through integration in the complex plane and using the fact that the function $B_y + iB_x$ is analytical in a domain which contains no field sources, this integration is performed in 11.6 and the obtained multipole expansion is given in equation 11.7.

$$F \;=\; B_y + iB_x \;=\; \sum_{n=1}^{\infty} (B_n + iA_n) \left(\frac{z}{R}\right)^{n-1} \tag{11.5}$$

$$A \;=\; \int_C (B_x\,dy - B_y\,dx) \;=\; -\,\Re \int_C F\,dz \tag{11.6}$$

$$A \;=\; \sum_{n=1}^{\infty} \frac{R}{n} \left(\frac{r}{R}\right)^{n} (A_n \sin n\phi - B_n \cos n\phi) \tag{11.7}$$

This equation was already obtained at §7.3 taking into account that A was the real part of the complex potential.

Introducing the value of the vector potential of equation 11.7 in equation 11.4 it is possible to obtain the value of the total flux inducing voltage in the conductor system as a function of the multipoles that must be measured. The resulting equation is 11.8. The internal sum runs in the conductors orthogonal to the field.

$$\Phi \;=\; \sum_{n=1}^{\infty} B_n \sum_{m=1}^{h} \pm \frac{RL}{n} \left(\frac{r_m}{R}\right)^{n} \cos n\phi_m - \sum_{n=1}^{\infty} A_n \sum_{m=1}^{h} \pm \frac{RL}{n} \left(\frac{r_m}{R}\right)^{n} \sin n\phi_m \tag{11.8}$$

In order to study the measuring capability of the assembly it is important to split the last equation in the terms due to each harmonic. This is done in the following set of equations,

in which the sensitivity of the flux to each harmonic is defined. We define the sensitivity coefficients S_n and $\bar{S}_n$ which give the flux induced by each multipolar component. According to them the flux can be expressed as:

$$\Phi = \sum_{n=1}^{\infty} \left(B_n S_n + A_n \bar{S}_n \right) \tag{11.9}$$

$$S_n = \sum_{m=1}^{h} \pm \frac{RL}{n} \left(\frac{r_m}{R} \right)^n \cos n\phi_m \tag{11.10}$$

$$\bar{S}_n = \sum_{m=1}^{h} \mp \frac{RL}{n} \left(\frac{r_m}{R} \right)^n \sin n\phi_m \tag{11.11}$$

We will now study two particular cases, the first corresponds to a radial coil in which the measuring turns are located at a constant radius on top of a winding mandrel. The second case corresponds to a planar coil, in which all the turns are located on the same plane.

Particular case I

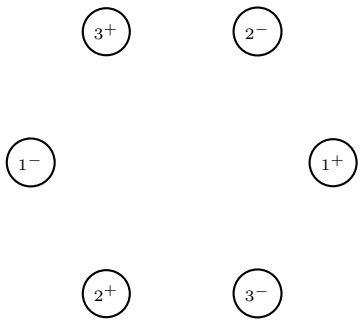

Figure 11.2 – Conductor placement

In this section the general expressions developed above are employed for the particular case of the figure 11.2. This design is developed to measure the sextupolar component B_3 and having a very low sensitivity to the main dipolar component. As we can see there are 6 conductors grouped in 3 coils. It is possible to group them in several ways, but the result must be the same. First of all the flux due to a diametrically placed coil is obtained. In the next equations, it is possible to see how the even harmonics cannot be measured with diametric coils.

$$S_n = \sum_{m=1}^{loops} \frac{RL}{n} \left(\frac{r_m}{R} \right)^n \left(\cos n\phi_m - \cos n(\phi_m + \pi) \right) \tag{11.12}$$

$$S_n = \begin{cases} \sum_{m=1}^{loops} \frac{2RL}{n} \left(\frac{r_m}{R} \right)^n \cos n\phi_m & \text{n odd} \\ 0 & \text{n even} \end{cases} \tag{11.13}$$

Using the expressions for a diametrical coil it is possible to calculate the nominal sensitivity of the structure represented in 11.2. As can be seen, with an ideal placement of the conductors it is possible to cancel the sensitivity to the dipole. On the other hand, the coils add the voltages created from the sextupole.

$$S_1^0 \;=\; 2rL\left(1+\cos\frac{2\pi}{3}+\cos\frac{4\pi}{3}\right) \;=\; 0 \tag{11.14}$$

$$S_3^0 \;=\; \frac{2RL}{3}\left(\frac{r}{R}\right)^3\left(1+\cos 3\frac{2\pi}{3}+\cos 3\frac{4\pi}{3}\right) \;=\; 2rL\left(\frac{r}{R}\right)^2 \tag{11.15}$$

Of special interest is the ratio between the sensitivity of the system to the dipole and the sextupole for the actual structure. As the difference between the actual and the ideal structure is not large, it is possible to estimate the value of the ratio from a linearization of S_1 around the ideal geometry. This expression is given in equation 11.16, where t_m is the tangential displacement in the increasing angles direction.

$$\frac{S_1}{S_3} \;=\; \frac{\sum_{m=1}^{h}\pm Lr_m\cos\phi_m}{2rL\left(\frac{r}{R}\right)^2} \;=\; \frac{\sum_{m=1}^{h}\pm\cos\phi_m^0\;\Delta r_m\mp\sin\phi_m^0\;r_m^0\;\Delta\phi_m}{2r\left(\frac{r}{R}\right)^2} \;=$$
$$\frac{1}{2}\left(\frac{R}{r}\right)^2\sum_{m=1}^{h}\left(\pm\cos\phi_m^0\;\frac{\Delta r_m}{r}\mp\sin\phi_m^0\;\frac{\Delta t_m}{r}\right) \tag{11.16}$$

In the table 11.2, it can be seen the increase in the ratio S_1/S_3 due to a variation of 1 mm around the ideal position.

Table 11.2 – Increase in the S_1/S_3 ratio for 1 mm error in conductor positioning

	Conductor number					
	1^+	2^-	3^+	1^-	2^+	3^-
Radial	$3.2\cdot10^{-3}$	$1.6\cdot10^{-3}$	$1.6\cdot10^{-3}$	$3.2\cdot10^{-3}$	$1.6\cdot10^{-3}$	$1.6\cdot10^{-3}$
Azimuthal	0	$2.77\cdot10^{-3}$	$2.77\cdot10^{-3}$	0	$2.77\cdot10^{-3}$	$2.77\cdot10^{-3}$

The voltage induced in the system can be calculated with equation 11.17. The integral of the voltage can be expressed as a linear combination of the field multipoles with the sensibilities as coefficients. This is expressed in equation 11.18.

$$v \;=\; -\frac{d\Phi}{dt} \;=\; -\sum_{n=1}^{\infty}\left(S_n\dot{B}_n+\bar{S_n}\dot{A}_n\right) \tag{11.17}$$

$$\int_0^t v\,dt \;=\; -\sum_{n=1}^{\infty}\left(S_nB_n+\bar{S_n}A_n\right) \tag{11.18}$$

Of all the terms included in equation 11.18, only those who satisfy one of the following characteristics are significant.

- The sensitivity is different of 0 even for conductors ideally placed. This is true for S_3, S_9,

... In that case S_n is large enough to give a large term even for a small field multipole.

- The value of the field multipole is extremely large. This is the case of B_1. For that term, the sensitivity due to the construction errors are large enough to give a large voltage.

According to the last considerations equation 11.18 can be reduced to the 2 terms equation 11.19, in which only the dipolar and sextupolar terms appear.

$$\int_0^t v\,dt \;=\; -\left(S_1B_1 + S_3B_3\right) \;=\; -B_1S_3\left(\frac{S_1}{S_3} + \frac{B_3}{B_1}\right) \;=\; -B_1S_3\left(\frac{S_1}{S_3} + 10^{-4}b_3\right) \quad (11.19)$$

According with equation 11.19, it is possible to see that the integral of the induced voltage depends on two terms. One of them, the ratio S_1/S_3 derives from the construction tolerances, the other $10^{-4}b_3$ is the magnitude that is desired to measure. There are two possibilities:

- If no calibration is desired it is necessary that the term derived from the sextupole is much larger than the dipolar term. If one tenth of sextupolar unit is the accuracy need, that means that the dipolar term must be in the order of 10^{-5}, according with table 11.2, that means that the tolerances must be in the order of a few microns, which seems a non-realistic objective.

- Equation 11.19 gives an idea of how to make the calibration of the system, a single measurement must give B_1 and b_3, the value of S_3 can be accurately approximated by its design value given by equation 11.15. Finally the ratio S_1/S_3 can be calculated. In such a way, and supposed that there is a way to measure the dipole, it is only necessary that the dipolar and sextupolar terms in equation 11.19 are of the same order of magnitude. This allows the system to be built with tolerances of a few hundreds of microns.

Planar coils

Very often the coils used to measure the magnetic field are approximately planar. A typical configuration may be seen in fig. 11.3.

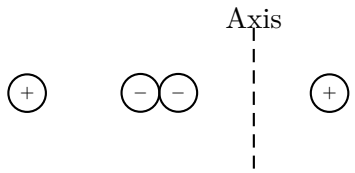

Figure 11.3 – Example of a planar coil.

In this case, all the turns are in the same plane, and the angle Φ_m is independent of the turn, the normal and skew components of the field, may be obtained in a more straightforward way from the time signal of the voltage.

One important advantage of the planar coils is that they may be manufactured using the Printed Circuit Board (PCB) technology which is widely used today. Small batches of coils may be manufactured on short time and at very low cost.

An example of a coil for measuring permanent magnet quadrupoles may be seen in fig. 11.4. In this design there are two concentric coils, each of 4 layers. The coils are eccentric to provide a signal to the even harmonics, including the quadrupole. The number of turns is calculated to cancel the sensitivity to B_2 when they are connected in anti-series. An excellent sensitivity to B_2 can be obtained by connecting them in series. The leads of both coils are available to the user, which may choose the type of measurement. This planar coil was designed using the equations of the previous section, and directly exported in DXF format to Orcad in order to create the GERBER files required for the manufacturing of the PCB.

Figure 11.4 – Example of a coil designed by the author for the measuring of small aperture PMQs. Left, global view. Right, detail of the connection side, showing the vias structure of the PCB.

In fig. 11.5 we may see the finalized coil, including the soldered wires and the jumpers to connect the inner turns to the outer ones.

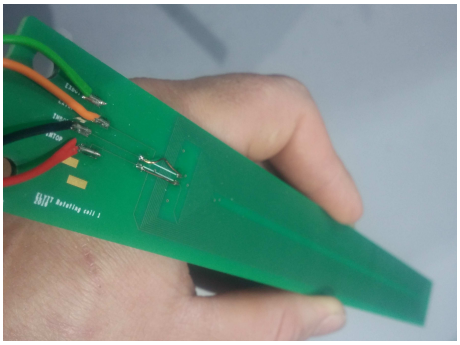

Figure 11.5 – The coil as finally built

11.3.3 The stretched wire method

The stretched wire method may easily be understood with the equations of the previous chapter. In this case, the voltage is induced by a single wire being moved in the magnet aperture with an external CNC system. The stretched wire is very useful for quickly determining the magnetic center and the magnetic length of straight magnets.

11.3.4 The vibrating wire method

The vibrating wire method was introduced by A. Temnykh while working in the measurements of the CESR Phase III project [50]. It is based in setting a stationary wave on a wire under the excitation force of the magnetic field acting on an alternating current passing through the wire. By changing the frequency of the current, it is possible to excite several resonances and by measuring the amplitude of the vibration at a certain point of the wire, it is possible to reconstruct the spatial distribution of the field. Intuitively, wire modes which have maximum amplitude near the regions of high magnetic field are mostly excited. The method is highly sensitive due to the very low damping coefficient of the wire. Even a small magnetic field will generate a significant vibration of the wire near the resonant frequencies.

Fig. 11.6 represents a simplified scheme of a vibrating wire measurement. We propose a vertical wire, because the typical reduced dimension of a PMQ allows such position and the measurement simplifies because it is not necessary to take the sag of the wire in to account.

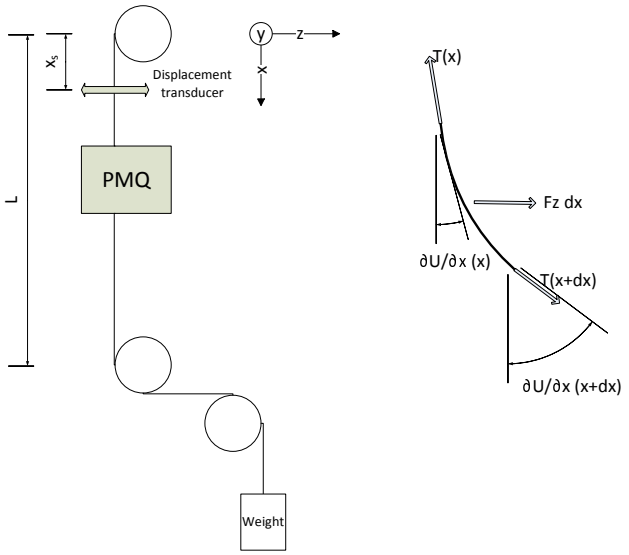

Figure 11.6 – Left, schematic representation of a vibrating wire measurement of a PMQ. Right, forces acting on a length dx of wire

We will now obtain the governing equations of the vibrating wire. In fig. 11.6 we can see the forces acting on a piece of wire of length dx. We will call U the displacement in the z direction $T(x)$ is the tension at a certain point and μ the mass of the wire per unit length. Newton's second law in the z direction will be,

$$\left(T(x+dx)\frac{\partial U}{\partial x}(x+dx) - T(x)\frac{\partial U}{\partial x}(x) + f_z dx\right) = \mu dx\left(\frac{\partial^2 U}{\partial t^2} + \gamma\frac{\partial U}{\partial t}\right) \tag{11.20}$$

, where γ is a viscous damping coefficient of the wire which includes all mechanism of losses in the vibration, mostly friction with air and internal damping of the material.

If we apply the equilibrium of forces in the x direction, we obtain how the tension will change with the slope of the wire. The result is that for small angles the tension is constant, as it scales with $\partial U/\partial x$. The final equation is then,

$$T\frac{\partial^2 U}{\partial x^2} + f_z = \mu\left(\frac{\partial^2 U}{\partial t^2} + \gamma\frac{\partial U}{\partial t}\right) \tag{11.21}$$

We will solve now 11.21 in two different conditions. First, we will solve the well known problem of the eigenvalues of the vibrating wire and then we will superpose the particular solution that includes the alternating forces due to the interaction of the AC current in the wire with the steady magnetic field. To solve the eigenvalue problem, we separate variables, i.e. we consider that the displacement $U(x,t)$ is obtained as the multiplication of two functions, one depending only on x and the other in t.

$$U(x,t) = X(x)S(t) \tag{11.22}$$

If we introduce eq. 11.22 into eq. 11.21 and group all the terms that depend on t on one side and on x on the other side, we obtain,

$$\frac{S"}{S} + \gamma\frac{S'}{S} = \frac{T}{\mu}\frac{X"}{X} = -\omega^2 \tag{11.23}$$

We have equated both terms to a constant because the first would depend only on t and the second on x, and a constant is the most general function depending at the same time only in x and only in t at the same time. The ordinary differential equations for S and X will be,

$$S" + \gamma S' + \omega^2 S = 0 \tag{11.24}$$

$$X" + \omega^2\frac{\mu}{T}X = 0 \tag{11.25}$$

The spatial solution X has two nodes at 0 and L. Therefore, the solution must be,

$$X(x) = A\sin\frac{n\pi x}{L} \tag{11.26}$$

and therefore only certain values of ω are possible, i.e. the ones satisfying

$$\omega = \omega_n = \frac{n\pi}{L}\sqrt{\frac{T}{\mu}} \tag{11.27}$$

The solutions of the time evolution part eq. 11.24 will be quantified as well by ω_n and will be,

$$S(t) = \exp\left(-j\frac{\gamma}{2}t\right)\cos\left(\omega_n t + \phi_n\right) \tag{11.28}$$

So that the general solution will be,

$$U(x,t) = \sum_{n=1}^{\infty} A_n \exp\left(-j\frac{\gamma}{2}t\right)\cos\left(\omega_n t + \phi_n\right)\sin\frac{n\pi x}{L} \tag{11.29}$$

So that the general solution of the homogeneous function is the sum of all the modes. Each mode is characterized by an amplitude A_n and a phase ϕ_n. For the vibrating wire mode, the most important conclusion of eq 11.29 is that it is a decaying solution and after a certain

time of a transitory will have disappeared and the only solution resting will be the solution synchronous with the excitation force.

In the vibrating wire method an alternating current will be passed through the wire and a force, $f_z(t,x) = i(t)B_y(x)$, will appear. As the time variation of the solution will follow the excitation frequency, we can convert the equation to phasor notation[1] and say that,

$$U(x,t) = \hat{U}(x)\exp j\omega t \tag{11.30}$$

The vibrating wire equation is then converted to an ordinary differential equation,

$$T\frac{d^2\hat{U}}{dx^2} + \mu\left(\omega^2 + j\omega\gamma\right)\hat{U} = -\hat{I}B(x) \tag{11.31}$$

We will represent now the magnetic field distribution along x as a Fourier series. We will suppose that the magnetic field cancels on both extremities of the wire. In this condition,

$$B(x) = \sum_{n=1}^{\infty} B_n \sin\left(\frac{n\pi}{L}x\right) \tag{11.32}$$

$$\hat{U}(x) = \sum_{n=1}^{\infty} \hat{U}_n \sin\left(\frac{n\pi}{L}x\right) \tag{11.33}$$

Normally, the solution of eq. 11.31 would require to obtain the general solution of the homogeneous equation and a particular solution of the non homogeneous equation. Nevertheless, in this case we are directly fitting the solution of the non homogeneous equation with a set of functions that already satisfy the boundary conditions, $\hat{U}(0) = \hat{U}(L) = 0$.

$$\hat{U}_n\left(-\frac{T}{\mu}\left(\frac{n\pi}{L}\right)^2 + \omega^2 + j\omega\gamma\right) \tag{11.34}$$

We will represent the resonant frequencies as ω_n,

$$\omega_n = \sqrt{\frac{T}{\mu}}\left(\frac{n\pi}{L}\right) \tag{11.35}$$

and the coefficients of the Fourier expansion of the phasor of the displacement will be,

$$\hat{U}_n = \frac{\hat{I}B_n}{\mu\left(\left(\omega_n^2 - \omega^2\right) - j\omega\gamma\right)} \tag{11.36}$$

The displacement phasor will be,

$$\hat{U}(x) = \sum_{n=1}^{\infty} \frac{\hat{I}B_n}{\mu\left(\left(\omega_n^2 - \omega^2\right) - j\omega\gamma\right)} \sin\left(\frac{n\pi}{L}x\right) \tag{11.37}$$

The wire vibration is obtained from the synchronous demodulation of the displacement at a certain point x_s with the current. The measured magnitude is,

[1] In this chapter, the *hat* symbol represents a time phasorial magnitude

$$F(\omega) = \frac{1}{T}\int_0^T U(x,t)i(t)dt = \frac{1}{2}\Re\left(\hat{U}\hat{I}\right) \tag{11.38}$$

The results is,

$$F(\omega) = \sum_{n=1}^{\infty} \frac{I^2 B_n}{2\mu_0} \sin\left(\frac{n\pi}{L}x_s\right) \frac{\left(\omega_n^2 - \omega^2\right)}{\left(\omega_n^2 - \omega^2\right)^2 + (\omega\gamma)^2} \tag{11.39}$$

Near the resonances, we can apply $\omega_n^2 - \omega^2 \approx 2\omega\left(\omega_n - \omega\right)$.

$$F(\omega) = \sum_{n=1}^{\infty} \frac{I^2 B_n}{\mu_0} \sin\left(\frac{n\pi}{L}x_s\right) \frac{\left(\omega_n - \omega\right)}{4\omega\left(\omega_n - \omega\right)^2 + \omega\gamma^2} \tag{11.40}$$

The value of γ is normally quite small compared to ω_n and therefore, each of the terms in the sum of eq. 11.40 has only a significant value around the resonant frequency. The scanning can then be executed only a few Hz around ω_n to obtain a plot that can be parametrized as,

$$\omega F(\omega) = A_n \frac{\omega_n - \omega}{4\left(\omega_n - \omega\right)^2 + \gamma_n^2} \tag{11.41}$$

In fig, 11.7 the shape of this plot near a resonance is shown for two different damping ratios. Near each resonance, it is possible by fitting to obtain the amplitude A_n, the resonance frequency ω_n and the damping γ_n. Although in the derivation of the wire behavior, we have supposed the damping not to be frequency dependent and to have of viscous origin, in reality it may be non linear and different for each of the resonant frequencies.

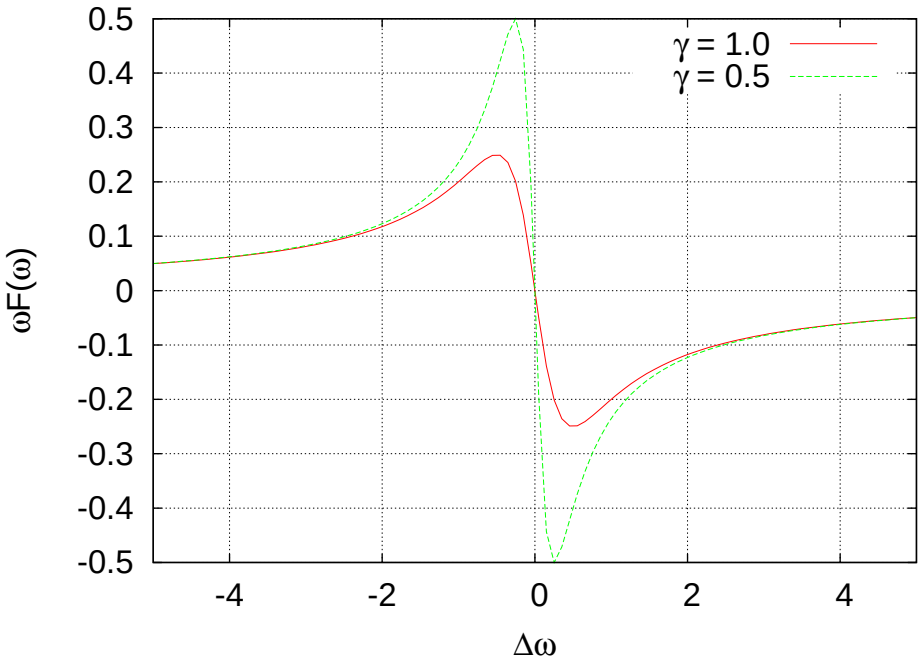

Figure 11.7 – Typical shape of $\omega F(\omega)$ near a resonance. For both curves A_n is unity and only γ is changed. The peak to peak amplitude is $\frac{A_n}{2\gamma}$ and the peak to peak separation is γ

To give a more quantitative approach to the method, we can propose a set of design values. The wave velocity in the vibrating wire will be given by,

$$v = \sqrt{\frac{T}{\mu}} = \sqrt{\frac{\sigma A}{\rho A}} = \sqrt{\frac{\sigma}{\rho}} \tag{11.42}$$

,where σ is the design tensile stress, A the wire section and ρ the material density, The standard material used for this wire is a Beryllium copper alloy (Cu98Be2), because it has a relatively high electrical conductivity and high yield limit to operate safely at high mechanical stress. It has a resistivity as low as 5.4 $\Omega \cdot$ m, a density of 8250 kg/m^3 and a tensile strength of at least 500 MPa. If we operate the wire at 200 MPa, the sound velocity will be 155 m/s. For measuring a short PMQ, the typical length of the wire may be 0.5 m and the first eigenfrequency will be,

$$f_1 = \frac{\omega_1}{2\pi} = \frac{c}{2L} = 155 \text{ Hz} \tag{11.43}$$

11.4 Corrective measurements

After the first assembly and the first measurement of each magnet, it is normally necessary to modify some of the parameters of the magnet to comply with the specifications. This is normally required for integrated gradient, magnetic center and specially for roll adjustment. It has been found that the specification for higher order harmonics is loose enough not to require any feedback from the measurements of the first assembly. This is probably related to the location of the permanent magnets relatively far away from the reference radius, and the effect of the higher order harmonics decaying fast with this distance. In this section, it will be analyzed how the compensation after the out of tolerance measurements is made. The theory of the effect of the individual blocks developed in chapter 7 will be very valuable for this application.

11.4.1 Integrated gradient correction

In order to correct the measured integrated gradient of each quadrupole and approaching it to the target value, the shims of all radial magnets are increased by 0.1 mm when it is desired to decrease the integrated gradient, or the shims of all the tangential magnets are decreased by 0.1 mm when it is desired to increased the integrated gradient. The choice to move the radial magnets in one case and the tangential in the other is required by the need to avoid the radial magnets being in an smaller radial position; as in this case the effect on B_6 of the radial position of the magnets is added to the effect of the larger coercitive field in the tangential magnets, which gives a natural B_6 in the same direction. For a larger variation, all radial and tangential magnets are moved in the same direction. Fig. 11.8 shows the relative effect (in per one) of increasing all 8 shims by 1 mm. The effect of moving 0.1 mm the radial magnets is typically a reduction in the integrated gradient of 0.7%. This variation is fine enough to achieve the required field accuracy of $\pm$ 0.5%.

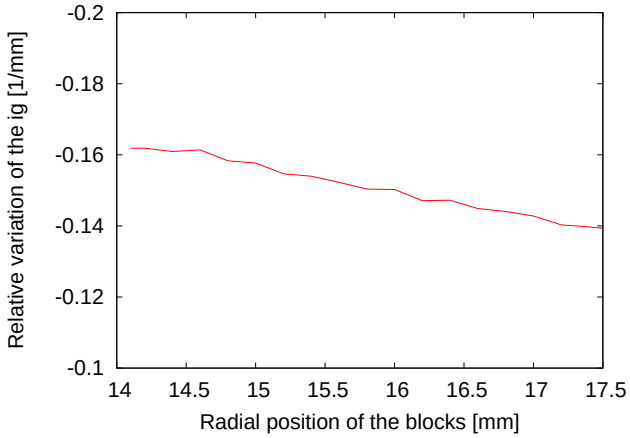

Figure 11.8 – Relative variation of the integrated gradient $dGdL/drGdL^{-1}$ for a variation of the radial position of all 8 shims

11.4.2 Magnetic center correction

For the calculation of the magnetic center, the first harmonic $B_1 + iA_1$ is used. Up to first order, the magnetic field is,

$$B_y + iB_x = B_1 + iA_1 + B_2 \frac{x + iy}{R_{ref}} \tag{11.44}$$

We neglect the higher order harmonics because they are small and as they decrease according to $(r/R_{ref})^{n-1}$ their effect is negligible near the magnetic axis.

The point at which the field will cancel is obtained by equating eq. 11.44 to zero,

$$x_0 = -R_{ref} \frac{B_1}{B_2} = -R_{ref} \frac{b_1}{10^4} \tag{11.45}$$

$$y_0 = -R_{ref} \frac{A_1}{B_2} = -R_{ref} \frac{a_1}{10^4} \tag{11.46}$$

So that correcting the magnetic center is equivalent to canceling the first harmonic. The contributions to the first harmonics may be seen in eq. 7.82, in order to modify, for instance, the real part of C_1, we can shift M_0 and M_4 in opposite directions. In this case, B_2 is not modified, because the effect of both shifts cancels in the second row of 7.82. We can check the effect of a radial displacement ΔR of the first block M_0, by taking the derivative of 7.78,

$$\Delta C_1 = -\frac{\mu_0 M \Delta R}{2\pi} \left(\frac{1}{\xi_1} + \frac{1}{\xi_3} - \frac{1}{\xi_2} - \frac{1}{\xi_4} \right) \tag{11.47}$$

Dividing eq. 11.47 by the value of B_2 as obtained by eq. 7.77 for n equal to 2,

$$\frac{\Delta C_1}{B_2} = -\frac{\Delta R}{8 R_{ref}} \tag{11.48}$$

The fifth block will give the same shift, so that the total displacement of the magnetic center will be,

$$\Delta x_0 = \frac{\Delta R}{4} \tag{11.49}$$

The same analysis may be repeated for the y axis to obtain a similar result involving blocks 3 and 7.

11.4.3 Roll correction

Probably, the roll is the most strict of all the requirements. At the reference radius of 7.5 mm, the arc length of 1 mrad is only 7.5 μm. In order to analyze how to correct the roll error, we have to return to the sensitivity matrix of eq. 7.82. There, we can see that the second harmonic is created by the sum of all the magnetizations, the magnetization in the *nominal* direction creates the desired B_2, while the angle error of the magnetization creates the undesired roll A_2. We can indifferently use the value of roll angle error or a_2, taking into account that 1 mrad is equivalent to 10 units of a_2.

We can conclude that the relative harmonic a_2 is the sum of all the skew magnetizations divided by the sum of all the nominal magnetizations. Because each PMQ is made of blocks of similar magnetization, we can suppose the nominal magnetization to be uniform in all of the blocks, therefore:

$$a_2 = 10^4 \frac{\sum_i M_{s_i}}{\sum_i M_{n_i}} = 10^4 \frac{\sum_i M_{s_i}}{8M_n} = 10^4 \frac{\sum_i \theta_i}{8} \tag{11.50}$$

The roll error is then the average value of the error in the magnetization angle error, θ_i in the blocks used in the PMQ. Typically, the addition of N random errors will be like multiplying the average value by $\sqrt{N}$, and the expected roll error of assembling N magnets will be,

$$a_2 \approx 10^4 \frac{\theta_{block}}{\sqrt{8}} \tag{11.51}$$

Referring to the statistical analysis of section 10.3, the average error in the magnetization angle of the best 560 magnets is 13.3 mrad, we would then expect the average roll error of each PMQ as assembled without any care or correction to be of 4.7 mrad, well above the desired value of 1 mrad.

This problem is solved by two observations. First, the measurement of the blocks, not only provides the absolute sign of the skew magnetization, but also its sign; and second, it is possible to change the sense of the skew magnetization with respect to the PMQ holder by flipping the front and the back of magnet while keeping the nominal magnetization (rotating an angle of π with respect of a radial axis). In such a way, it is possible to cancel the roll error of the PMQ to a value as small of the largest magnetization error angle of the blocks in the PMQ divided by 8.

Unfortunately, during the measurement of the blocks this roll correction method was not yet developed, and the blocks were measured without taking into consideration the flipping of the block in the bench, i.e. where the *east* and *west* of the block were positioned with respect to the measuring bench. Because of that, the roll correction was an iterative process, in which some of the blocks were rotated until the desired PMQ roll was obtained. Typically, 3 iterations were required per magnet in order to obtain the desired roll.

11.5 Summary of the magnet manufacturing

After some 400 individual assemblies, measurements and corrections, all magnets were put in tolerance and send to CERN. The measurements at CERN confirmed that basically ours and the magnets could be integrated in linac4.

The experience was extremely positive for the company, as it allowed to develop the technology required to design and manufacture similar projects for other linacs, at BARC and ESS.

CHAPTER 12

Conclusions

This work has presented several contributions that I would like to remark in the conclusion, making emphasis in the results that I consider to be a novelty. Directly, or not, they are related to several aspects of the science of guiding charged particles through the use of electromagnetic fields.

It has proven the feasibility of using the very high sensitivity of high-Q cavities to the change of their external boundary to create a range of displacement sensors that thanks to their inherent bandwidth, noise immunity and easy interfacing to the measurement electronics may be applied to a large series of applications. The measurements on the prototype has confirmed the calculations and sensitivities in the range of nm could be achieved, combined with bandwidths that cannot be reached with any other sensor of the same range, like capacitive ones. This new sensor has been the object of a patent.

A significant contribution has been made to the complex theory of the linear dynamics by generalizing some results that were known since the 50s on the possibility of combining the beam envelope parameters on a single complex number. The general equation of the envelope has been found and solved. It has been shown that the formalism is equivalent to the Twiss parameters, but by recognizing that the evolution along any beam line is a Moebius transform, it has been possible to apply a large corpus of already developed theory, like circle invariance, to obtain results that can be only extracted with extreme difficulty from the algebra of the Twiss parameters transform. These results, have a beautiful geometrical interpretation on the complex plane which is hidden in the classical formalism.

Another contribution has been made on the development of a large aperture spectrograph using direct ray tracing from a Finite Element Method program to a custom made, high efficient, program. This approach has allowed to design and build an analyzing magnet of the highest acceptance.

The complex theory of magnetic fields has been developed and used to design the linac4 permanent magnet quadrupoles for CERN. It has been proven that an 8 block design in spite of its apparently excessive simplicity is the best solution for this application, in which a modest gradient is required. It has been shown how to characterize and sort the permanent magnet blocks to provide high quality quadrupoles from lower quality blocks and how to measure the magnets in order to validate its design and construction.

The developments produced during the present work, apart from its purely technical interest, has significantly enhanced the positioning of my Company in the fields covered by it. I would like to emphasize that, for instance, the developments we did in Permanent Magnet Quadrupoles has open us the field to supply this components to 2 new customers in India and

Italy. Actually, linking the scientific and industrial sides of the projects has been the major pleasure in the present work.

Bibliography

[1] E Abad, I Arredondo, I Badillo, D Belver, F J Bermejo, I Bustinduy, D Cano, D Cortazar, D de Cos, S Djekic, S Domingo, P Echevarria, M Eguiraun, V Etxebarria, D Fernandez, F J Fernandez, J Feuchtwanger, N Garmendia, G Harper, H Hassanzadegan, J Jugo, F Legarda, M Magan, R Martinez, A Megia, L Muguira, G Mujika, J L Munoz, A Ortega, J Ortega, M Perlado, J Portilla, I Rueda, F Sordo, V Toyos, and A Vizcaino. Ess-bilbao light-ion linear accelerator and neutron source: design and applications. *Journal of Physics: Conference Series*, 325(1):012003, 2011.

[2] A.J.Lichtenberg. *Phase-Space dynamics of Particles*. John Wiley & Sons, 1969.

[3] M. Aleksa, J. Lucas, and S. Russenschuck. Optimisation of a periodic solenoidal focusing system. *Electrical Engineering*, 87(5):231–236, 2005.

[4] Roch Andrzejewski. *New methods for high-resolution ion beam analysis*. PhD thesis, Universidad Autónoma de Madrid, June 2008.

[5] L Arnaudon, P Baudrenghien, M Baylac, G Bellodi, Y Body, J Borburgh, P Bourquin, J Broere, O Brunner, L Bruno, C Carli, Friedhelm Caspers, S M Cousineau, Y Cuvet, C De Almeida Martins, T Dobers, T Fowler, R Garoby, F Gerigk, B Goddard, K Hanke, M Hori, M Jones, K Kahle, Willi Kalbreier, T Kroyer, D Küchler, A M Lombardi, L A López-Hernandez, M Magistris, M Martini, S Maury, E Page, M Paoluzzi, M Pasini, U Raich, C Rossi, J P Royer, E Sargsyan, J Serrano, R Scrivens, M Silari, M Timmins, W Venturini-Delsolaro, M Vretenar, R Wegner, W Weterings, and T Zickler. Linac4 Technical Design Report. Technical Report CERN-AB-2006-084. CARE-Note-2006-022-HIPPI, CERN, Geneva, Dec 2006. revised version submitted on 2006-12-14 09:00:40.

[6] E. Asua, V. Etxebarria, A. García-Arribas, J. Feutchwanger, J. Portilla, and J. Lucas. Electronic interface for position sensing using resonant cavities. In *5th IEEE International Workshop on Advances in Sensors and Interfaces IWASI*, pages 142–147, June 2013.

[7] E. Asua, V. Etxebarria, A García-Arribas, J Feutchwanger, J Portilla, and J Lucas. Interface electronics for an rf resonance-based displacement sensor. *Journal of Physics: Conference Series*, 450(1):012017, 2013.

[8] Estibaliz Asua, Victor Etxebarria, Alfredo García-Arribas, Jorge Feutchwanger, Joaquín Portilla, and Julio Lucas. A novel micro- and nano-scale positioning sensor based on radio frequency resonant cavities. *Sensors*, 14(6):9615–9627, 2014.

[9] R.A. Beth. Complex representation and computation of two-dimensional magnetic fields. *Journal of Applied Physics*, 37(7):2568, 1966.

[10] R.A. Beth. An integral formula for two-dimensional fields. *Journal of Applied Physics*, 38(12):4689, 1967.

[11] R.A. Beth. Currents and coil forces as contour integrals in two-dimensional magnetic fields. *Journal of Applied Physics*, 40(6):2445, 1969.

[12] R.A. Beth. Complex methods for three-dimensional magnetic fields. *IEEE Trans.Nucl.Sci.*, 18:901–903, 1971.

[13] E. W. Blackmore. Radiation effects of protons on samarium cobalt permanent magnets. *IEEE Transactions on Nuclear Science*, NS-32, No. 5:3669–3671, 1985.

[14] Amos Breskin and Rüdiger Voss. *The CERN Large Hadron Collider: Accelerator and Experiments*. CERN, Geneva, 2009.

[15] J.C. Browne, J.L. Anderson, and M.W. Cappiello. *Status of the Accelerator Production of Tritium (APT) project*. Jul 1996.

[16] Didier De Bruyn, Hamid Aït Abderrahim, Peter Baeten, and Paul Leysen. The {MYRRHA} {ADS} project in belgium enters the front end engineering phase. *Physics Procedia*, 66:75 – 84, 2015. The 23rd International Conference on the Application of Accelerators in Research and Industry - {CAARI} 2014.

[17] M. Buzio, G. Golluccio, A. Lombardi, and F. Mateo. Magnetic qualification of permanent magnet quadrupoles for cern's linac4. *IEEE Transactions on Applied Superconductivity*, 22(3):4004304–4004304, June 2012.

[18] M. G. Calkin. *Lagrangian and hamiltonian mechanics*. World Scientific, 1998.

[19] C.H. et al. Chen. The effect of neutron irradiation on nd-fe-b and sm2co17-based high-temperature magnets. *IEEE Transactions on Magnetics*, 41(10):3832–3834, 2005.

[20] V. Dubrovski, Ya. Smorodinski, and E. Surkov. *El Mundo Relativista*. Ed. Mir, 1987.

[21] Romuald Duperrier, Nicolas Pichoff, and Didier Uriot. *CEA Saclay Codes Review for High Intensities Linacs Computations*, pages 411–418. Springer Berlin Heidelberg, Berlin, Heidelberg, 2002.

[22] S. Peggs (Ed.). *ESS Technical design report*. 2013.

[23] J.Knaster et al. IFMIF, the European Japanese efforts under the Broader Approach agreement towards a Li(d,xn) neutron source: Current status and future options. *Nuclear Materials and Energy*, 9:46–54, 2016.

[24] Jose V. Mathew et al. An improved permanent magnet quadrupole design with larger good field region for high intensity proton linacs. *Nuclear Instrument and Methods in Physics Research A 727*, pages 12–20, 2013.

[25] R. Andrzejewski et al. A wide angle spectrograph of a novel design. *Nuclear Instruments and Methods in Physics Research B*, 249:939–942, 2006.

[26] V. Etxeberria et al. Very high sensitivity displacement sensor based on resonant cavities. *IEEE Sensors Journal*, 10(8):1335–1336, August 2010.

[27] William H. Press et al. *Numerical Recipes in C*. Cambridge University Press, 1988.

[28] Lyndon Evans and Philip Bryant. LHC Machine. *Journal of Instrumentation*, 3(08):S08001, 2008.

[29] Robert B. Leighton Feynman Richard P. and Matthew L. Sands. *The Feynman Lectures on Physics*. Addison-Wesley Pub., Reading, Mass., 1963.

[30] D. Lens H. Klingbeil, U. Laier. *Theoretical Foundations of Synchrotron and Storage Ring RF Systems*. Springer, 2015.

[31] K. Halbach. Design of permanent multipole magnets with oriented rare earth cobalt material. *Nuclear Instruments and Methods*, 169(1):1 – 10, 1980.

[32] H.G. Hereward. THE PROPERTIES OF PARTICLE BEAMS IN OPTICAL MATCHING SYSTEMS, IN TERMS OF PHASE - PLANE ELLIPSE SHAPES. Technical Report CERN-PS-TH-59-5, CERN, 1959.

[33] The IFMIF international collaboration. *IFMIF Comprehensive Design Report*. 2004.

[34] T.W. Elgar J. W. Elmer. Measuring the residual ferrite content of rapidly solidified stainless steel alloys. *69th Annual AWS Meeting*, pages 141–150, 1988.

[35] W. Joho. Representation of beam ellipses for transport calculation. Technical Report SIN-REPORT TM-11-14, Paul Scherrer Institute, 1980.

[36] S. Wolff K. H. Mess, P. Schmueser. *Superconducting accelerator magnets*. World Scientific, 1996.

[37] Vinit Kumar. Understanding the focusing of charged particle beams in a solenoid magnetic field. *Am. J. Phys.*, 77:737–741, 2009.

[38] Julio Lucas Torralba and Victor Etxebarria Ecenarro. Sensor de desplazamiento basado en cavidades de radiofrecuencia resonantes, March 2012. ES 2377405 B1.

[39] Steven M. Lund and Klaus Halbach. Iron-free permanent magnet systems for charged particle beam optics. *Fusion Engineering and Design*, 32Ű33(0):401 – 415, 1996. Proceedings of the Seventh International Symposium on Heavy Ion Inertial Fusion.

[40] T. Mason. The Spallation Neutron Source: A Powerful Tool for Materials Research. In A. W. Chao, editor, *Linac 2000*, page 1043, 2000.

[41] J L Munoz, N Garmendia, J Feuchtwanger, I Bustinduy, V Toyos, J Portilla, V Etxebarria, F J Bermejo, E Asua, and J Lucas. Rf measurements and numerical simulations for the model of the bilbao linac double spoke cavity. *Proceedings of 2011 Particle Accelerator Conference*, 2011.

[42] T. Needham. *Visual Complex Analysis*. Oxford University Press, 1997.

[43] Hasan Padamsee, Tom Hays, and Jens Knobloch. *RF superconductivity for accelerators*. Wiley series in beam physics and accelerator technology. Wiley, New York, NY, 1998.

[44] Suitbert Ramberger et al. Drift Tube Linac Design and Prototyping for the CERN Linac4. In *Proceedings, 24th International Linear Accelerator Conference, LINAC2008*, page MOP049, 2008.

[45] Suitbert Ramberger et al. Production Design of the Drift Tube Linac for the CERN Linac4. In *Proceedings, 25th International Linear Accelerator Conference, LINAC2010: Tsukuba, Japan, September 12-17, 2010*, page TUP066, 2011.

[46] E. Regenstreif. *Focusing with quadrupoles, Doublets and Triplets*. Academic Press, New York and London, 1967.

[47] H. Schwerdtfeger. *Geometry of Complex Numbers*. Dover Publications, 1979.

[48] V.S Skachkov. Quasi-sheet multipole permanent magnets. *Nuclear Instruments and Methods in Physics Research Section A: Accelerators, Spectrometers, Detectors and Associated Equipment*, 500(1Ű3):43 – 54, 2003. NIMA Vol 500.

[49] J. Spencer and J. Volk. Permanent magnets for radiation damage studies. *Proceedings of the 2003 Particle Accelerator Conference*, pages 2180–2182, 2003.

[50] Alexander Temnykh. Vibrating wire field-measuring technique. *Nuclear Instruments and Methods in Physics Research A*, 399:185–194, 1997.

[51] Y. M. Tsipenyuk. *The microtron, development and applications*. Taylor and Francis, 2002.

[52] J. T. Volk. *Summary of radiation damage studies on rare earth permanent magnets*. Nov 2002.

[53] V.V.Nikolski. *Electrodinámica y propagación de ondas de radio*. YPCC, 1973.

[54] J.L. Warren and Los Alamos National Laboratory. Accelerator Code Group. *Poisson/-superfish Reference Manual*. Los Alamos National Laboratory, 1987.

[55] H. Wiedeman. *Particle Accelerator Physics*. Springer-Verlag, 1993.